

SANDIA REPORT

SAND2014-0681

Unlimited Release

Printed January 2014

SMART Wind Turbine Rotor: Design and Field Test

Jonathan C. Berg, Brian R. Resor, Joshua A. Paquette, and Jonathan R. White

Prepared by
Sandia National Laboratories
Albuquerque, New Mexico 87185 and Livermore, California 94550

Sandia National Laboratories is a multi-program laboratory managed and operated by Sandia Corporation, a wholly owned subsidiary of Lockheed Martin Corporation, for the U.S. Department of Energy's National Nuclear Security Administration under contract DE-AC04-94AL85000.

Approved for public release; further dissemination unlimited.



Sandia National Laboratories

Issued by Sandia National Laboratories, operated for the United States Department of Energy by Sandia Corporation.

NOTICE: This report was prepared as an account of work sponsored by an agency of the United States Government. Neither the United States Government, nor any agency thereof, nor any of their employees, nor any of their contractors, subcontractors, or their employees, make any warranty, express or implied, or assume any legal liability or responsibility for the accuracy, completeness, or usefulness of any information, apparatus, product, or process disclosed, or represent that its use would not infringe privately owned rights. Reference herein to any specific commercial product, process, or service by trade name, trademark, manufacturer, or otherwise, does not necessarily constitute or imply its endorsement, recommendation, or favoring by the United States Government, any agency thereof, or any of their contractors or subcontractors. The views and opinions expressed herein do not necessarily state or reflect those of the United States Government, any agency thereof, or any of their contractors.

Printed in the United States of America. This report has been reproduced directly from the best available copy.

Available to DOE and DOE contractors from

U.S. Department of Energy
Office of Scientific and Technical Information
P.O. Box 62
Oak Ridge, TN 37831

Telephone: (865) 576-8401
Facsimile: (865) 576-5728
E-Mail: reports@adonis.osti.gov
Online ordering: <http://www.osti.gov/bridge>

Available to the public from

U.S. Department of Commerce
National Technical Information Service
5285 Port Royal Rd.
Springfield, VA 22161

Telephone: (800) 553-6847
Facsimile: (703) 605-6900
E-Mail: orders@ntis.fedworld.gov
Online order: <http://www.ntis.gov/help/ordermethods.asp?loc=7-4-0#online>



SAND2014-0681
Unlimited Release
Printed January 2014

SMART Wind Turbine Rotor: Design and Field Test

Jonathan C. Berg, Brian R. Resor, Joshua A. Paquette, and Jonathan R. White
Wind Energy Technologies Department
Sandia National Laboratories
P.O. Box 5800
Albuquerque, New Mexico 87185-MS1124

Abstract

The Wind Energy Technologies department at Sandia National Laboratories has developed and field tested a wind turbine rotor with integrated trailing-edge flaps designed for active control of rotor aerodynamics. The SMART Rotor project was funded by the Wind and Water Power Technologies Office of the U.S. Department of Energy (DOE) and was conducted to demonstrate active rotor control and evaluate simulation tools available for active control research. This report documents the design, fabrication, and testing of the SMART Rotor.

This report begins with an overview of active control research at Sandia and the objectives of this project. The SMART blade, based on the DOE / SNL 9-meter CX-100 blade design, is then documented including all modifications necessary to integrate the trailing edge flaps, sensors incorporated into the system, and the fabrication processes that were utilized. Finally the test site and test campaign are described.

ACKNOWLEDGMENTS

The SMART rotor project was funded by the U.S. Department of Energy (DOE) Wind and Water Power Technologies Office (director Jose Zayas) under the office of Energy Efficiency and Renewable Energy (EERE, assistant secretary David Danielson).

The authors gratefully acknowledge all those who contributed to this project, including the following:

USDA-ARS staff at Bushland Test Site

- Adam Holman
- Byron Neal

Testing

- Wesley Johnson
- Bruce LeBlanc
- Nate Yoder (ATA Engineering)

Data Acquisition System programming

- Juan Ortiz-Moyet (Prime Core)

Blade Modification

- David Calkins
- Mike Kelly
- Bill Miller

Blade Manufacture by TPI Composites

SMART blade design

- Matt Barone
- Dale Berg
- Jonathan Berg
- Gary Fischer
- Josh Paquette
- Brian Resor
- Mark Rumsey
- Jon White

Consultation

- Derek Berry (TPI Composites)
- Mike Zuteck (MDZ Consulting)

CONTENTS

1. Introduction.....	11
1.1. Background of SMART Rotor Research at Sandia	12
1.2. Project Objectives	12
2. Blade Design.....	13
2.1. Options Considered.....	13
2.2. Conceptual Design.....	14
2.3. Structural Design	15
2.3.1. Initial Detailed Design of Structural Changes.....	15
2.3.2. Sectional Analysis of Initial Design with PreComp.....	17
2.3.3. Final Structural Design.....	19
2.3.4. Finite Element Analysis (FEA) of Final Design	20
2.4. Maximum Aerodynamic Forces and Moments.....	28
2.5. Hinged Flap Module Design	30
2.5.1. Module Components	30
2.5.2. Required Actuator Torque.....	33
2.5.3. Actuator Selection	35
2.5.4. Module Stress Analysis	37
3. Blade Construction and Device Integration	39
3.1. Instrumentation Plan	39
3.2. Mitigation of Electrostatic Discharge	39
3.3. Blade Construction.....	40
3.4. Post-build Blade Modification.....	41
3.5. Flap Module Construction and Integration	43
4. Control Hardware.....	45
5. Field Test	47
5.1. Layout of the Test Site.....	47
5.2. Test Turbine	48
5.3. Instrumentation	49
5.4. Test Cases	49
6. Conclusion	53
7. References.....	55
Appendix A: Original CX Layup.....	59
Low Pressure Skin	59
High Pressure Skin.....	62
Appendix B: Changes to PreComp v1.00.02	64
Appendix C: VectorPly Data Sheet	65
Appendix D: PreComp Section Analysis Inputs.....	67
Material Properties.....	67
Input file	67
Webs:	67

Main shear web	67
Aft flange.....	67
Station 5	68
Overall 68	
Layup (webs present but not shown here).....	68
Station 5.1 (cutout).....	69
Overall 69	
Layup (webs present but not shown here).....	69
Station 6.1 (cutout).....	72
Overall 72	
Layup (webs present but not shown here).....	72
Station 7.1 (cutout).....	75
Overall 75	
Layup (web present but not shown here)	75
Station 8.1	78
Overall 78	
Layup (web present but not shown here)	78
Appendix E: SMART Blade Layup.....	79
Low Pressure.....	79
High pressure	80
Appendix F: Inflow and Turbine Instrumentation	82
Appendix G: Data File Summaries	84
Distribution	92

FIGURES

Figure 2.1	Interchangeable tip of a DG800 Sailplane.	14
Figure 2.2	Blade retrofit concept.	15
Figure 2.3	Flap module AAD concept.	15
Figure 2.4	CX-100 layup and SMART blade alterations.	16
Figure 2.5	Outboard blade planform.	17
Figure 2.6	Sectional analysis results of original CX-100 and SMART blade.	19
Figure 2.7	SMART Blade FEA Model.	20
Figure 2.8	Trailing edge cutout modification to model.	21
Figure 2.9	Outboard section of model.	21
Figure 2.10	Outboard webs and rib.	21
Figure 2.11	Model with loads applied.	22
Figure 2.12	Loading applied at outboard section.	22
Figure 2.13	HP spanwise strains.	23
Figure 2.14	LP spanwise strains.	24
Figure 2.15	Main web shear strains.	25
Figure 2.16	Aft web shear strains.	26
Figure 2.17	Rib shear strains.	27
Figure 2.18	Flap AAD module design overview.	30
Figure 2.19	Module base design.	31
Figure 2.20	Additional features in second module.	32
Figure 2.21	Module flap design.	32
Figure 2.22	Final flap module design.	33
Figure 2.23	Simulated angle-of-attack along blade span.	34
Figure 2.24	Motor torque-speed curves.	36
Figure 3.1	Schematic of internal sensor locations.	40
Figure 3.2	Blade set after removal of trailing edge.	41
Figure 3.3	Aft spar bonded into place.	42
Figure 3.4	Fully assembled SMART blade set.	43
Figure 4.1	AAD control box.	46
Figure 5.1	Schematic overview of the test site.	47
Figure 5.2	Site plan with detailed dimensions.	48
Figure 5.3	Strain response to flap step sequence.	50
Figure 5.4	Sequence of video frames during turbine operation.	51

TABLES

Table 2.1	Table of trailing edge changes in PreComp analysis.	18
Table 2.2	Layer thickness for laminate materials.	19
Table 2.3	Force and moment coefficients at flap hinge line.	29
Table 2.4	Force and moment coefficients at module-to-blade interface.	29
Table 2.5	Calculated forces and moments on each module.	29
Table 2.6	Mass properties of the flaps.	33
Table 2.7	Flap inertial loading due to blade flapwise motion.	35
Table F.1	Inflow Instrumentation.	82
Table F.2	Turbine Instrumentation.	82
Table F.3	Rotor Instrumentation.	83
Table G.1	Initial shakedown.	84
Table G.2	First operation during power production.	85
Table G.3	Static flap settings with 10-minute data files.	86
Table G.4	Sine sweeps during power production.	87
Table G.5	Power production at prevailing wind direction with flap step series.	88
Table G.6	Power production with flap step series.	89
Table G.7	Data files during video of flaps in operation.	90
Table G.8	Power production with tape sealing possible air gaps in flap modules.	90

NOMENCLATURE

AAD	active aerodynamic device
AALC	active aerodynamic load control
aft	toward the trailing edge of a wind turbine blade
chordwise	in the direction of airfoil chord and perpendicular to blade span
DOE	Department of Energy (U.S.)
edgewise	similar to chordwise but used to describe blade loads and deflections
ESD	electrostatic discharge
flapwise	perpendicular to edgewise and in the direction of blade “flapping” motion
HAWT	horizontal axis wind turbine
HP	high-pressure (the nominally upwind surface of a HAWT blade)
inboard	toward the root end of a wind turbine blade
layup	the stack of layers which constitute a composite blade structure
LP	low-pressure (the nominally downwind surface of a HAWT blade)
outboard	toward the tip of a wind turbine blade
PID	proportional-integral-derivative
planform	shape of a blade as viewed from the HP or LP side
R&D	research and development
SMART	Structural and Mechanical Adaptive Rotor Technology
SNL	Sandia National Laboratories
spanwise	in the direction of the blade length
UV	ultra-violet light

1. INTRODUCTION

As the United States seeks to establish a diverse portfolio of clean and renewable energy systems, continued development of wind energy technology is essential to reaching renewable energy deployment goals. The Report on the First Quadrennial Technology Review (QTR), published by the U.S. Department of Energy in September 2011, was written to “establish a framework for thinking clearly about a necessary transformation of the Nation’s energy system” [1]. The QTR was a first step in developing guiding principles for DOE to prioritize investment of R&D funds. Within the “Clean Electricity Generation” strategy outlined in the report, wind energy is described as a fairly mature technology which is cost competitive at good wind sites and continues to expand market deployment. At a high-level assessment, the report states the technical headroom for additional research and development exists mainly in grid integration and subsystem reliability as well as tapping into the offshore wind resource.

The 20% Wind Energy by 2030 report [2], published in July 2008, provides a more detailed assessment of the technical headroom for additional R&D. The core opportunities it identifies include reducing capital costs, increasing capacity factors, and mitigating risk through enhanced system reliability. The rotor itself is highlighted as a key target for technology improvement because it is the source of all energy captured and of most of the structural loads entering the system. Increasing rotor size while controlling rotor loads will directly impact the capacity factor and the life of components within the main load path. The report mentions both passive load control in which the structural and material properties of the blades are tailored to passively mitigate loads and active load control in which a control system senses rotor loads and actively responds by driving aerodynamic actuators.

Reducing ultimate and oscillating (or fatigue) loads on the wind turbine rotor can lead to reductions in loads on other turbine components such as the main bearings, gearbox, and generator. This, in turn, is expected to reduce maintenance costs and may also allow a given turbine to use longer blades to capture more energy. In both cases, the ultimate impact is reduced cost of wind energy. With the ever increasing size of wind turbine blades and the corresponding increase in non-uniform loads along the span of those blades, the need for more sophisticated load control techniques has produced great interest in the use of aerodynamic control devices (with associated sensors and control systems) distributed along each blade to provide feedback load control (often referred to in popular terms as ‘smart structures’ or ‘smart rotor control’). A review of concepts and inventory of design options for such systems have been performed by Barlas and van Kuik at Delft University of Technology (TU Delft) [3]. Active load control utilizing trailing edge flaps or deformable trailing edge geometries is receiving significant attention because of the direct lift control capability of such devices. Researchers at TU Delft [4-5], Risø/Danish Technical University Laboratory for Sustainable Energy (Risø/DTU) [6-12] and Sandia National Laboratories (SNL) [13-19] have been active in this area over the past decade.

1.1. Background of SMART Rotor Research at Sandia

Sandia's involvement with active aerodynamic load control (AALC) can be traced back to collaborations with C.P. van Dam and R. Chow on the microtab device concept [20] and also to internal efforts of D. Berg, J. Zayas, and D. Lobitz to identify the controls, sensors, and actuators needed to implement these or similar devices [21]. Since that time, work has steadily progressed to improve simulation capabilities and evaluate the potential benefits of AALC on wind turbine performance. This work established hypothetical approaches for integrating active aerodynamic devices (AADs) into the wind turbine structure and controllers, but it has needed the validation and additional insight that a field test would provide. In 2010, Sandia began a three-year project to design, build, and test a rotor with integrated sensors and active aerodynamic load control devices.

1.2. Project Objectives

While there were many questions associated with the use of active aerodynamic devices that must be answered with field testing experience and experimental data, the general goals were restricted to the following:

- Test the control authority of one particular type of AAD.
- Acquire experimental data required to evaluate AALC simulation tools.
- Evaluate/demonstrate numerous aerodynamic and structural sensor systems to determine those that offer the most benefit as signal inputs for the AALC controllers.
- Develop procedures for characterizing an operating wind turbine system which incorporates AALC.
- Identify structural design changes required within a rotor blade to accept the AAD.
- Identify requirements and challenges producing an integrated AALC rotor blade.

2. BLADE DESIGN

2.1. Options Considered

Initial project planning focused mainly on adapting the DOE/SNL CX-100 research blade as the starting point for the SMART blade design. Choosing to retrofit the existing CX-100 blade design would allow the design team to focus on the AAD implementation and blade integration and to build upon previous design work thereby minimizing the amount of analysis required to ensure the new design could withstand operating loads. Much experience and knowledge had been gained through testing of the CX-100 [22-24], TX-100 [22-24], and Sensor Blade [25-26]. The structural properties and aerodynamic performance of the baseline CX-100 blade design had been well characterized through field and lab testing. Sensor integration techniques had been developed and proven with the Sensor Blade / Rotor projects. The TX-100 was not used for this project because the combination of passive and active load control, although promising for future projects, was considered unnecessarily complicating for the objectives of this project.

A significant challenge of the SMART blade design was the limited space available in the outboard portion of this 9-meter blade within which to fit AAD mechanisms. Although using a slightly larger scale blade and turbine was attractive, the benefits of having a well characterized baseline for comparison and not needing to duplicate previous design efforts were two factors which pointed strongly toward choosing the CX-100 design.

With regard to the AAD technology itself, the design team considered microtabs and two types of trailing edge flaps: conventional rigid hinged and flexible with continuous deformation.

Researchers at the University of California, Davis (UC Davis) had been investigating microtabs for a number of years using both high fidelity simulation and wind tunnel testing. They conducted their work both independently and under contract with Sandia. Within the last few years leading up to this report they tested a microtab design with actively deployable tabs in a wind tunnel. At Sandia, another mechanism for deployable microtabs was prototyped. However, at the beginning of the SMART rotor project, there was much uncertainty regarding the amount of effort required to scale down these prototypes to the size required to fit within the available space.

In previous work with FlexSys Inc., Sandia investigated deformable trailing edge technology and sketched out a plan for integration into a wind turbine blade. However, once again there was much uncertainty about scaling down the technology for the SMART rotor.

Thus, to minimize uncertainty and risk in the project, the design team decided to use a conventional rigid flap design which would be actuated much like a scale-model airplane's control surfaces. Although a rigid flap was not as aerodynamically efficient as a deformable trailing edge design, it satisfied the objectives of demonstrating the control authority of an active aerodynamic device and testing the capabilities of AALC simulation tools.

2.2. Conceptual Design

Initial thoughts on AAD integration moved toward a modular concept in which the whole blade tip would be interchangeable. Figure 2.1 shows an example of an interchangeable tip for the glass composite wing structure of a sailplane. Although this idea was attractive for the flexibility of trying multiple active aerodynamic device technologies, the amount of design work needed to implement the idea would have detracted from the main project goals and increased project risk. Additionally, the potential discontinuities in the structural dynamics across the joint may have created unnecessary complexity and substantial differences compared to the baseline CX-100 structural dynamics.



Figure 2.1 Interchangeable tip of a DG800 Sailplane. Photos by Brian Resor.

The concept for AAD integration converged on modification to the outboard trailing edge section while leaving the original main blade structure intact. The overall concept is portrayed in Figure 2.2 in which the original shear web (teal) is visible and the two new structural components, the aft spar (magenta) and inboard rib (orange), have been added where the trailing edge section was removed. The aft spar rejoined the upper and lower skins, thereby completing the “torque tube” to provide a path for loads, and it also provided a mounting location for the AAD hardware. The rib was added to provide a load path between the main shear web and the aft spar.

The concept also maintained a somewhat modular aspect because different AAD hardware packages could theoretically be designed to fit the available space. However, the feasibility of making new modules would depend on compatibility of the new hardware with the placement of mounting features and control cabling.

The initial concept for the hinged flap AAD is shown in Figure 2.3. The base piece (blue trapezoidal piece) housed the motor actuator and mounted to the aft spar. A timing belt transmitted the motor shaft motion to the flap (red triangular piece).

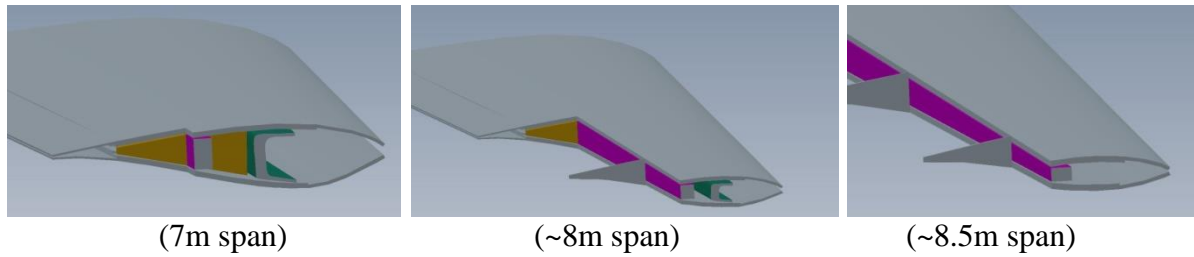


Figure 2.2 Blade retrofit concept with representative blade cross sections at 7m, 8m, and 8.5m showing the shear web (teal C-channel), rib (orange triangle), and aft spar (magenta).

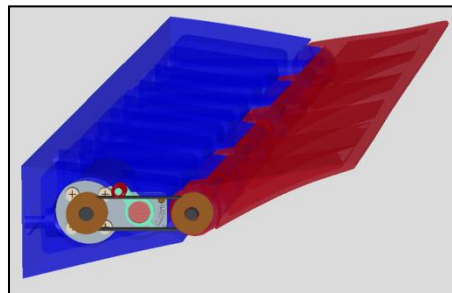


Figure 2.3 Flap module AAD concept.

2.3. Structural Design

An overview schematic of the baseline CX-100 layup is shown in Figure 2.4 and detailed drawings are contained in Appendix A. This design incorporated carbon fiber spar caps which ran nearly the entire length of the blade, providing increased stiffness. A single shear web, constructed of fiber glass and balsa, bridged between the two blade skins at the spar cap location. In the outboard trailing-edge panels aft of the spar caps, the blade skin laminate stack consisted of the following layers:

- gel coat at the outer surface
- fiber-glass mat, 3/4 oz.
- double-bias fiber glass, DBM-1708, oriented at $\pm 45^\circ$ to blade centerline
- balsa core, 1/4 inch thick (from root to 8.5m span)
- double-bias fiber glass, DBM-1708, oriented at $\pm 45^\circ$ to blade centerline

2.3.1. Initial Detailed Design of Structural Changes

The approach for designing the SMART blades was to start with the CX-100 design [27] and then introduce modifications for integrating the AAD hardware. The main design change was the blade cutout which accepted the AAD hardware as illustrated in Figure 2.4. The cutout extended forward of the trailing edge by 40% of chord at span 7.029 m (the inboard end) and linearly expanded to 50% of chord at 8.857 m (the outboard end). This cutout did not extend to the tip of

the blade; rather, the outer 14.3 cm (one tip chord length) of the trailing edge was left intact to minimize the impact of the blade tip vortex on the performance of the AAD. The shear web remained the same as the original.

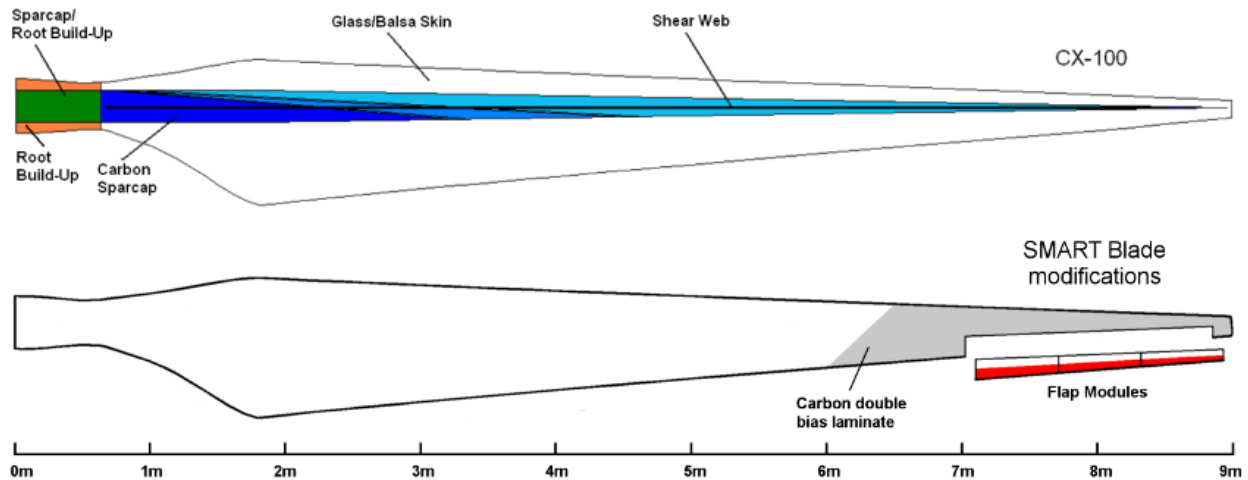


Figure 2.4 The SMART blade design incorporates all of the CX-100 features plus modifications for integrating the AAD hardware.

Removing this amount of material from the original CX-100 blade would have had very large impacts on the structural properties of the blade in the outboard region – the edgewise, flapwise, and torsional stiffness properties would all have been reduced significantly. The strategy which guided the design modifications was to regain the original stiffness properties and thereby avoid repeating all of the blade certification calculations. (This approach assumed the active aerodynamic devices would be controlled in a way which did not exceed the original design loads.)

In order to minimize or eliminate stiffness reductions, the SMART blade design replaced the outer layer of glass double-bias laminate in both the high pressure and low pressure skins with two layers of carbon fiber double-bias laminate. As shown in Figure 2.4, the carbon material was introduced along a diagonal, starting at 6 m on the trailing edge and reaching the leading edge at about 6.5 m, with the transition line between glass and carbon following the carbon fiber direction of 45°. In the transition region from glass fiber to carbon fiber, the inboard edges of the two carbon layers overlapped the outboard edge of the glass layer by 4 inches so that a load path would exist between the two skin materials.

The CX-100 shear web ended at approximately 8 m. The SMART design added a spar between 7.0 m and 8.8 m, positioned somewhat aft of the original shear web. This aft spar provided a mounting point for the active aero modules, facilitated the transfer of the associated loads down from the blade tip into the main blade structure, and helped to maintain torsional stiffness. The balsa core in the aft panels outboard of 7.0 m was removed because the aft spar and cutout reduced the aft panel size which eliminated any concerns of panel buckling.

The initial design of the new aft spar consisted of outside layers of double-bias carbon fiber (DB-carbon) with an inner core of birch plywood. Fiber direction was oriented $\pm 45^\circ$ relative to the span-wise axis so that torsional blade forces would be carried efficiently. No uni-directional carbon was included because additional bending stiffness in the spar was deemed unnecessary and undesirable. The shape of the spar was a straight web without any flanges.

The initial design also included a single rib at the inboard end of the cutout region to help transfer the loads from the aft spar to the main shear web. The rib would utilize the same layup as the spar.

2.3.2. Sectional Analysis of Initial Design with PreComp

If original stiffness properties were captured, then the new blade design would be deemed adequate for expected loads. Therefore, the goal of the sectional analysis was to produce a design with cut-out trailing edge and aft spar that possessed all the stiffness properties of the original CX-100 design. This work focused on assessing SMART Blade stiffness properties relative to the original CX-100 blade.

Analysis was performed with a version of PreComp [28] based on version 1.00.02 which includes changes outlined in Appendix B.

Station locations in this PreComp analysis corresponded with station locations of the CX-100 NuMAD [29] model. They were not adjusted to correspond exactly with span dimensions of the trailing edge cutout (e.g. inboard cut at 7.2 m in NuMAD versus actual 7.0 m intended for SMART blade) because the stiffness properties would be extrapolated and interpolated at locations between the analyzed stations.

The following configuration, visualized in Figure 2.5, was analyzed:

- At 7.2m span: Cut off T.E. at 60% from leading edge
- At 9m span: Cut off T.E. at 50% from leading edge
- No balsa core in panels starting at 7.2 m span
- Each layer of DB-glass in skin replaced with two layers of DB-carbon starting at about 6.5 m span
- Aft spar constructed with combination of balsa (or birch) and DB-carbon
- No modifications to the main shear web (i.e. glass and balsa, leave as is)

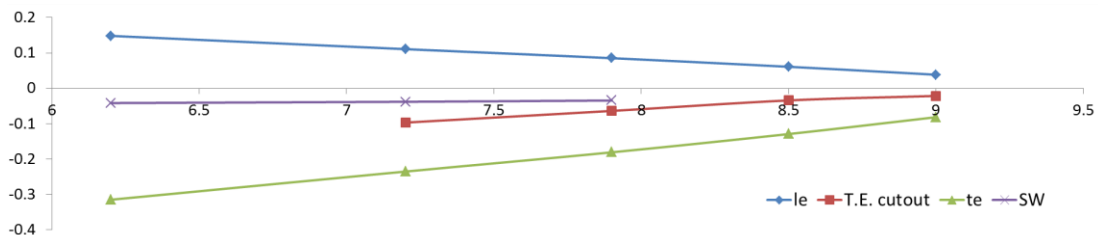
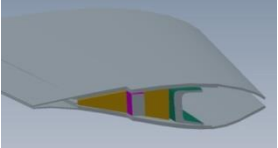
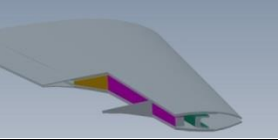
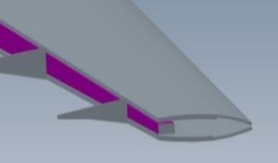


Figure 2.5 Outboard blade planform.

The trailing edge was cut off at the chord locations listed in Table 2.1 and the aft spar was added at the location of the spanwise cut.

Table 2.1 Table of trailing edge changes in PreComp analysis.

PreComp Station #	Span (m)	Chord (m)	Cut off T.E. (%Chord removed)	Schematic (approximate)
4	6.2	0.463	NA	
5	7.2	0.346	40% removed	 <p><i>rib (orange triangle) not included in PreComp models</i></p>
6	7.9	0.266	44% removed	
7	8.5	0.19	50% removed	
8	9	0.12	50% removed	

The following properties of the DB-carbon material were taken from the VectorPly C-BX 1200 material data sheet in Appendix C:

- Infused layer thickness: 0.4064 mm (0.016 inches)
- Density: 1530 kg/m³
- E_x, E_y: 58.8812 GPa
- G_{xy}: 2.55106 GPa

Note: Poisson ratio for the DB carbon material used in the SMART blade was estimated to be 0.32 because the ratio was not readily available on the material data sheet. Final results appeared to be highly insensitive to this estimate (when varied between 0.28 and 0.34).

Table 2.2 lists the layer thicknesses for the glass and carbon laminate materials.

Sectional analysis results presented in Figure 2.6 show that the flapwise and torsional stiffness were maintained with the addition of DB carbon. The reduction in edgewise stiffness was deemed acceptable because the blade design was originally driven by flapwise loads, which caused the edgewise stiffness to be much higher than edgewise loads required. Blade mass lost in the cutout region would be compensated with the mass of the AAD modules.

Table 2.2 Layer thickness for laminate materials.

Material	Single Layer Thickness
VectorPly Carbon DB (SMART Blade-specific) CBX-1200	0.4064 mm (0.016 inches)
DBM 1708*	0.89 mm
DBM 1208* (LE panels only)	0.56 mm
Gel Coat	0.10 mm
3/4 oz. Mat	0.40 mm
CX100_hybrid_triax (spar cap)	3.30 mm

*Note: DBM 1708 and DBM 1208 were modeled using the same material properties, but different layer thicknesses.

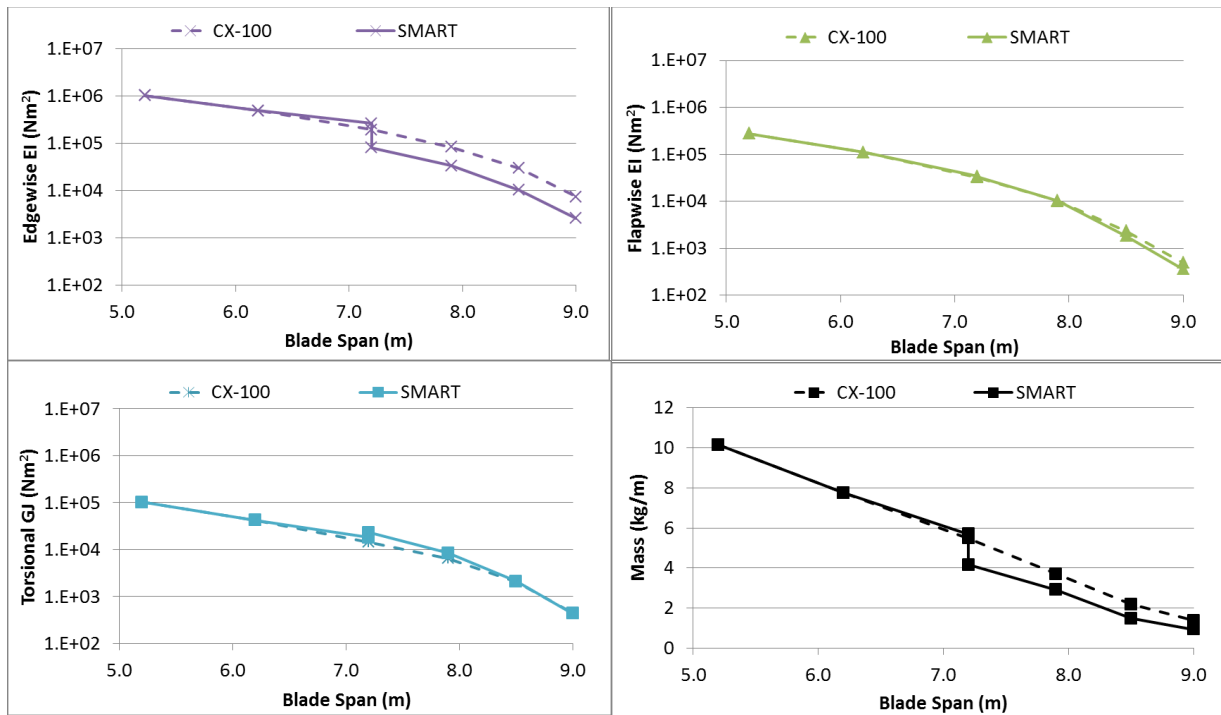


Figure 2.6 Sectional analysis results of original CX-100 and SMART blade.

2.3.3. Final Structural Design

The changes to the blade skin layup which were analyzed in the initial design were manufactured without any additional modifications. However, the designs of the aft spar and inboard rib were altered after the blade trailing edge was removed and the installation procedure for these two components was considered in more detail.

It was decided that balsa or birch core material originally planned for the spar was unnecessary because the gap spanned by the spar was narrow enough to make buckling of the spar unlikely. The change simplified the manufacturing process for the spar and opened up more room for control cables which needed to run within the blade and emerge from feed-thru holes in the spar. The spar took on the shape of a C-channel with flanges about 19 mm wide. The flanges provided sufficient surface area for bonding to the blade shell.

The inboard rib was redesigned because the original concept prevented installation of the aft spar. Keeping with the original purpose of providing a load path between the spar and shear web, the rib was designed to fit between the two members a small distance from the inboard end of the spar. Additionally, the trapezoidal shape required cut-outs for control cables to pass through to the AAD modules.

2.3.4. Finite Element Analysis (FEA) of Final Design

An FEA model of the SMART blade base structure was created in ANSYS using the NuMAD [29] preprocessor along with several modifications within ANSYS. The completed structure is shown in Figure 2.7. The cutout and aft spar can be seen in Figure 2.7 and in Figure 2.8 which shows a close-up view of the high-pressure (HP) and low-pressure (LP) blade surfaces. Also shown in the figures is the introduction of bi-axial carbon along a 45° diagonal in the blade skins.

Figure 2.9 shows the mesh in the area around the modification and Figure 2.10 shows only the main shear web, the aft spar, and the rib that connects the two. In Figure 2.10, it can be seen that the rib was modeled with a semicircular cut-out at each end which, as mentioned above, allow control cables to pass through. Additionally, the mesh density was increased in the area of the rib and adjacent structure to produce more detailed results for the load path between structures.

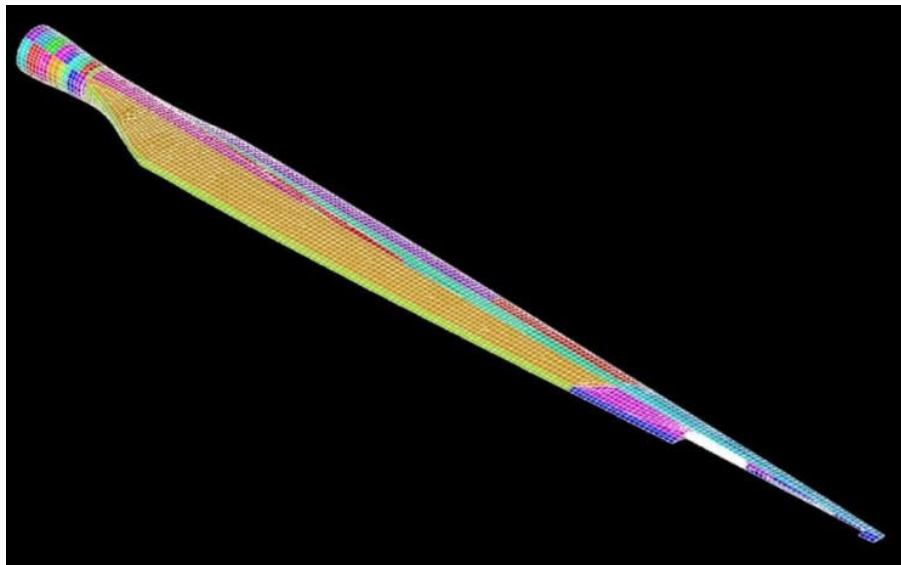


Figure 2.7 SMART Blade FEA Model.

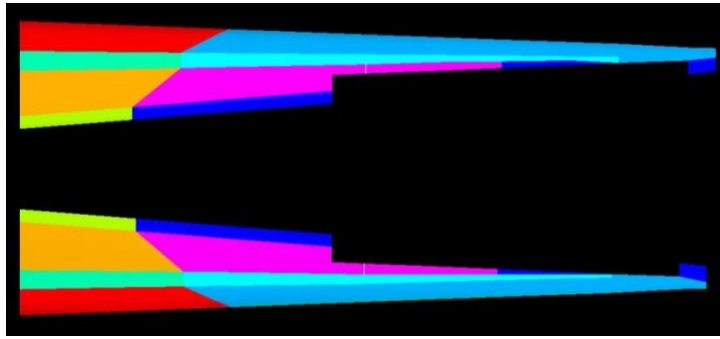


Figure 2.8 Trailing edge cutout modification to model.

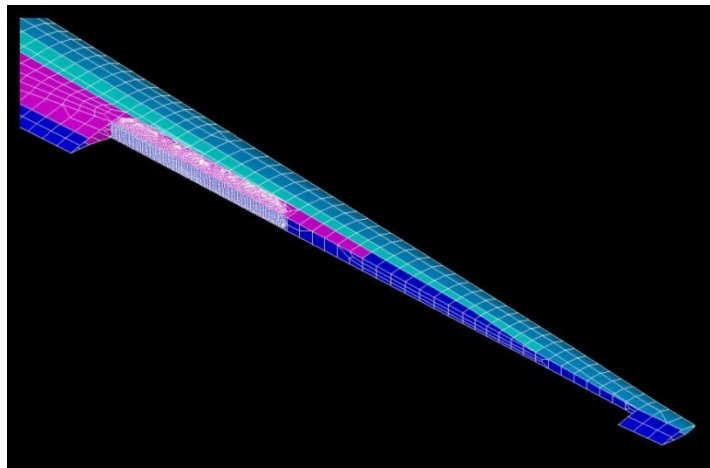


Figure 2.9 Outboard section of model.

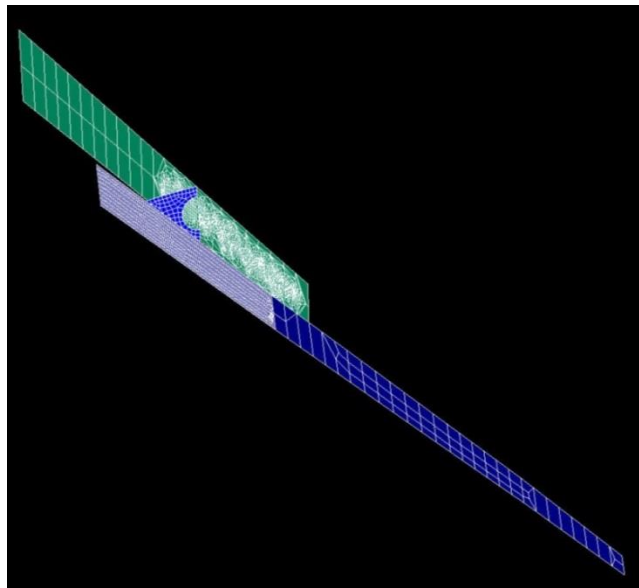


Figure 2.10 Outboard webs and rib with increased mesh density where they interface.

Figures 2.11 and 2.12 show the loads that were applied to the model. The loading was calculated by taking beam loads from FAST [30] operational simulations and converting them to an approximate surface loading using a script developed at Sandia. Additionally, moments were applied at three points along the aft spar to represent the moment load caused by flap operation. For this analysis, two sets of loads were applied to the blade, one set for 12 m/s operation and another for 20 m/s operation.

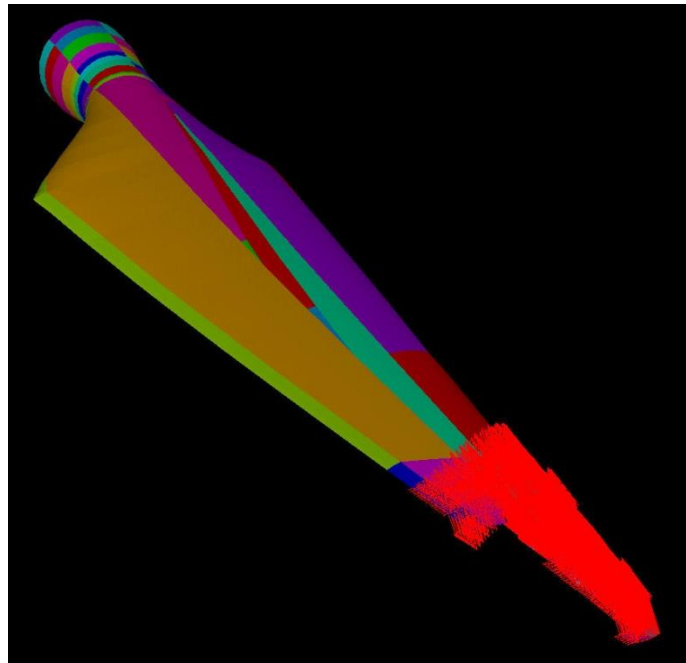


Figure 2.11 Model with loads applied.

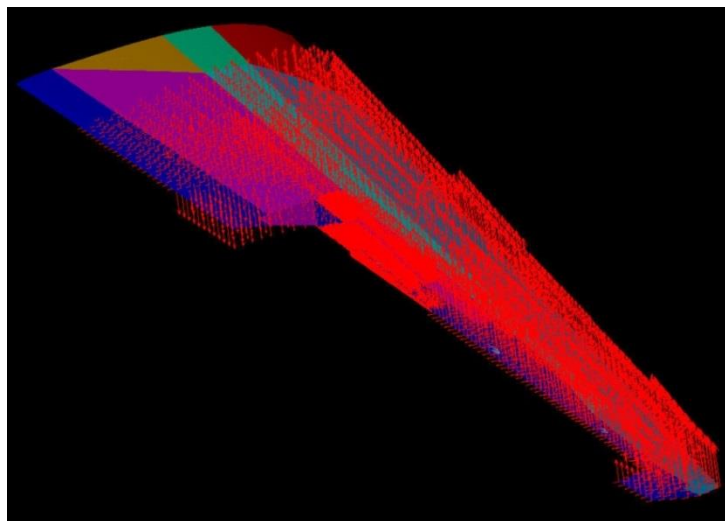
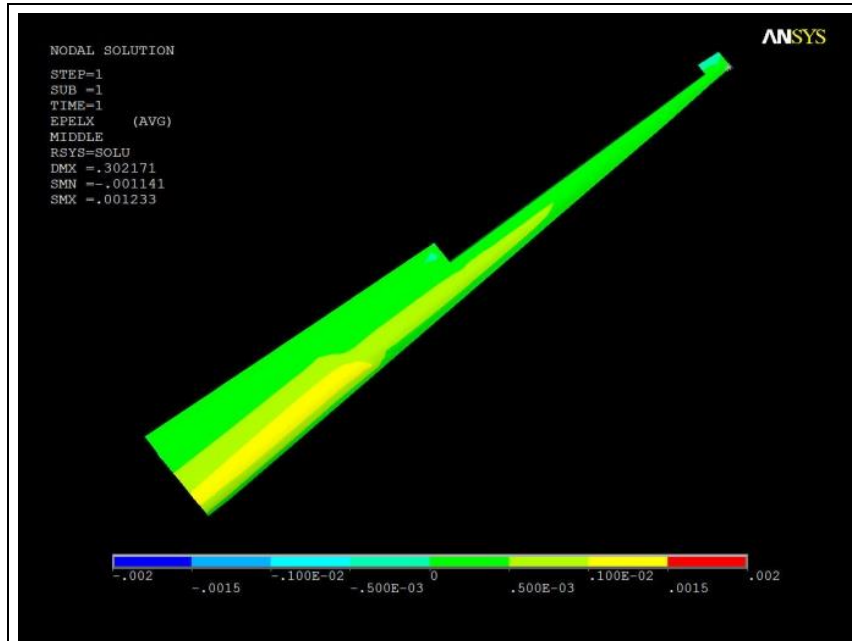
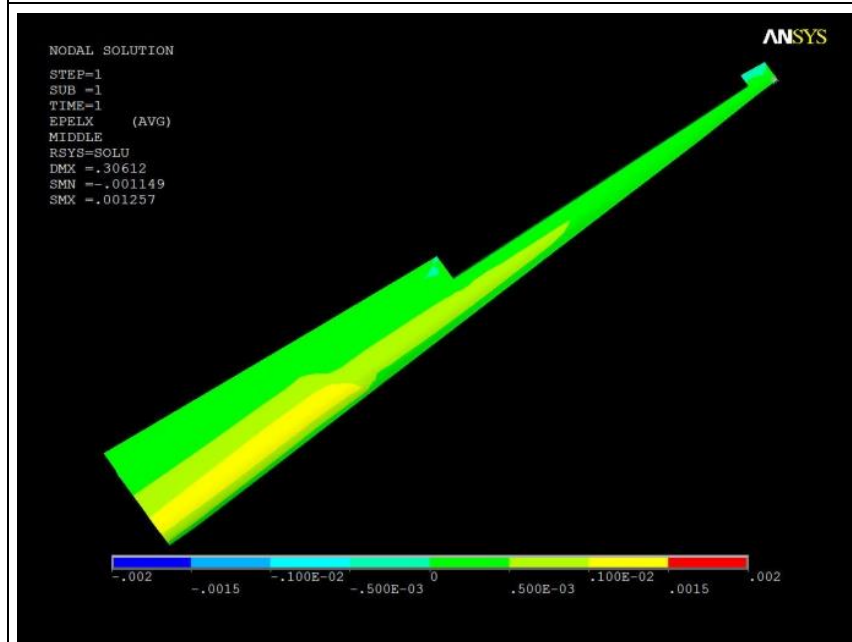


Figure 2.12 Loading applied at outboard section.

Figure 2.13 shows the predicted spanwise strains along the HP surface of the blade at 12 m/s and 20 m/s wind speeds. The tensile strains were shown to be less than 1500 microstrain, which was well within allowable strain limits.



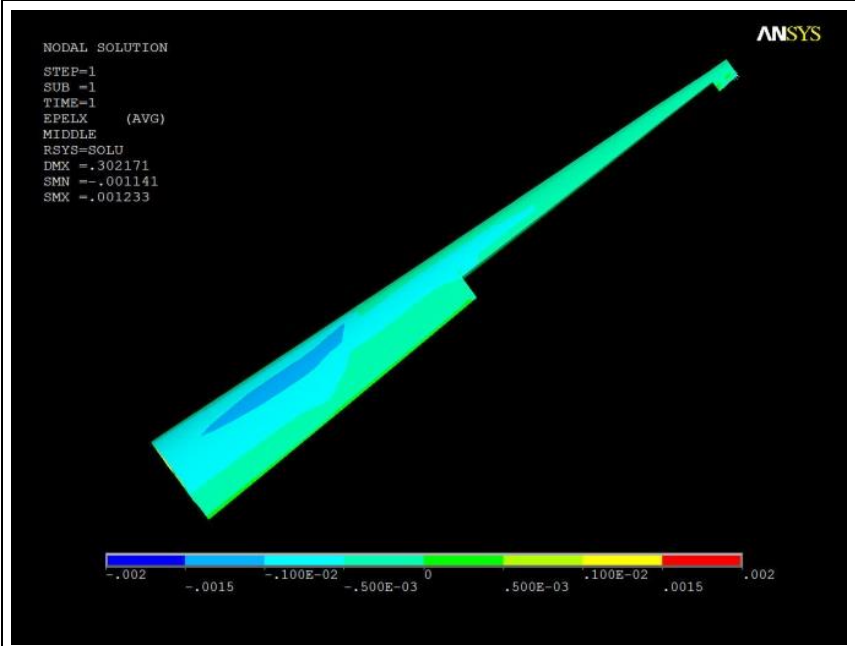
(a) HP spanwise strains, 12 m/s wind speed



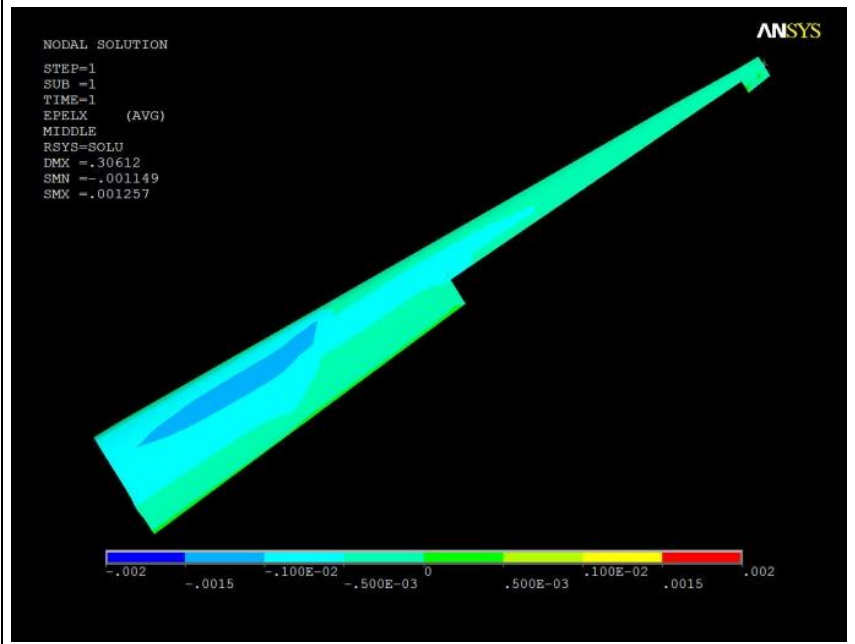
(b) HP spanwise strains, 20 m/s wind speed

Figure 2.13 HP spanwise strains.

Figure 2.14 shows the predicted spanwise strains along the LP surface of the blade at 12 m/s and 20 m/s wind speeds. The compressive strains were shown to be less than 1500 microstrain, which was well within allowable strain limits.



(a) LP spanwise strains, 12 m/s wind speed



(b) LP spanwise strains, 20 m/s wind speed

Figure 2.14 LP spanwise strains.

Figure 2.15 shows the predicted shear strains along the main web at 12 m/s and 20 m/s wind speeds. The strains were shown to be less than 1500 microstrain, which was well within allowable strain limits.

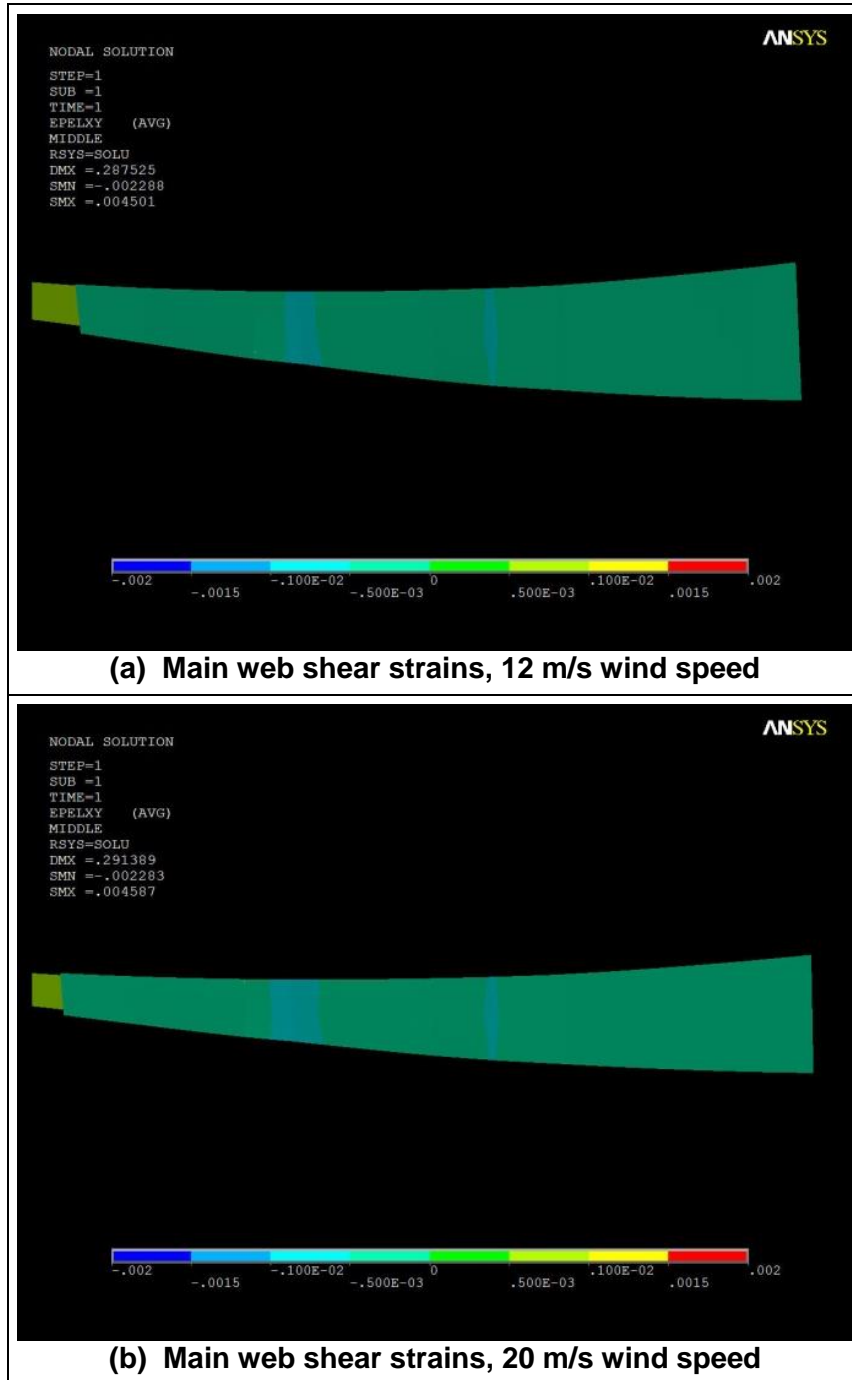


Figure 2.15 Main web shear strains.

Figure 2.16 shows the predicted shear strains along the aft spar at 12 m/s and 20 m/s wind speeds. The strains were mostly less than 1500 microstrain, which was well within allowable strain limits. Note that there were localized high loads near the introduction of the moment loading from the modules. Since the actual blades had multiple attachment points, this was not expected to be a problem. The only area of concern was the inboard LP corner of the aft spar, suggesting that a semicircular cut-out at the end should be considered to gradually introduce the spar stiffness and thereby eliminate the stress concentration.

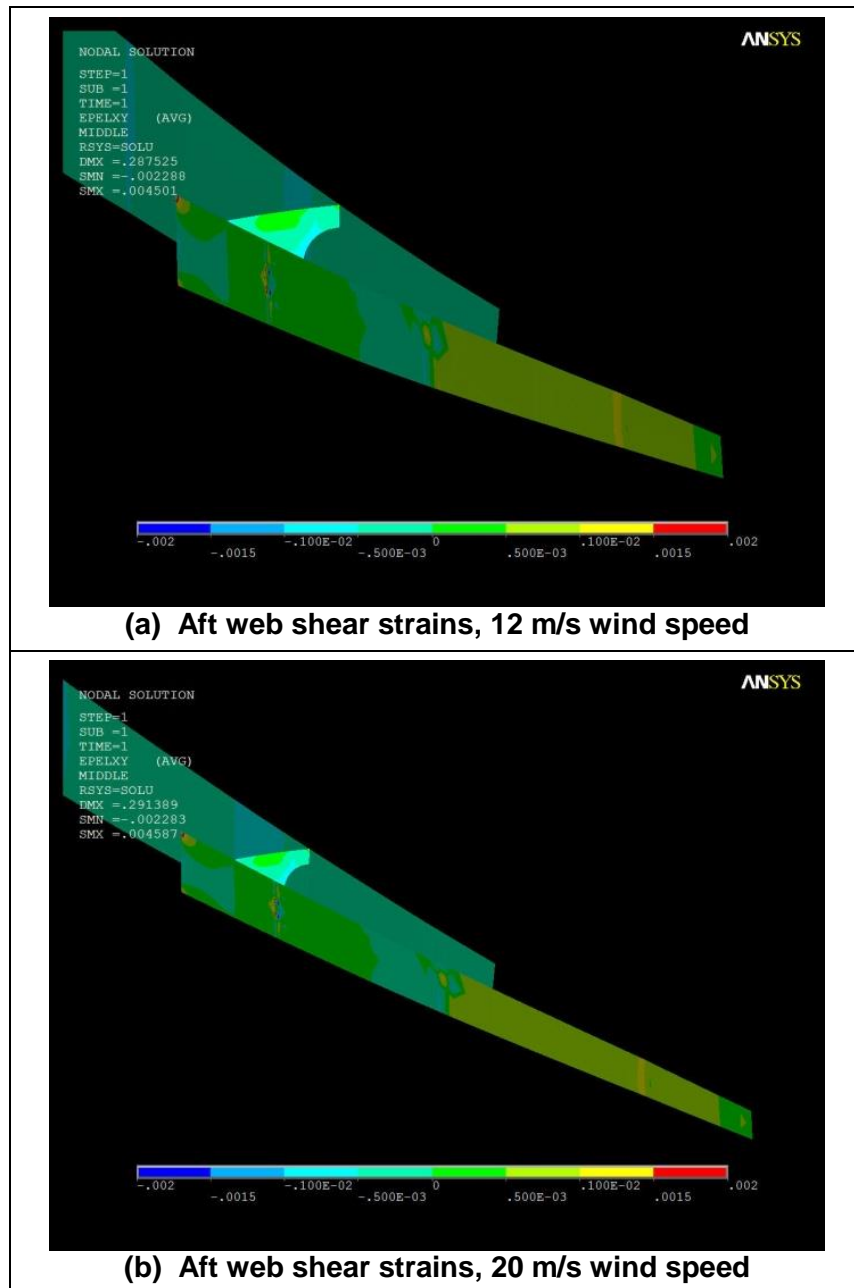
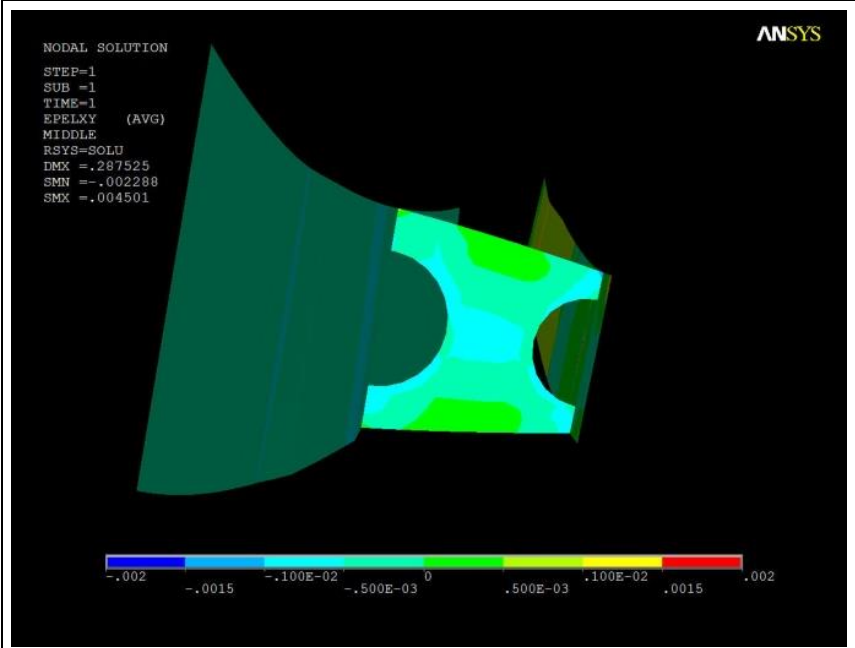
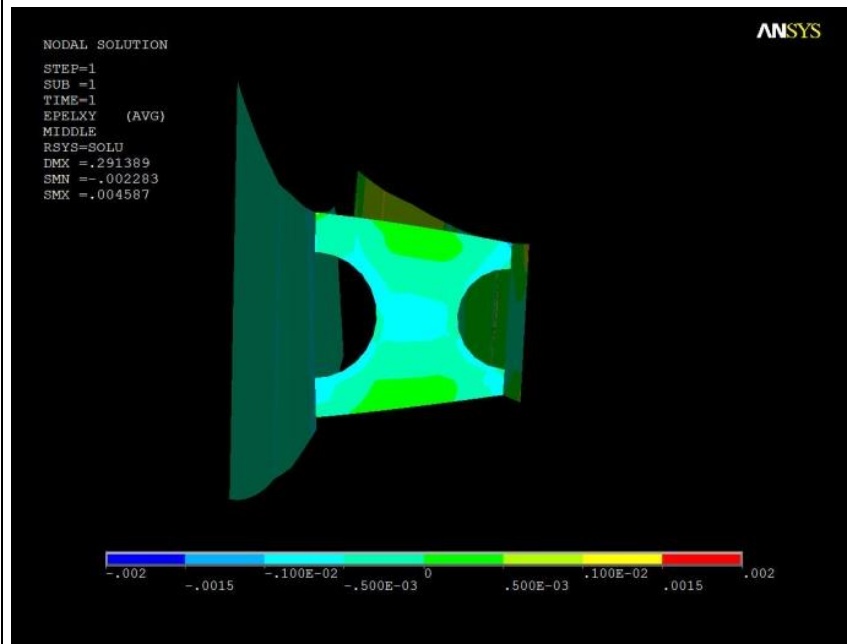


Figure 2.16 Aft spar shear strains.

Figure 2.17 shows the predicted spanwise strains along the HP surface of the blade at 12 m/s and 20 m/s wind speeds. The strains were shown to be less than 1500 microstrain, which was well within allowable strain limits.



(a) Rib shear strains, 12 m/s wind speed



(b) Rib shear strains, 20 m/s wind speed

Figure 2.17 Rib shear strains.

2.4. Maximum Aerodynamic Forces and Moments

The expected aerodynamic forces and moments acting on the flaps and AAD modules were calculated at various flap angles and inflow angles using XFOIL [31]. These loads determined the operating requirements of the flap motors and they were also applied in the structural analysis of the blade and the flap modules.

From the available blade design cross sections, three of them, which were located at 7.0, 7.8, and 8.2 meter span, were chosen for analysis. These locations most closely matched the inboard end (7.03 m), middle (7.94 m), and outboard end (8.86 m) of the AAD blade section. The blade tip geometry was not defined accurately in available documentation and so the 8.2 m span station was chosen as the best approximation.

In the analysis, a “hinge point” was specified at which two forces and one moment were calculated. If the airfoil shape were to be divided at this point, the forces and moment would maintain static equilibrium with the pressure distribution on the remaining airfoil section.

In the final AAD module design, the flap width was 20% of chord. Therefore, in order to calculate the aerodynamic loads on the flap, the hinge point was set to 0.8 (measured from the leading edge in normalized coordinates). The module-to-blade interface occurs at a chordwise location ranging from 0.6 at around 7 m span to 0.5 at around 9 m span and so the “hinge point” was set in this range when calculating loads at the interface.

The forces were reported as two coefficients, F_x (chordwise) and F_y (transverse), which are defined in equation (2.1) where ρ is the air density, V is the local air velocity, and c is the chord length.

$$\text{Force per unit span} = \frac{1}{2}\rho V^2 c \cdot F_x \text{ (or } F_y) \quad (2.1)$$

Similarly, the moment coefficient is defined in equation (2.2). Note that the moment depends on the square of the chord length while the forces have a linear relationship with chord.

$$\text{Hinge moment per unit span} = \frac{1}{2}\rho V^2 c^2 \cdot (\text{Moment Coefficient}) \quad (2.2)$$

The maximum force and moment coefficients with their corresponding angles of attack are given in Table 2.3 for the flap hinge line and in Table 2.4 for the module-to-blade interface.

Aerodynamic loads under specific operating conditions were calculated using these coefficients. The final design of the AAD modules, which the next section describes in more detail, divided the active aerodynamic hardware into three distinct modules. Table 2.5 lists the maximum loads expected on each module under high wind conditions (20 m/s). Module 1, the most inboard module, exhibited the highest loading on the flap. The actuator driving the flap would need to produce up to 1.8 Nm of torque to resist the aerodynamic moment on the flap.

Table 2.3 Force and moment coefficients at flap hinge line.

Flap angle (deg)	Hinge analysis location	Span (m)	Reynolds number	Angle of attack (deg)	Hinge moment coefficient	Fx coefficient	Fy coefficient
20	0.8	7.03	9.60E+05	20	0.019130	0.101142	0.202990
		7.94	9.40E+05	16	0.016733	0.091779	0.176893
		8.86	7.20E+05	14	0.014699	0.082698	0.156081
-20	0.8	7.03	9.60E+05	0	-0.005158	0.019701	-0.113472
		7.94	9.40E+05	-2	-0.006565	0.018700	-0.101908
		8.86	7.20E+05	1	-0.006957	0.012370	-0.109343

Table 2.4 Force and moment coefficients at module-to-blade interface.

Flap angle (deg)	Hinge analysis location	Span (m)	Reynolds number	Angle of attack (deg)	Hinge moment coefficient	Fx coefficient	Fy coefficient
20	0.6	7.03	9.60E+05	20	0.083593	0.080268	0.458252
	0.55	7.94	9.40E+05	16	0.093601	0.068866	0.445795
	0.5	8.86	7.20E+05	14	0.101399	0.061308	0.424054
-20	0.6	7.03	9.60E+05	0	-0.040544	0.004021	-0.258027
	0.55	7.94	9.40E+05	-2	-0.058267	-0.013899	-0.313255
	0.5	8.86	7.20E+05	1	-0.074431	-0.026077	-0.331978

Table 2.5 Calculated forces and moments on each module.

Part	Parameter	Flap (deg)	Module 1	Module 2	Module 3	TOTAL
flap	Hinge Moment (N-m)	20	1.7823	1.1636	0.6604	3.6063
		-20	-0.5441	-0.4406	-0.2853	-1.27
	Drag force Fx (N)	20	28.7078	24.2191	18.8923	71.8192
		-20	5.6712	4.8519	3.3223	13.8454
	Lift force Fy (N)	20	56.9108	46.8735	36.0232	139.8075
		-20	-32.1052	-27.1458	-23.0378	-82.2888
base	Hinge Moment (N-m)	20	8.4222	6.3719	4.1168	18.9109
		-20	-4.4832	-3.905	-2.812	-11.2002
	Drag force Fx (N)	20	22.3997	18.2915	14.0882	54.7794
		-20	-0.5522	-3.2714	-4.4552	-8.2788
	Lift force Fy (N)	20	132.9602	116.9518	94.3956	344.3076
		-20	-80.8724	-80.7335	-70.3299	-231.9358

2.5. Hinged Flap Module Design

2.5.1. Module Components

The design of each AAD module, as mentioned in Section 2.2, consisted of two main pieces: (1) a base piece which housed the motor and mounted to the blade and (2) the flap itself which was attached to the base by a hinge as illustrated in Figure 2.18. A stainless steel shaft ran the length of the hinge and rotated on bronze sleeve bearings contained in the base. The shaft and flap were locked together by set screws in the flap.

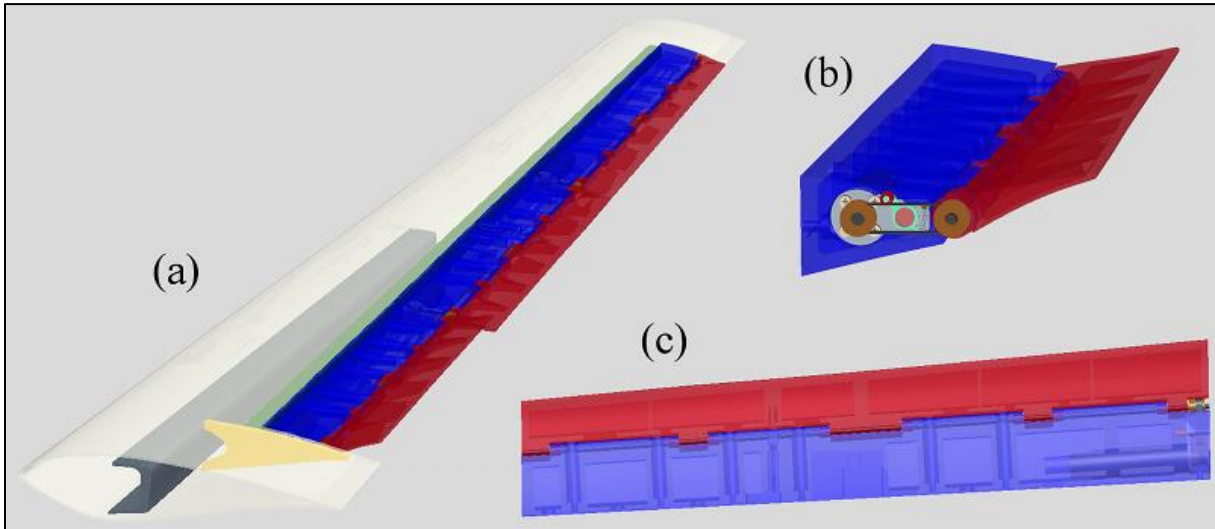


Figure 2.18 Flap module design overview: (a) Three modules assembled with the blade tip. (b) A single module with flap actuated a few degrees. (c) Top view showing the flap hinge geometry.

Given the complex geometry and the need to quickly make design iterations, the design team chose rapid prototyping to manufacture the components. Because the in-house rapid prototyping capability for this project was limited to components no greater than one foot in any dimension, six 1-foot sections were needed to obtain the target AAD length of 20% blade span. As shown in Table 2.5, the total hinge moment on a flap of this length under high winds was 3.6 Nm. Dividing the total length into three separate flap modules reduced the torque demand on each module's drive mechanism and gave the added benefit of individual control over the three sections of flap. Thus each of the three modules consisted of two 1-foot halves joined together.

Design of the module base is illustrated in Figure 2.19. This design was the result of several iterations of analysis, attempts to lower weight, and tests of fabrication capability. Wherever possible, material was removed to save on weight but a wall thickness of at least 0.20 inch was maintained for strength. The base was fastened to the blade using socket cap screws and six long tubes (item {1} in Figure 2.19) provided access for a hex driver to reach the screws. In normal operation, the flap covered these access tubes, but for installation, the flap rotated a full 38 degrees and allowed the hex driver to slide past the flap and shaft.

The inboard end of the module received the motor, and a bracket attached to the motor drive-end held it in place. The walls of the cavity provided lateral support to the long motor body. Motor electrical connections passed through a hole in the mounting face of the base. Sockets spaced along the flap hinge line received bronze sleeve bearings which supported the rotating shaft. As mentioned earlier, each 2-foot long base was fabricated in two 1-foot long pieces.

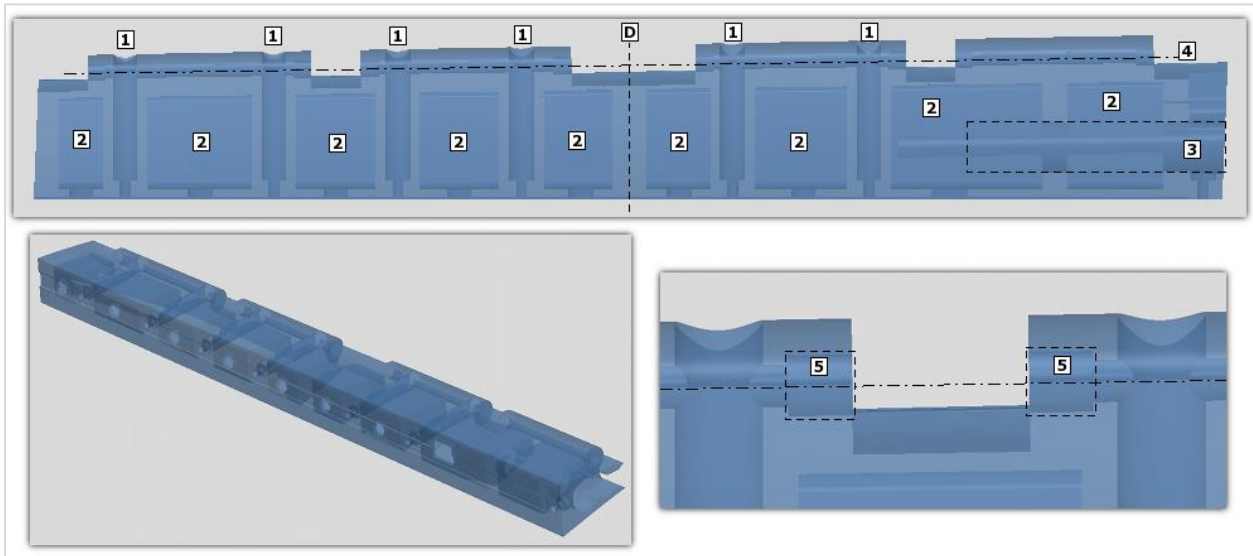


Figure 2.19 Module base design: {D} Dividing line between the two 1-foot pieces of the base. {1} Access tubes to reach socket cap screws which attach the base to the blade. {2} Empty cavities which reduce weight. {3} Motor location. {4} Hinge center line. {5} Pockets which hold the sleeve bearings.

The second module (middle of the three) had additional features not found on the other two modules (see Figure 2.20). Pockets were created to accommodate the installation of accelerometers and pressure taps in the module as well as a Pitot tube in the blade.

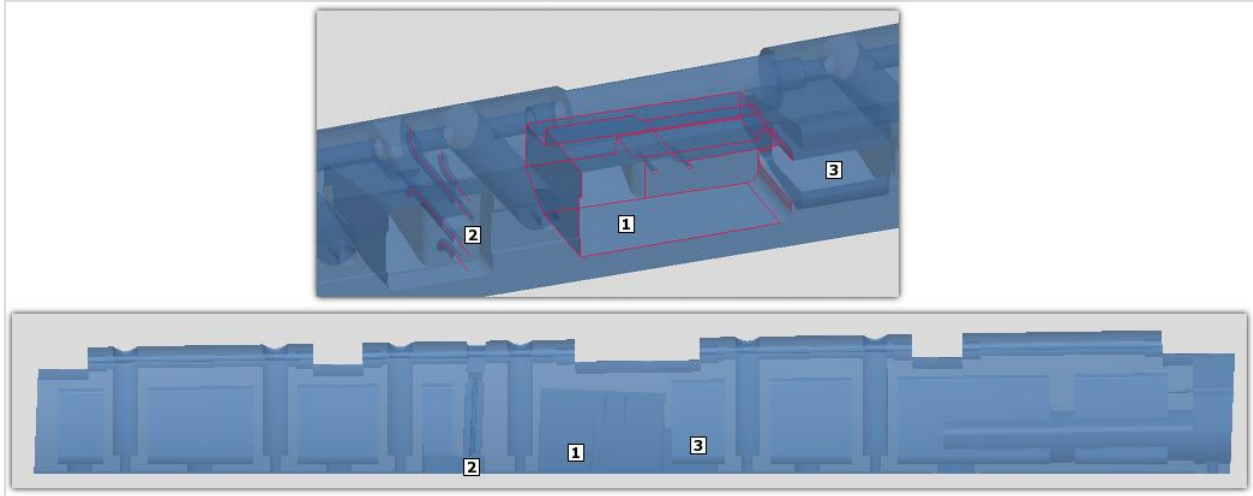


Figure 2.20 Additional features in second module: {1} Pocket for two accelerometers. {2} Channels for surface pressure taps. {3} Pocket to provide extra room for Pitot tube lines.

Design of the flap is illustrated in Figure 2.21. Wherever possible, material was removed to save on weight and reduce moment of inertia about the hinge line, and then ribs were added to maintain strength. Again, each 2-foot long flap was fabricated in two 1-foot long pieces.

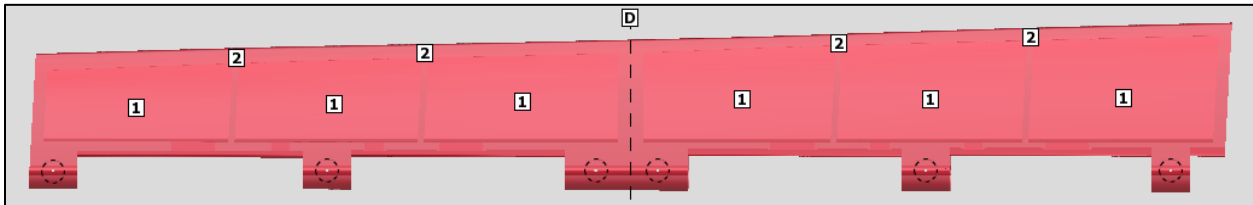


Figure 2.21 Module flap design. {D} Dividing line between the two 1-foot pieces. {1} Empty cavities which reduce weight. Wall thickness is 1/16 inch. {2} Ribs maintain strength. {circles} locations of set screws which hold flap to shaft.

The initial concept for the flap drive mechanism was a timing belt and two pulleys. This design concealed most of the mechanism within the module so that the airflow would not be disturbed by components protruding from the surface. However, the prototyping phase showed that it was difficult to tension the belt. Without tensioning, the belt slack allowed a few degrees of backlash in the flap position.

The belt design was replaced with rigid linkages and control horns as shown in Figure 2.22. The linkage rods were pre-tensioned slightly to reduce play in the mechanism.

Total mass of all three flap modules with motors installed was 3.1 kg while the mass of the blade cutout was approximately 1.5 kg. This doubling of the mass did shift the center of mass in the region by about 10 mm toward the trailing edge, increasing the possibility of blade flutter instability; however, the calculated change in center of mass was deemed to be negligible.

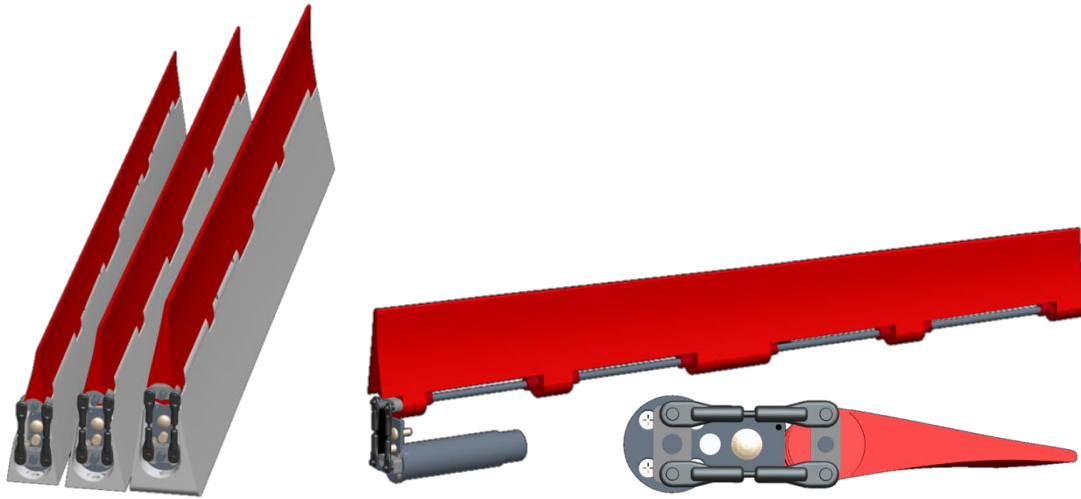


Figure 2.22 Final flap module design.

2.5.2. Required Actuator Torque

Various loading mechanisms were considered to determine the required specifications for the flap actuator. The main contributor was the aerodynamic load which was calculated for steady flow conditions, as presented in Section 2.4. Adjustments were made to account for inertial loading and to provide additional control margin.

The hinge moment for the each module was discussed in Section 2.4 and the maximum value was shown to be 1.8 Nm for the most inboard module at a high angle of attack. At lower angles of attack consistent with normal operating conditions (0 to 12 degrees, see Figure 2.23 which shows the angle of attack distribution at various wind speeds) the hinge moment was about 1.0 Nm for the 20 degree flap position. Besides the static aerodynamic load, an additional torque would be required to accelerate the flap between positions and this torque depends on the inertia of the flap itself. An effort was made to reduce the inertia of the flap about the hinge line and as a result the expected acceleration torque was less than 10% of the static hinge moment for accelerations up to 30,000 deg/s². (For context, a sinusoidal flap motion at 10 Hz with 10 degree peak-to-peak amplitude has a maximum acceleration of around 19,700 deg/s² and maximum speed of 314 deg/s.) Table 2.6 lists the mass properties of the flaps.

Table 2.6 Mass properties of the flaps.

Property	Flap 1	Flap 2	Flap 3
Mass (kg)	1.951E-01	1.442E-01	9.696E-02
CG offset from hinge (m)	2.418E-02	1.918E-02	1.473E-02
Inertia about hinge (kg*m ²)	2.036E-04	9.162E-05	3.556E-05

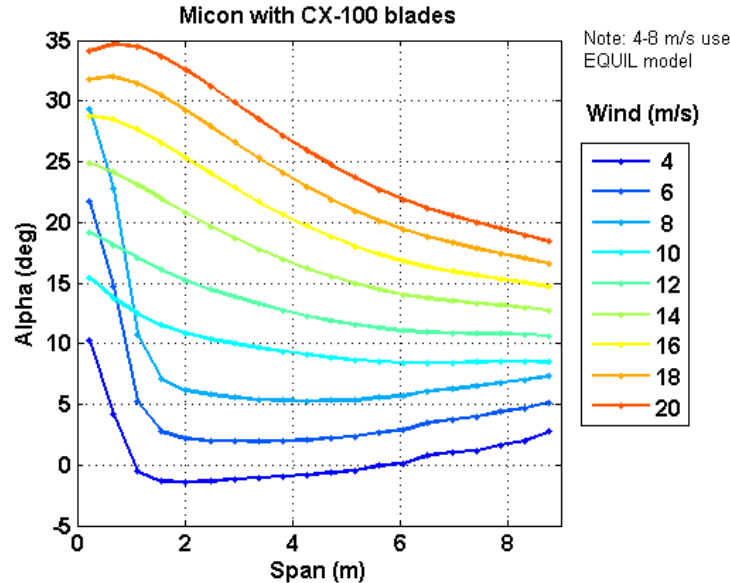


Figure 2.23 Simulated angle-of-attack along blade span in steady wind for fixed-speed fixed-pitch test turbine.

Inertial loading, due to the offset between the flap center-of-gravity (CG) and the hinge line, was the next loading mechanism considered. It can be generated by rotor acceleration, rotor rotation, and blade flapping motion. If the rotor speed increases quickly, the acceleration pulls the flap along by the hinge and the flap CG will tend to fall in line behind the hinge point, which is acceptable behavior. If the rotor speed decreases quickly, the deceleration will push on the flap at the hinge point and so the CG will tend to deflect to either side. This behavior is undesirable but should occur only when the turbine braking system is engaged. An emergency stop with flap position at 20 degrees would generate a hinge moment equivalent to 10% of the static aerodynamic moment at that flap position. The constant rotor rotation also pulls the flap along by the hinge but the inertial effect is on the order of 1% of the aerodynamic hinge moment.

Inertial loading due to blade flapping motion produces the same positive-feedback mechanism which causes flutter instability:

- When the blade tip accelerates downwind, the flap CG tends to remain upwind, thereby increasing the camber.
- More camber generates higher lift forces which again deflect the blade downwind.
- Process repeats until blade stiffness causes the blade to spring back in the upwind direction.
- Feedback cycle occurs on the upwind swing as well due to decreasing camber.

During a blade flapping motion, the torque on the flap is equal to inertial force times the moment arm (perpendicular distance from the flap CG to the hinge line). The inertial force is equal to the mass of the flap times the local blade flapping acceleration. Simulations indicated the maximum flapwise acceleration were about 50, 60, and 70 m/s^2 for the three modules. As a check, one dataset from the Sensor Blade test [26] was examined and the maximum flapwise acceleration at 8m span was 8.1g or 79.5 m/s^2 . Based on this number, the design values were set at 70, 80, and

90 m/s² for the three modules. Table 2.7 lists the resulting moments at 0 degree flap position. These moments are significant compared to the aerodynamic hinge moment.

It was decided that the required actuator torque was at least 1.5 Nm but that an additional buffer should be included to account for the torque required under high winds, dynamic effects not considered in the aerodynamic analysis, and friction in the drive mechanism. A target actuator torque of 3.0 Nm was selected.

Table 2.7 Flap inertial loading due to blade flapwise motion.

Flap	Mass (kg)	Max flapwise accel. (m/s ²)	CG offset (m)	Moment generated (N-m)
1	0.195	70	0.0242	0.330
2	0.144	80	0.0192	0.221
3	0.097	90	0.0147	0.129

2.5.3. Actuator Selection

Electric motors and servos were both considered, but the cylindrical shape of motors was more compatible with the flap module geometry. The electric motor needed a gearhead to obtain the required torque and a shaft encoder to sense shaft motion. Selection of the motor, gearhead, and encoder are described below. Unlike a servo which has integrated control logic, the electric motors also required separate electronic drives to provide position control.

A flap actuation rate of at least 300 deg/s was desired so that unsteady aerodynamic effects could be explored. With this shaft speed and the torque of 3.0 Nm specified in Section 2.5.2, the expected maximum mechanical power was 15.7 W. A general rule, given by motor manufacturers, was that the motor should initially be selected by choosing a power rating around 1.5 times the expected power, or about 24 W in this case.

Using power rating and physical size as the first-pass filter, it was found that one motor and gearhead combination available from Faulhaber met the pre-selection requirements.

Given that the recommended maximum input speed of the gearhead was 4000 rpm and the desired output speed was 300 deg/s (50 rpm), the approximate reduction ratio was 80. There were three reduction ratios available that would work within the space constraints and output requirements: 43, 66, and 86. Figure 2.24 is a plot of motor torque-speed curves with these three reduction ratios. The red curve is an example flap motion profile.

The 86:1 ratio was close to the 4000 rpm input limit and could therefore reduce the life of the gearhead. Also, there was little margin to increase flap rate. The 43:1 ratio appeared too restrictive on the available torque. The 66:1 ratio provided a balance of torque and speed.

Motor selection results:

DC-Micromotor: 2642 W 024 CR (24V nominal input voltage)
Gearhead: 26/1 S, 66:1 (the “S” is for steel input gears, which allow output torque up to 3.5 Nm continuous and 4.5 Nm intermittent)

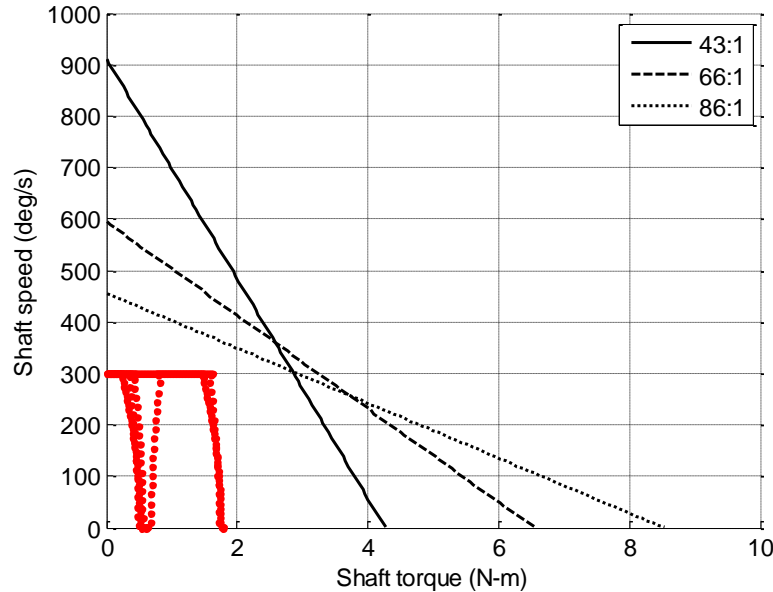


Figure 2.24 Motor torque-speed curves for Faulhaber 2642W024CR, 26/1S

The last motor component to be chosen was the shaft encoder. Because the encoder signal cable would run all the way back to the rotor hub, the encoder needed to have a line driver to provide signal noise immunity. Within the Faulhaber IE3 series of magnetic encoders, various resolutions (lines per revolution) were available.

The maximum encoder input frequency of the motor position controller was 5 MHz. At 6400 rpm (the motor’s no-load speed), an encoder with 1024 lines per revolution would produce 109,000 pulses per second. This frequency was far below the 5 MHz limit and so there was no concern about exceeding the position controller’s maximum input frequency.

With the 66:1 gearhead, the shaft positioning resolution for 512 and 1024 count encoders were 0.0027 degrees / quad count and 0.0013 degrees / quad count, respectively. The term “quad count” refers to quadrature decoding which provides four pulses per encoder count. Either resolution provided more than enough precision, and so the IE3-512L version was chosen.

2.5.4. Module Stress Analysis

A stress analysis was performed to verify the strength of the modules under expected loads. Both the flap and the base were fabricated using a rapid prototyping printer which builds up layers of P400 ABS plastic. The raw plastic filament had a density of 1.05 g/cm³ and a tensile strength of 5000 psi (34.4 MPa).

The model geometry for each module was imported into ANSYS directly from the Pro/Engineer solid model. Within ANSYS workbench, a point mass was added to represent the motor mass. Supports were added to represent how the modules were mounted to the blade and also to simulate the operational loads experienced by the flap and base. A force applied at the fastener holes modeled the fastener preload. Compression-only reactions were defined at the blade-module interface. Cylindrical supports defined at the fastener holes provided resistance to lateral movement.

The forces listed in Table 2.5 were applied to simulate the flap forces at the hinge line and on the base itself. In addition to the aerodynamic forces, blade rotation and blade “flapping” acceleration were simulated. By iterative analysis, the required preload in each socket cap screw was found to be 200 N. Stress in the modules was found to be only 5 MPa at most, well within the limits of the ABS plastic.

3. BLADE CONSTRUCTION AND DEVICE INTEGRATION

3.1. Instrumentation Plan

Sandia has developed several new sensor optimization strategies and state estimators to maximize the performance of the overall controls observer (a measurement or quantity computed from measurements) and minimize the number of sensors required, subject to the assumption that it is absolutely critical to observe the complete rotor dynamics. The enhanced technology incorporated in these sensor optimizations includes a Modal Filter for stochastic monitoring, a patented static blade deflection estimator based on centripetal acceleration, and order analysis for the deterministic monitoring of structural response. All of these methods are discussed by White [25] and White, Adams, and Rumsey [26]. The number and locations of the accelerometers were driven by sensor optimization strategies that account for expected rotor loads, deflections, modal contributions, mass and stiffness distributions, and co-locations with other measurements for multi-physics observers.

Applying these optimizations resulted in single triaxial and uniaxial accelerometers placed at both the 2 m and 8 m locations in each blade to permit estimation of linear deflections and spanwise rotations. The strain sensors were located at the root, 25%, 50%, and 75% of blade spanwise length to enable accurate capture of the curvature along the blade for the application of shape reconstruction force and deflection estimators. The measurements at these locations also enable training of a modal filter for the application of multi-physics observers. Single metal foil and fiber-optic strain gauges were mounted at each of these locations to enable comparison of the performance of the two technologies. SNL has been performing metal-foil strain measurements of operational rotor blades for nearly four decades, but these sensors have never demonstrated the long-term reliability that would be needed for utility application. Fiber-optic strain measurements, on the other hand, are a fairly recent application for SNL, but they have been shown to continue to perform well at cycle counts well above those which are expected in the 20-year life of a turbine rotor blade. The fiber-optic temperature sensors will be used to study the correlation between rotor blade temperature and structural performance, hopefully yielding crucial insight into the role of temperature in the “noise” or randomness that is typically observed in the strain signals recorded during online structural health and condition monitoring.

3.2. Mitigation of Electrostatic Discharge

Previous sensor demonstration efforts by White, Adams and Rumsey [26] have shown that electrostatic discharge (ESD) is a field-test hazard that is a major contributor to sensor failure, particularly to accelerometers. The most well-known manifestation of ESD is lightning; to handle the large currents associated with lightning, a large copper cable was installed inside each SMART blade, connecting a lightning receptor located near the blade tip and the metal hub. This lightning protection was not present on the CX-100 blades but is a common feature included in most wind turbine blades manufactured today. The ESD problems cited above, however, occurred mainly in the absence of lightning, most likely due to the triboelectric effect [32], the static build-up of charge due to the contact and separation of dissimilar materials. Air passing over turbine blades is an example of this effect; it can result in the accumulation of very large charges that can vary significantly along the blade, leading to discharges from one portion of the

blade to another or to ground. Three features were included in the SMART blades in an attempt to address this issue. First, fine wire mesh was added to the outside of the carbon laminate and a conductive gelcoat coating was applied to the entire blade surface at the time of fabrication. Both were grounded via the lightning protection cable. Also, while not intentionally designed to be an ESD mitigation mechanism, the conductive carbon fiber laminates in the outboard 2-meters of the SMART blades do provide ESD dissipation. Second, more robust accelerometers with a much higher tolerance to ESD than those used in the prior efforts were used. Third, the accelerometers were mounted on orientation/grounding blocks that serve the dual purposes of orienting the sensor accurately and grounding the accelerometer housing via a cable to the rotor hub.

3.3. Blade Construction

The SMART blades skins were fabricated by TPI Composites at their Rhode Island facility in June 2010 using the original CX-100 molds and a vacuum infusion process with epoxy resin. In early October 2010, SNL staff traveled to the TPI facility to install the instrumentation packages. Each blade was instrumented with an internally-mounted array of accelerometers, fiber-optic strain gages, metal foil strain gages, fiber-optic temperature sensors, pressure taps, and mounting hardware for a Pitot tube. Placement of the structural sensors is summarized in Figure 3.1.

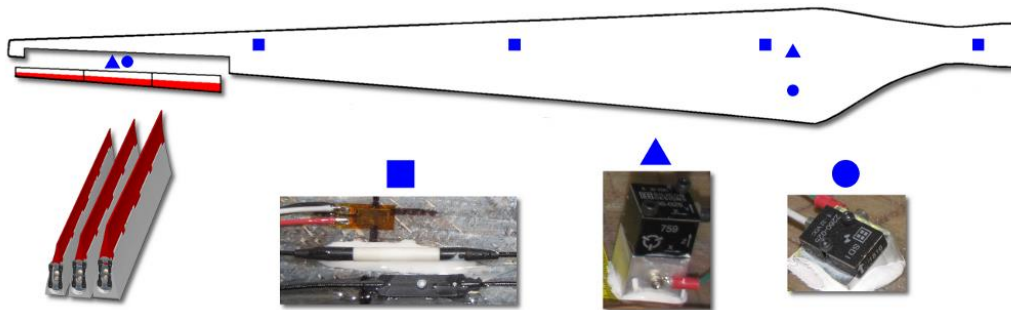


Figure 3.1 Schematic of internal sensor locations. (Square) co-located foil strain, fiber-optic temperature, and fiber-optic strain. (Triangle) tri-axial accelerometer. (Circle) uni-axial accelerometer.

The aerodynamic measurements were installed at approximately 7.9 m (the center spanwise location of the aerodynamic modules) on each blade. These measurements included a traditional five-hole Pitot tube for determining angle of attack and velocity (planned for only one blade), as well as an array of pressure taps to measure the chord-wise distribution of surface pressure. Two modifications were made to minimize the difficulties that past users of similar aerodynamic measurements have experienced. First, the Pitot tube was built with an integrated bend to place it at the nominal angle of attack orientation to maximize the angular range and accuracy of the measurement. Second, a highly accurate absolute pressure sensor was located in each blade to measure the reference pressure, eliminating the complexity associated with the pneumatic slip-ring required for the usual hub-mounted absolute pressure reference. Unfortunately, difficulties were encountered with the pressure scanner itself and none of the aerodynamic measurement capabilities were utilized during the field test.

Upon completing installation of the sensor arrays, TPI closed the blades and performed final surface finish work. The blade set was then shipped to SNL in Albuquerque, NM.

3.4. Post-build Blade Modification

After receiving the blades from TPI Composites, SNL staff began modifying the blade structure so that the active control modules could be installed. The first step was to remove the portion of each blade corresponding to the intended location of the AAD modules. A CAD model of the geometry provided the surface measurements needed to accurately define the cutout, and ruled adhesive tape with millimeter markings provided the means of making these measurements. The most difficult challenge in drawing the layout lines was accommodating the variation among the three blades. Although the blade skins all came from the same mold, variations in material placement, assembly, and finishing operations resulted in noticeable differences in blade tip geometry and airfoil thickness.

An oscillating “multi-tool” with a semi-circular cutting attachment cut through the skin material (approximately 3 mm thick). This tool was easy to control, accurate, and generated very little dust (although it was still necessary to have appropriate respiratory protection while cutting glass and carbon fiber). Figure 3.2 shows the blade set with the trailing edge sections removed.



Figure 3.2 Top: blade set after removal of 6-foot section. Bottom: close-up of cavity showing surface pressure tap tubing and lightning cable.

The next step was to build the aft spar which bridged between the upper and lower skins of the cavity and provided a flat surface for mounting the AAD modules. The CAD software model of the blade geometry provided enough information to develop a rough initial design of the component which was then refined after the trailing edge had been removed. The initial design

was similar in concept to the main shear web of the blade: it had a C-channel shape with birch plywood core sandwiched between layers of biaxial carbon. However, upon removing the trailing edge cutout, the initial design was changed in two major ways. First, the cavity of each blade was measured and the spar's flanges were modified to accommodate interior protrusions such as the lightning protection system and surface pressure taps. Second, it was decided that the birch plywood core would complicate the fabrication and was actually unnecessary because the gap spanned by the spar's web was small enough that carbon laminate alone would provide sufficient resistance against buckling of the web.

A mold for the spar was constructed which established the tapering geometry of the C-channel and included features such as cable pass-thru holes and attachment point holes. This approach allowed these features to be located accurately relative to one another and relative to the overall shear web geometry. Attempting to add these features by drilling and machining after the part was formed would have made fixturing and locating the part difficult. Four layers of Vector Ply C-BX 1200 biaxial carbon cloth were placed in the mold, orienting the biaxial fiber directions at +45 and -45 degrees relative to the centerline of the mold. In especially thin areas, strands of uni-axial carbon fiber were added as reinforcement. The dry materials were then vacuum-infused with Hexion resin (system MGS RIMR 135 / RIMH 1366) to create the composite part. The final step in completing the shear webs was to add the attachment point hardware, which was #8-32 threaded nutplates from Click Bond (part numbers CN609CR08 and CN614CR08). These nutplates are designed so that the base bonds to the composite surface while the threaded portion is able to "float" a small amount within the base. This movement provided the leeway required to align the modules when attaching them.

The spar was then bonded into place using Hexion structural adhesive (system BPR 135G / BPH 137G). Achieving proper alignment of the spar was critical in this step because it determined how well the AAD modules would align with the surrounding blade surfaces. Because the spar could twist and flex, a rigid jig which ran the full length of the spar was created from a piece of aluminum bar stock. Alignment of the spar was accomplished with thin templates, placed at each end of the jig, which represented the shape of the flap modules and could be aligned with the surrounding blade surfaces. During the spar installation process, the motor control cables and the accelerometer cables were routed through the spar feed-through holes. The surface-tap pressure tubing was also routed within the blade cavity. Immediately after applying the adhesive, a pre-cure was performed at 50 °C for 1 hour. The adhesive was post-cured at 75 °C for 4 hours. Figure 3.3 shows the spar bonded in place and call-outs for a few module attachment points and a cable feed-through.

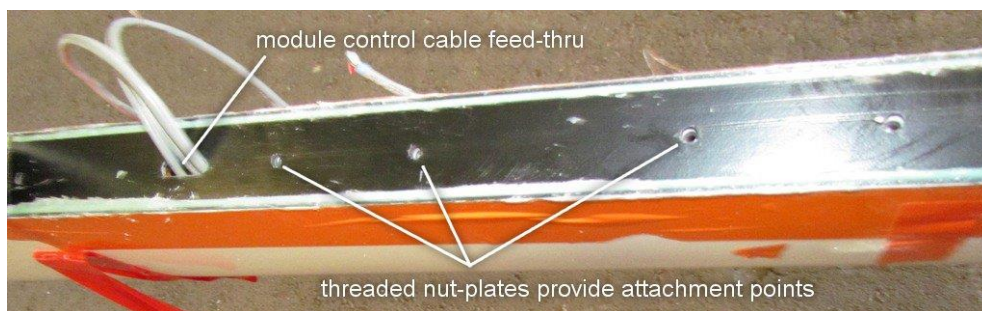


Figure 3.3 Aft spar bonded into place.

3.5. Flap Module Construction and Integration

The flap modules were fabricated using a fiber deposition modeling (FDM) rapid prototyping printer which produces complex geometry by building up layers of material. The surface quality of the parts was fairly smooth and depended somewhat upon the orientation of each face with respect to the deposited layers. To produce a better finish with surface roughness closer to that of the blade skin, the modules were sanded with fine-grit sand-paper. Two coats of clear UV-resistant spray paint were then applied to the parts to reduce degradation of the plastic in sunlight.

Weather resistance was added to the motors by applying Plasti Dip® to the control wires where they protrude from the motor encoder and also encapsulating the entire encoder assembly. The connector which joined the motor to the blade control cables was also sealed to keep water away from the electrical contacts. At the root end of the blade control cable, a waterproof reverse bayonet connector (Spacecraft Components part number SCPT07F12-14S) brought the signals into the control box.

After all nine modules were fully assembled, each module was attached to the appropriate location on the blade spar with six #8-32 cap head screws. Before tightening the screws, each module was positioned to align it as well as possible with the adjoining blade surfaces. Any remaining mismatch between the blade and module surfaces was smoothed out using a flexible filler compound. Figure 3.4 shows the completed blade set.



Figure 3.4 Fully assembled SMART blade set.

4. CONTROL HARDWARE

Three levels of control loops governed operation of the flap AAD modules. The first and lowest level of control was the actuator control loop. This loop was responsible for driving the motors so that their shaft angles remained near the setpoints commanded by the master controller. The second level of control sat above the actuator control loop and was responsible for transitions between various system operating states. This loop can be called the state controller. The third level of control was the master controller which was responsible for generating the position setpoint command for each flap module.

The actuator control must operate at a high loop rate and must be able to respond to disturbance inputs acting on the motors. This means that the shaft angle must remain near the setpoint for any torque load on the shaft, whether it is zero, constant, or variable. The exact magnitude and characteristics of this torque input are unknown and therefore it is regarded as a disturbance entering the actuator control loop. Motor positioning control units are available to handle this low-level control task. If the motors were replaced by servos, the control logic and electronics would be very similar but would be integrated with the motor package rather than existing in a separate drive package.

There were nine drive units to control the nine motors on the rotor. The drive units were Maxon EPOS2 24/5 positioning control units. This motor driver can supply 5 amps continuously and 10 amps intermittently at 24 volts; the motors were expected to require less than 2 amps for most flap motions and loading conditions. In this motor driver, the actuator control loop has a switching frequency of 50 kHz (this is the rate at which the drive pulses power to the motor) and a positioning controller update rate of 1 kHz. The position controller is a proportional-integral-derivative (PID) regulator with feed-forward gains on velocity and acceleration. The Maxon EPOS Studio software provided a utility for automatic tuning of the PID gains. In addition to the position control function, each EPOS2 unit implemented safeguards and limits to keep the motor within a specified operating range. The drive units also monitored and reported to the data acquisition system the shaft angle and current draw of each motor.

The state controller was responsible for keeping all of the motor drives in the same operating mode and responding to state transition commands from the top level master controller. Whenever the turbine control system powered up, the state controller would initiate communication with the motor drives and cause the flaps to hold their current positions. When signaled by the master controller, the state controller then caused the motor drives to perform a homing operation to re-establish the zero flap angle position. After verifying the homing operation was complete, the state controller would then wait for the master controller's signal to begin accepting position commands. The state controller was always running and handling drive faults, even when the master controller was idle or being reconfigured. The state controller was implemented in a set of three microcontrollers so that each microcontroller had to communicate with only three of the nine motor drive units.

The third level control loop was the master controller. In addition to the signaling operations which have already been mentioned, the master controller was responsible for generating the position setpoint command for each flap module. For open-loop control this was either sinusoidal

motions or step movements. For closed-loop control it would take information from the rotor sensor network and continually make flap control decisions according to the programmed control law. The master controller was implemented with an Athena single-board computer from Diamond Systems and was programmed within the Matlab/Simulink xPC Target framework. The Athena provided analog-to-digital and digital-to-analog conversion as well as digital I/O interfaces. Position control commands had to be given to the motor drives via analog signals because the Athena could not send RS-232 messages fast enough to all nine motor drives. Switching to a faster communication protocol such as CAN bus may have resolved this problem, but resource restrictions prevented its implementation during the project.

Figure 4.1 is a picture of the control box. Three power supplies are located at the top. In the second row of components the nine Maxon motor drives are located at the left in two stacks. The enclosure of the Athena single-board computer is in the middle, and the microcontrollers are located within the gray enclosure. The block box atop the gray enclosure is a network-to-serial communication converter. Lightning protection on all input lines and terminal blocks for making connections are located in the bottom half of the control box.

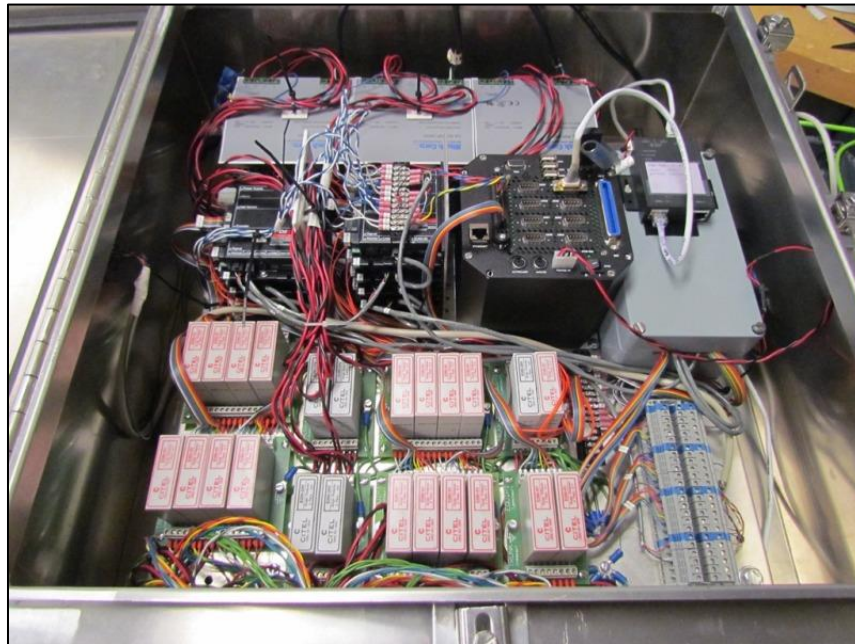


Figure 4.1 AAD control box.

5. FIELD TEST

5.1. Layout of the Test Site

The test turbine was located on the USDA-ARS site in Bushland, Texas. The region is characteristic of the U.S. Great Plains with essentially flat terrain and the test site itself is surrounded by farmland. As illustrated in Figure 5.1, the northwest corner of the site has a reservoir surrounded by an approximately 1.2-m (4-ft)-high berm.

The primary wind direction at the site is from 224° with respect to true north, 215° with respect to magnetic north. The wind rose for this site shows a secondary peak for winds from approximately due north.

As shown in Figure 5.2, three turbines were positioned at the site in a straight line across the prevailing wind direction. The towers were labeled 1, 2, and 3 and the nacelles were labeled A, B, and C. Upwind of the turbines (with respect to the southwest prevailing winds) were five meteorological (met) towers. The SMART rotor was installed on turbine B and only the center three met towers upwind of turbine B were used. For the secondary prevailing wind direction (approximately north) another meteorological tower was used. The nomenclature used to designate each of these towers is given in Figure 5.2.

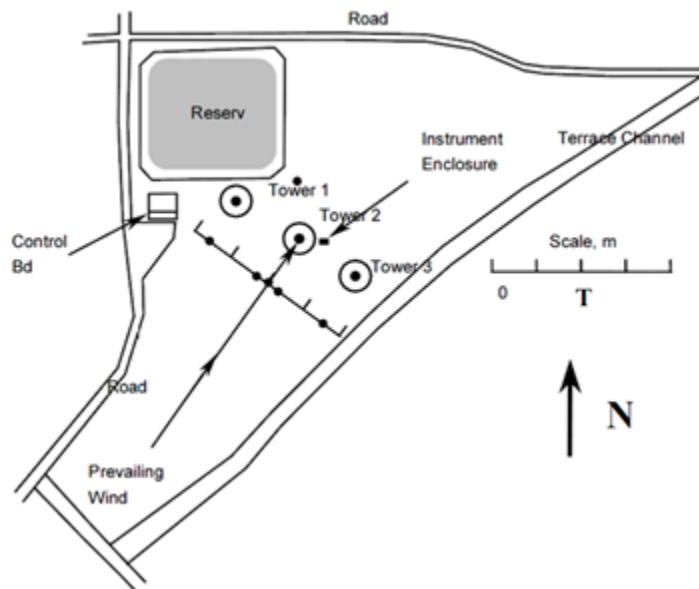


Figure 5.1 Schematic overview of the test site.

Two buildings were located on the test site (see Figure 5.1). The main “Control Building” was west of Tower 1. A small “Instrumentation Building” was located east of Tower 2. The latter building provided environmental protection for a number of signal processors and wiring junction points in the data system. Neither the reservoir nor the buildings obstruct the inflow to

the turbines from the prevailing wind direction. For inflow from the secondary wind direction (north), the turbines also have an unobstructed inflow.

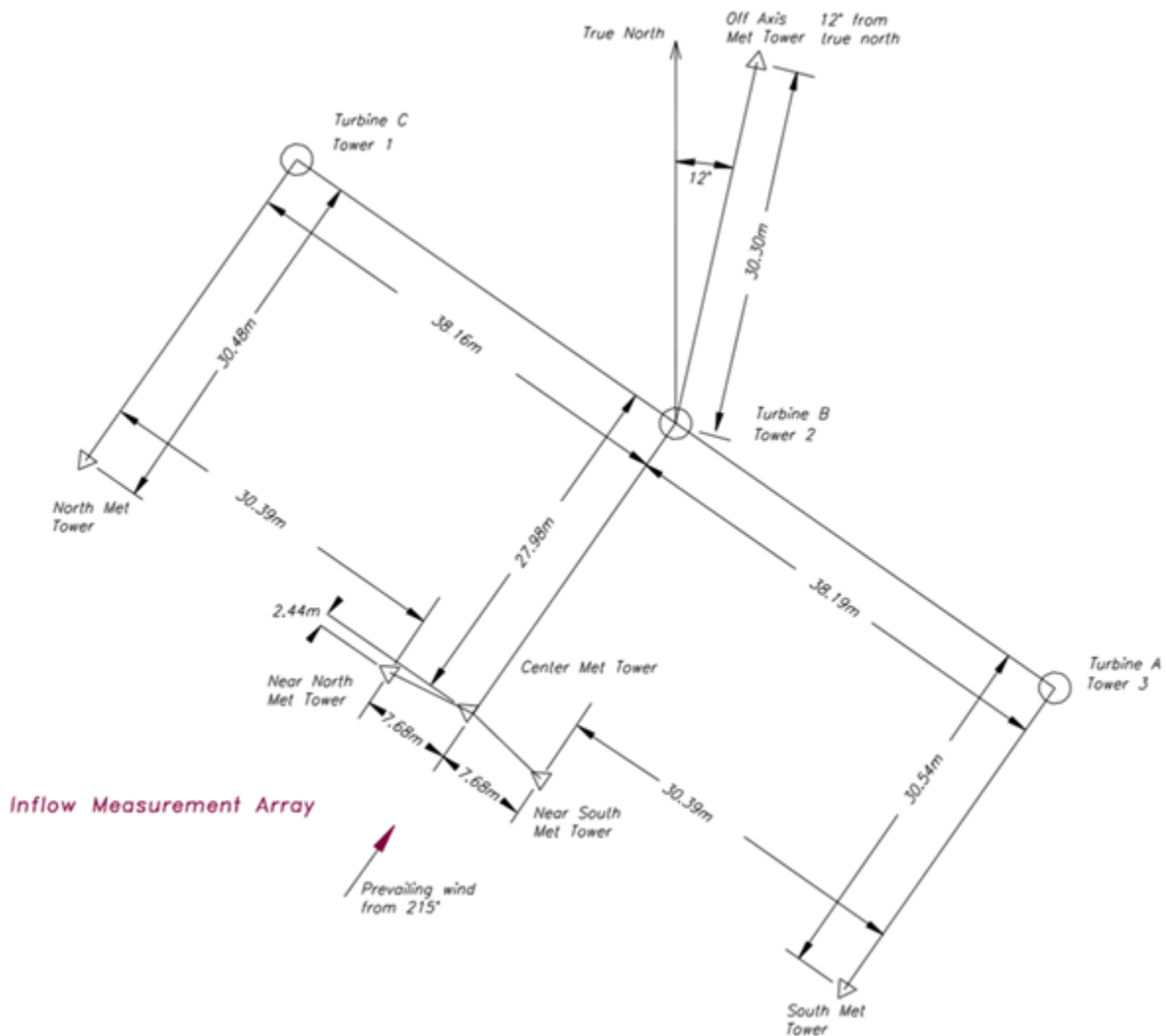


Figure 5.2 Site plan with detailed dimensions.

5.2. Test Turbine

The three turbines at the test site were modified versions of the Micon 65/13 turbine (65/13M). Each turbine was designed as a three-bladed, fixed-pitch, upwind turbine with an induction generator. At hub height, the turbine stood 23 m (75 ft) tall on a tubular, three-piece steel tower that weighed approximately 64.5 kN (14,500 lb). The nacelle weight was approximately 42.7 kN (9,600 lb).

The turbines were retrofitted machines that ran in the Palm Springs California area for approximately 15 years. During that period, several turbine subsystems were modified to increase performance and reliability. Modified subsystems include the brakes, gearbox, generator

and blades. The new drive train was built around an induction, three-phase 480v generator rated at 115 kW. The generator operated at 1200 rpm while the blades turned at a nominal 55 rpm (the standard Micon 65/13 turbine rotated at 45 rpm). Around 2007 at the Bushland test site, a second retrofit of the machine was conducted in which several components were heavily modified including: new brakes, faster sensors, new safety infrastructure, and new control algorithms.

The Micon turbine used in this test campaign was Turbine B (Tower 2). The blades measured 9 m (354.3 in) in length, yielding a rotor diameter of 19.3 m (63.3 ft). The hub flange for mounting the blades was located 599 mm (23.6 in) from the centerline of the low-speed shaft and provided only fixed-pitch operation of the blades.

5.3. Instrumentation

The turbine and the meteorological inflow at the Bushland test site were monitored with a total of 144 instrument channels: 111 to characterize the blades and flaps, 16 to characterize inflow, and 17 to characterize the turbine.

A complete list of the 144 instruments is presented in Appendix F.

The pressure taps on the blades and the Pitot tube were not utilized in the field test due to difficulties with the pressure scanner.

5.4. Test Cases

Six types of flap motions were employed during testing:

- 1) Sine(A, f), at prescribed amplitude A and frequency f
- 2) Sine series(A), at prescribed amplitude A with sequence of seven frequencies: {0.1 Hz, 0.2 Hz, 0.4 Hz, 0.8 Hz, 1.5 Hz, 3 Hz, 6 Hz}
- 3) Sine sweep(A, T), at prescribed amplitude A with logarithmic frequency sweep from 0.1 Hz to 10 Hz over time period T
- 4) Steps(A, d), between 0 degree position and prescribed angle A , with hold duration d
- 5) Step series(d), with a sequence of step motions between the 0 degree position and $\pm 5, 10, 15$, and 20 degrees and hold duration d before next step motion.
- 6) Static angle

Initial shakedown of the data acquisition and flap drive system was recorded in the February 1st and 10th data files. The rotor was turned slowly on low wind days to check structural measurement signals. Some of the accelerometer cables had been inadvertently swapped which was discovered and corrected after February 10th.

First operation with the turbine generating power was on February 21st with flap step motions to 5 degrees and then 10 degrees. Subsequent testing on February 29th revealed that the flap drive linkage mechanism had loosened on the motor shaft for a few of the flap modules. The set screws holding the control horns to the motor shafts were tightened and thread lock added.

Before each day of testing the flap motion was checked for signs of loosening in the drive mechanism and maintenance was performed as needed. For future testing efforts the mechanism would need to be redesigned to prevent loosening.

On March 9th the foil strain gage excitation voltage offsets were adjusted because the mean level had drifted to the point where signals were being clipped.

The first day of long-duration power production testing occurred on March 14th and consisted mostly of 10-minute duration data files for each static flap setting: 0 and $\pm 5, 10, 15,$ and 20 degrees.

During this time frame the programmer of the data acquisition system was addressing an issue with the fiber optic interrogator which measures the optical strain and temperature sensors. Fixes were attempted remotely but eventually the CompactRIO embedded computer system was removed, reprogrammed, and reinstalled at the beginning of April.

On April 9th, sine sweep motions were tested to excite the entire turbine system over a range of input frequencies. Unfortunately, it appears that one of the sine sweeps had demanded too much motor current and some of the lightning protection hardware became too hot and internal electrical connections failed under the stress. Identifying and fixing the issue delayed testing for about two weeks. During this time the fiber optic interrogator's peak threshold for fiber #2 was adjusted to better capture the correct wavelength peaks.

April 24th was an important day of testing because the winds were aligned with the prevailing wind direction and a full four hours of data was acquired over a range of wind speeds while using a flap "step series". The hold duration of each flap position was 30 seconds which allowed enough time for step transients to die out but was quick enough to evenly distribute the wind variation throughout the day over all the flap positions. Figure 5.3 shows the step sequence and the strain response, scaled to facilitate comparison, which correlates well with the flap motions. Similar data sets were taken on May 10th and May 23rd but the average wind direction did not match the prevailing direction.

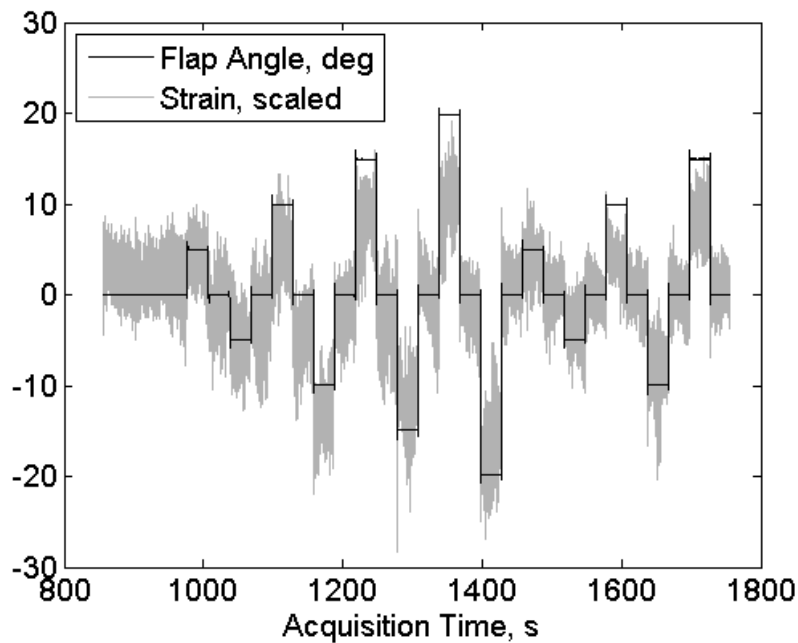


Figure 5.3 Strain response to flap step sequence.

Video of the flaps in operation was taken on May 4th, a few frames of which are shown in Figure 5.4. Flap motions included a step series, a sine series, and a sine sweep. The motions were performed first with the rotor parked and then during power production.

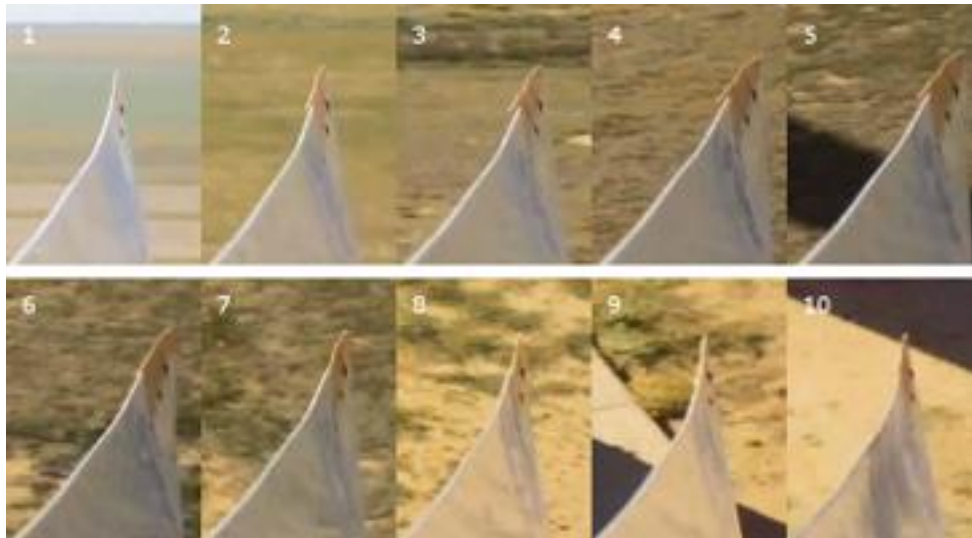


Figure 5.4 This sequence of video frames of a sinusoidal flap motion shows the blade tip moving from a downwind position (1) to an upwind position (5) and back to the downwind position (9) during one flap cycle.

Initial analysis of the power production data seemed to indicate a loss of power compared to baseline CX-100 tests. To investigate the possibility of air leakage from the high pressure to low pressure side through the flap hinge, on May 25th all seams on the flap modules were taped and about 50 minutes of power production data was obtained. The tape did not stay in place very long and so the value of the data set is questionable.

Tabular summaries of the acquired data files are available in Appendix G.

6. CONCLUSION

A wind turbine rotor with integrated trailing-edge flaps was designed and tested to demonstrate active control in the field and obtain data sets for validation of simulation tools. The design of the SMART rotor modified the DOE/SNL CX-100 research blade platform to allow installation of active aerodynamic control modules.

The structural changes to the baseline CX-100 design were focused on maintaining blade stiffness when a portion of the trailing edge was removed. Analysis to verify the required design changes was straight forward. However, integration of the trailing-edge flap modules highlighted the following design challenges:

- Variation between blade geometries was significant even though they were produced from the same blade mold.
- The method of attaching the modules to the blade impacts ease of manufacturing, alignment, and maintenance.

The main blade geometry variation which complicated flap module integration was the outboard airfoil thickness. Due to a compressed project timeline, the flap module geometry was based on measurements of a baseline CX-100 blade tip rather than the as-built SMART blades. Airfoil thickness in the outboard region of the SMART blades was smaller than that found on the CX-100 blade tip which had been used to design the modules. As a result, filler material had to be added to fill the gap and smooth the surface.

Variation also existed from one SMART blade to another. Some of the variation may have been unique to this rotor due to some unique manufacturing steps. Nonetheless, the variations raise the important issues of repeatability and ease of manufacturing when considering how integration of active aerodynamic devices would be incorporated into blade manufacturing procedures.

The method of attaching the modules to the blade was decided early in the blade design to allow sufficient time for designing the module geometry. Through the course of the blade design and build, however, additional insight was gained into trade-offs in the method of attachment:

- The socket cap screws were difficult to reach, and over the course of many removals and installations the nutplates could possibly wear out and no longer hold the fastener tightly.
- The fasteners had been placed at the centerline of the module so that the access tubes would be covered by the flap. Offsetting the fasteners would have better handled the loading but would have required filling the access tubes after installation to obtain a smooth aerodynamic surface. Ideally, a future design would better address the forces on the modules while simplifying installation and preserving aerodynamic smoothness.
- Although retrofitting the blades with flat mounting surfaces was a successful approach, future designs should consider approaches integrated with the blade manufacture and designed in conjunction with the fastener considerations given above.
- Alignment flexibility is important, especially due to the variation in blade geometry.

Rapid prototyping allowed rapid production of complicated geometry at low cost. With UV-resistant spray paint protecting the surface, the ABS plastic material survived four months in the field but was yellowed and becoming brittle by the end. A more long-term test platform would require another choice of materials or planning for periodic replacement of the modules.

During testing it was discovered that the linkage mechanism transferring motion from the drive motor to the flap was allowing relative motion under aerodynamic loading. For future testing the mechanism would need to be redesigned to reduce the amount of relative motion and, ideally, a rotation sensor would measure the flap angle to supplement the motor shaft angle measurement. Despite these challenges, all nine modules were operational during testing, achieved the desired flap deflection rate, and had an observable impact on blade strains.

Detailed analysis of the field test data is contained in a subsequent report [33].

7. REFERENCES

1. U.S. Department of Energy. "Report on the First Quadrennial Technology Review," DOE/S-0001, Washington, DC, September 2011.
2. U.S. Department of Energy. "20% Wind Energy by 2030," DOE/GO102008-2567, Washington, DC, July 2008.
3. T.K. Barlas and G.A.M. van Kuik. "Review of state of the art in smart rotor control research for wind turbines," *Progress in Aerospace Science* (2009), doi:10.1016/j.paerosci.2009.08.002
4. J-W van Wingerden, A.W. Hulskamp, T. Barlas, B. Marrant, G.A.M. van Kuik, D-P Molenaar, and M. Verhaegen, "On the Proof of Concept of a 'Smart' Wind Turbine Rotor Blade for Load Alleviation", *Wind Energy*, 2008; 11:265-80.
5. T. Barlas, J-W van Wingerden, A. Hulskamp, and G. van Kuik, "Closed-loop Control Wind Tunnel Tests on an Adaptive Wind Turbine Blade for Load Reduction," *Proceedings of the 46th AIAA/ASME*, Reno, NV, USA, 2008.
6. N. Troldborg, "Computational study of the Risø B1-18 airfoil with a hinged flap providing variable trailing edge geometry." *Wind Engineering* 2005, 29:89-113.
7. T. Buhl, M. Gaunaa, and C. Bak, "Load reduction potential using airfoils with variable trailing edge geometry," *Proceedings of the 43th AIAA/ASME*, Reno, NV, USA, 2005.
8. T. Buhl, M. Gaunaa, and C. Bak, "Potential load reduction using airfoils with variable trailing edge geometry." *Solar Energy Engineering* 2005, 127:503-16.
9. P. B. Andersen, M. Gaunaa, C. Bak, and T. Buhl, "Load alleviation on wind turbine blades using variable airfoil geometry," *Proceedings of the EWEC 2006*, Athens, Greece.
10. P. B. Andersen, M. Gaunaa, C. Bak, and T. Buhl, "Wind tunnel test on wind turbine airfoil with adaptive trailing edge geometry," *Proceedings of the 45th AIAA/ASME*, Reno, NV, USA, 2007.
11. T. Buhl, "Stability Limits for a Full Wind Turbine Equipped with Trailing Edge Systems," *European Wind Energy Conference*, Marseille, France, 16-19 March, 2009.
12. P.B. Anderson, "Load Reduction Using Pressure Difference on Airfoil for Control of Trailing Edge Flaps," *European Wind Energy Conference*, Marseille, France, 16-19 March, 2009.
13. D.G. Wilson, D.E. Berg, M.F. Barone, J.C. Berg, B.R. Resor, and D.W. Lobitz, "Active Aerodynamic Blade Control Design for Load Reduction on Large Wind Turbines," *European Wind Energy Conference*, Marseille, France, 26-19 March, 2009.

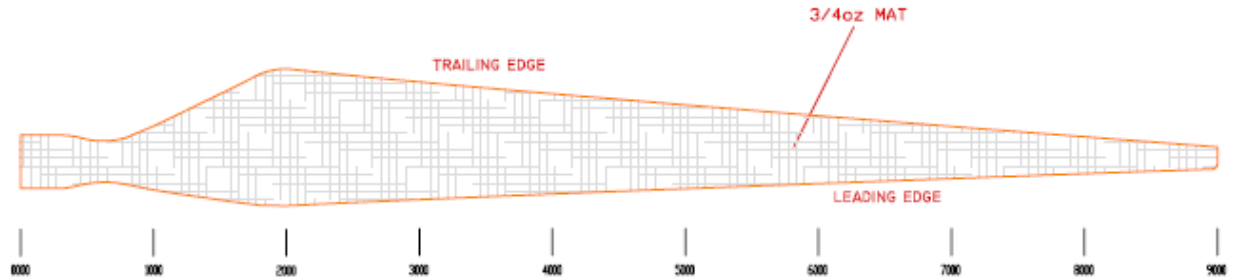
14. D.E. Berg, D.G. Wilson, M.F. Barone, J.C. Berg, B.R. Resor, J.A. Paquette, and J.R. Zayas, "The Impact of Active Aerodynamic Load Control on Fatigue and Energy Capture at Low Wind Speed Sites," European Wind Energy Conference, Marseille, France, 16-19 March, 2009.
15. D.E. Berg, D.G. Wilson, B.R. Resor, M.F. Barone, J.C. Berg, S. Kota, and G. Ervin, "Active Aerodynamic Blade Load Control Impacts on Utility-Scale Wind Turbines," WINDPOWER 2009, Chicago, Illinois, 5-7 May, 2009.
16. D.G. Wilson, D.E. Berg, B.R. Resor, M.F. Barone, and J.C. Berg, "Combined Individual Pitch Control and Active Aerodynamic Load Controller Investigation for the 5MW UpWind Turbine", WINDPOWER 2009, Chicago, Illinois, 5-7 May, 2009.
17. B. Resor, D. Wilson, D. Berg, J. Berg, T. Barlas, and G. van Kuik, "The Impact of Higher Fidelity Models on Active Aerodynamic Load Control Fatigue Damage Reduction," Proceedings of the 48th AIAA Aerospace Sciences Meeting, Orlando, FL, January 4-7, 2010.
18. D.G. Wilson, B.R. Resor, D.E. Berg, T.K. Barlas, and G.A.M. van Kuik, "Active Aerodynamic Blade Distributed Flap Control Design Procedure for Load Reduction on the UpWind 5MW Wind Turbine," Proceedings of the 48th AIAA Aerospace Sciences Meeting, Orlando, FL, January 4-7, 2010.
19. D.E. Berg, D. Wilson, B. Resor, J. Berg, T. Barlas, A. Crowther, and C. Halse, "System ID Modern Control Algorithms for Active Aerodynamic Load Control and Impact on Gearbox Loading," The Science of Making Torque from Wind, 2010.
20. R. Chow and C.P. van Dam, "Unsteady Computational Investigations of Deploying Load Control Microtabs," Journal of Aircraft, Vol. 43, No. 5, Sept-Oct 2006, pp. 1458-1469.
21. D.E. Berg, J.R. Zayas, D.W. Lobitz, C.P. van Dam, R. Chow, and J.P. Baker, "Active Aerodynamic Load Control of Wind Turbine Blades," Proceedings of the 5th Joint ASME/JSME Fluids Engineering Conference, San Diego, CA, June 2007.
22. J.R. Zayas, P.L. Jones, and A. Holman, "CX-100 and TX-100 Blade Field Tests." SAND2005-7454, Sandia National Laboratories, Albuquerque, NM.
23. J. Paquette, J. van Dam, S. Hughes, "Fatigue Testing of 9m Carbon Fiber Wind Turbine Research Blades," Proceedings of the 46th AIAA Aerospace Sciences Meeting, Reno, NV, January 2008.
24. J. Paquette, D.L. Laird, D.T. Griffith, L. Rip, "Modeling and Testing of 9m Research Blades," Proceedings of the 44th AIAA Aerospace Sciences Meeting, Reno, NV, January 2006.
25. J. White, "Operational Monitoring of Horizontal Axis Wind Turbines with Inertial Measurements." Ph.D. Dissertation, Purdue University, West Lafayette, IN., 2010.

26. J. White, D. Adams, and M. Rumsey, "Measurement of Operational Loading and Deflection with a Smart Turbine Rotor Blade," WINDPOWER 2009, Chicago, IL, May 4-7, 2009.
27. D. Berry and T. Ashwill, "Design of 9-Meter Carbon-Fiberglass Prototype Blades: CX-100 and TX-100." SAND2007-0201, Sandia National Laboratories, Albuquerque, NM.
28. NWTC Design Codes (PreComp by Gunjit Bir).
<http://wind.nrel.gov/designcodes/preprocessors/precomp/>. Last modified 26-March-2007; accessed March 2010.
29. Sandia National Laboratories: Numerical Manufacturing And Design Tool (NuMAD© version 2.0). http://energy.sandia.gov/?page_id=2238. Pre-release internal development version April 2010.
30. NWTC Computer-Aided Engineering Tools (FAST by Jason Jonkman, Ph.D.).
<http://wind.nrel.gov/designcodes/simulators/fast/>. Last modified 31-Mar-2010; accessed 31-Mar-2010.
31. XFOIL 6.97 by Mark Drela and Harold Youngren. MIT Aero & Astro / Aircraft, Inc.
<http://web.mit.edu/drela/Public/web/xfoil/>
32. Triboelectric Effect: http://en.wikipedia.org/wiki/Triboelectric_effect
33. J. Berg, M. Barone, and N. Yoder, "SMART Wind Turbine Rotor: Data Analysis and Conclusions." SAND2014-0712, Sandia National Laboratories, Albuquerque, NM.

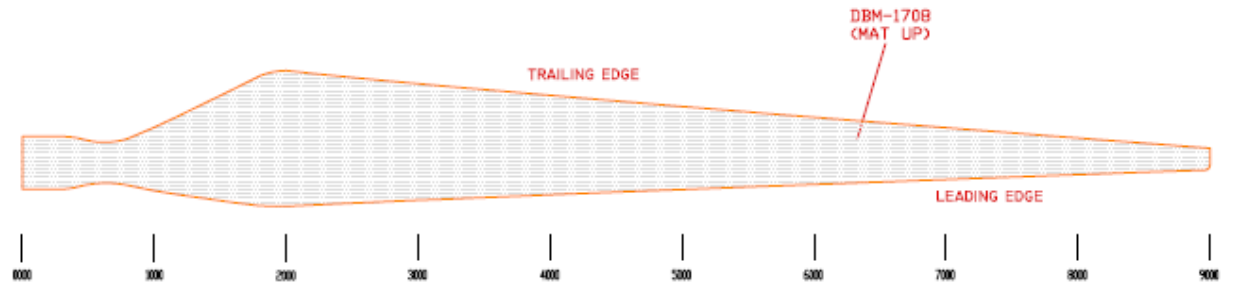
APPENDIX A: ORIGINAL CX LAYUP

Following are illustrations of the original CX-100 layup design. This is provided as a reference and a starting point from which to understand the modifications to this design for the SMART blade.

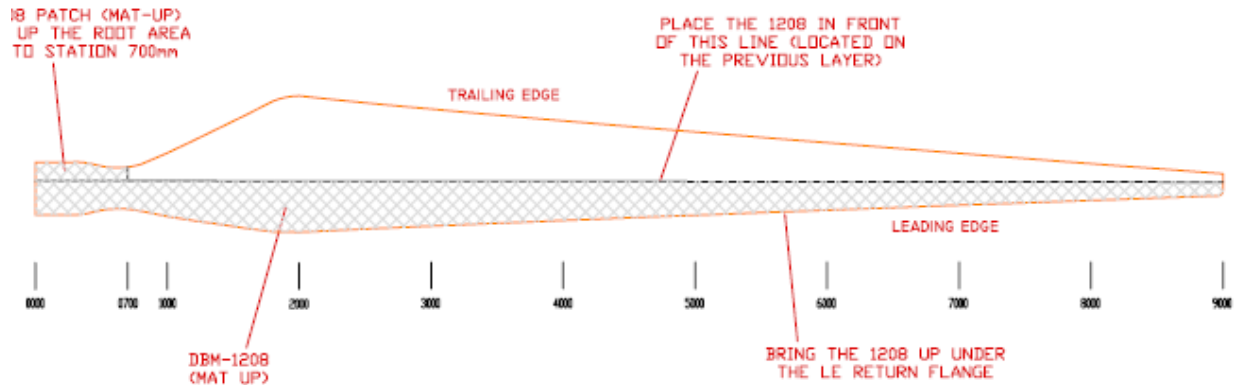
Low Pressure Skin



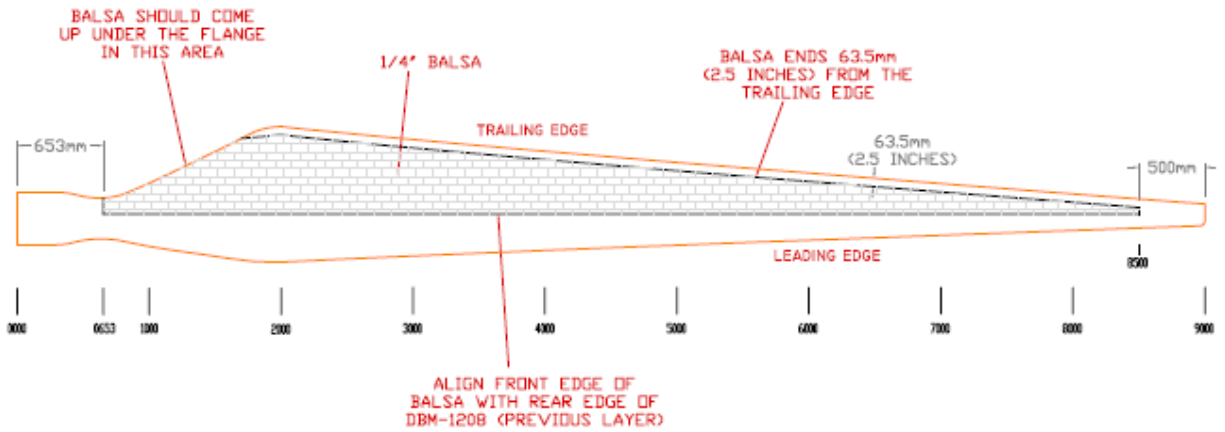
(A)



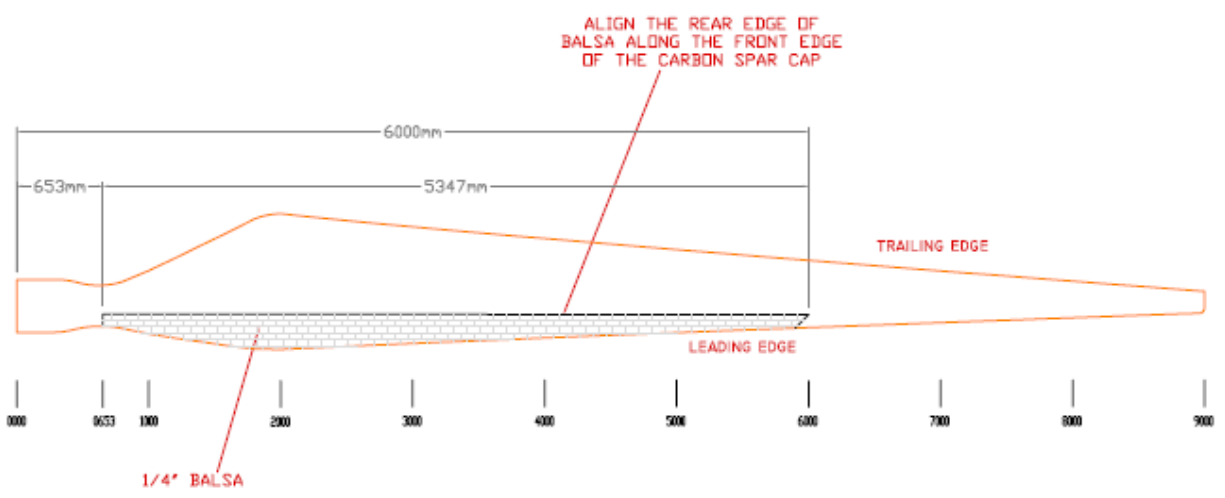
(B)



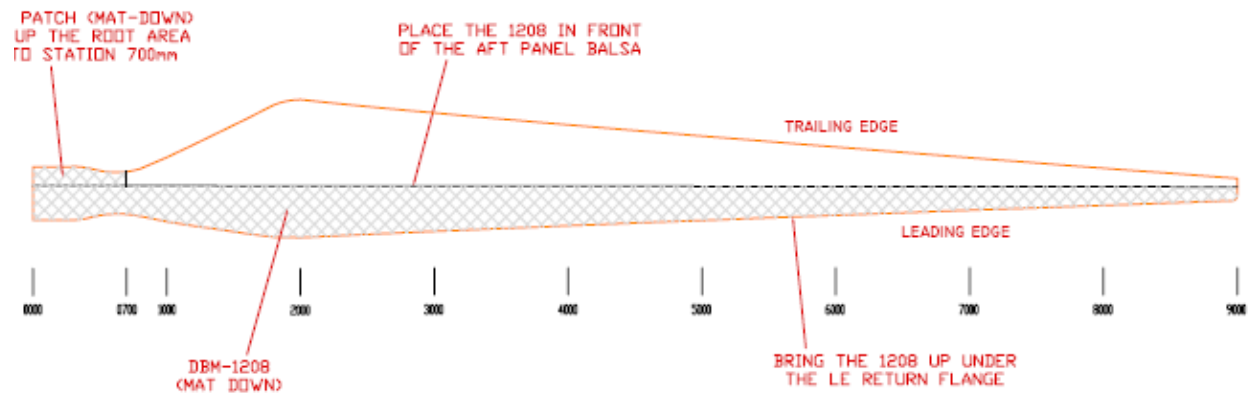
(C)



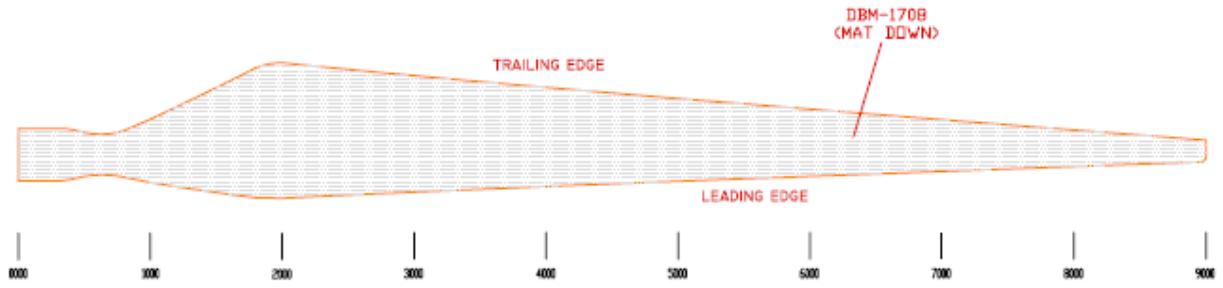
(D)



(E)

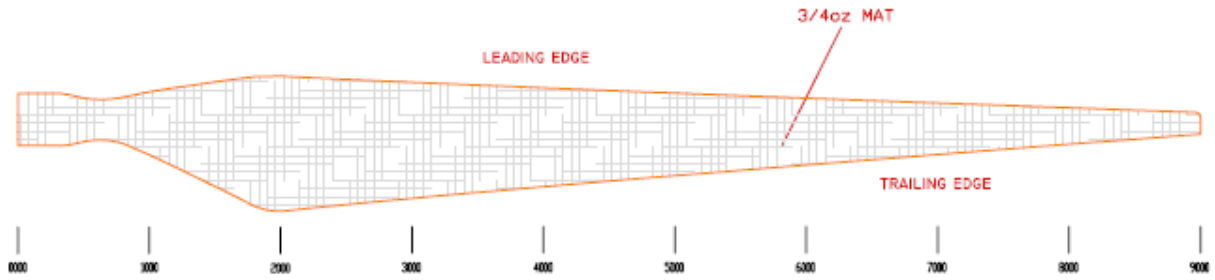


(F)

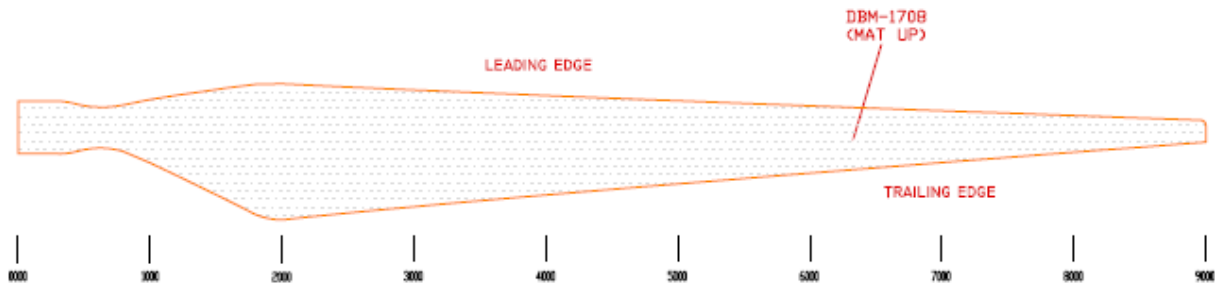


(G)

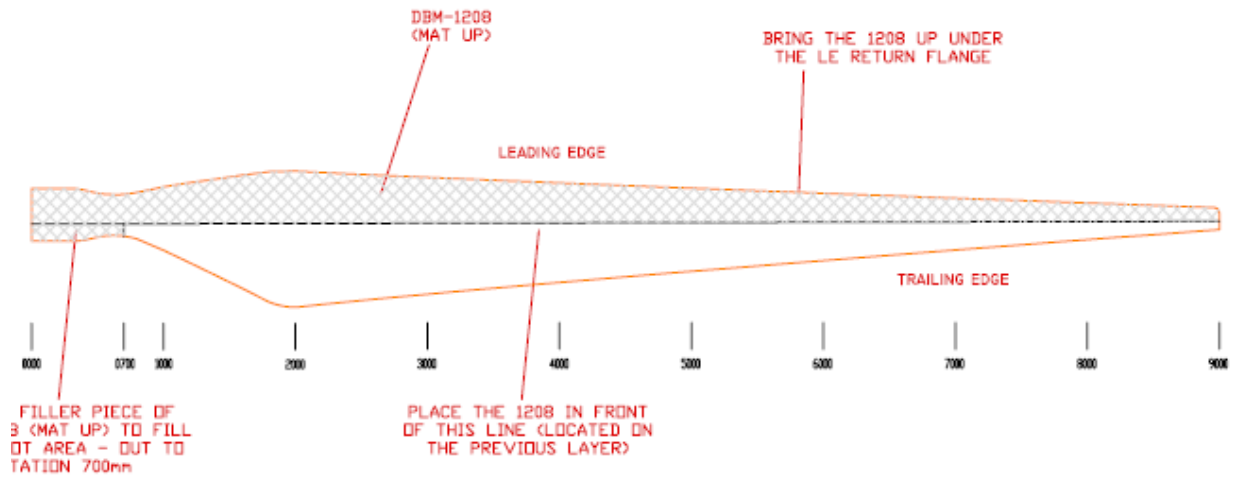
High Pressure Skin



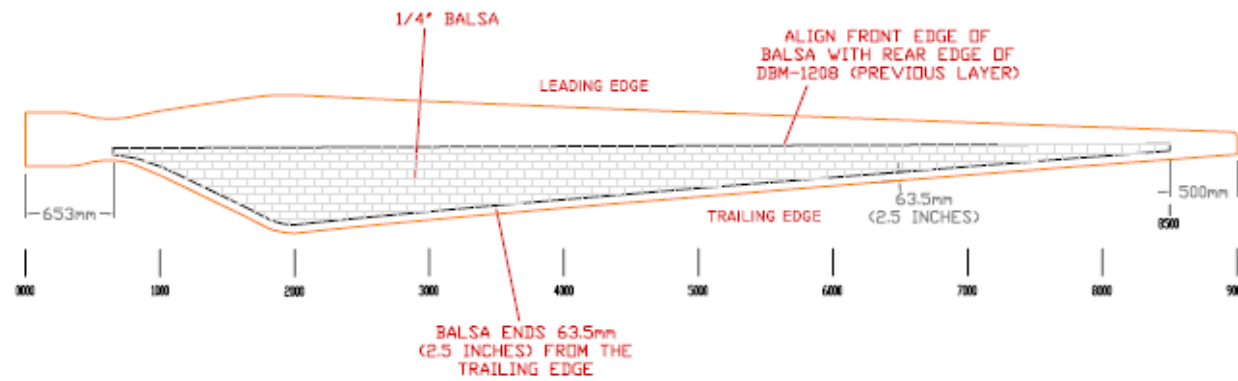
(A)



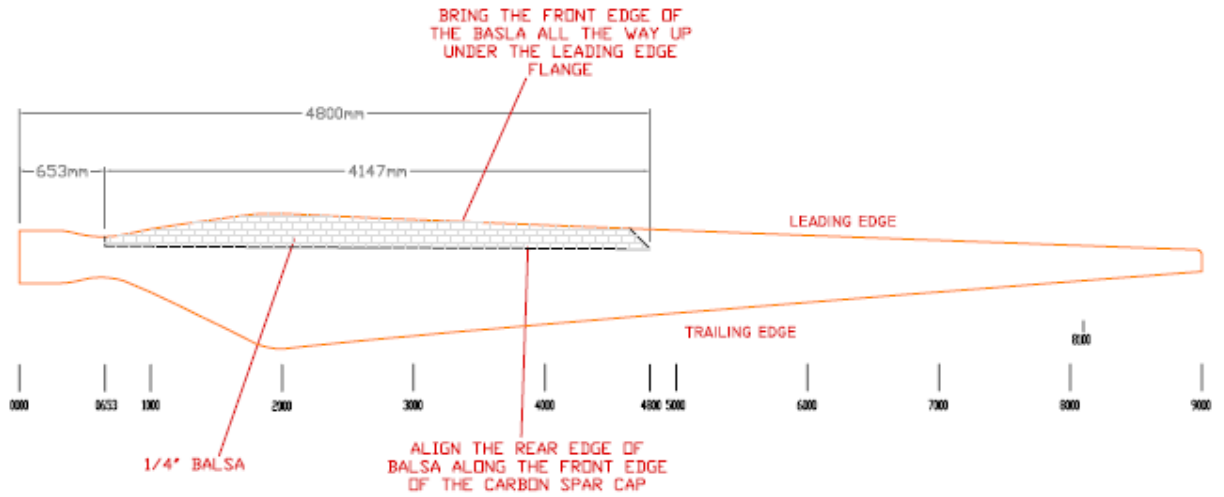
(B)



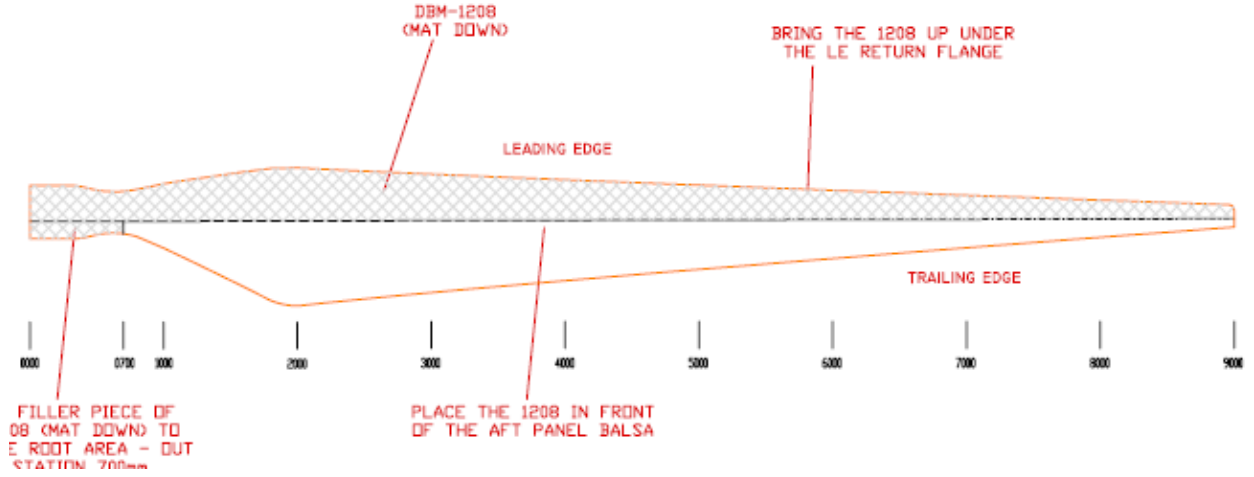
(C)



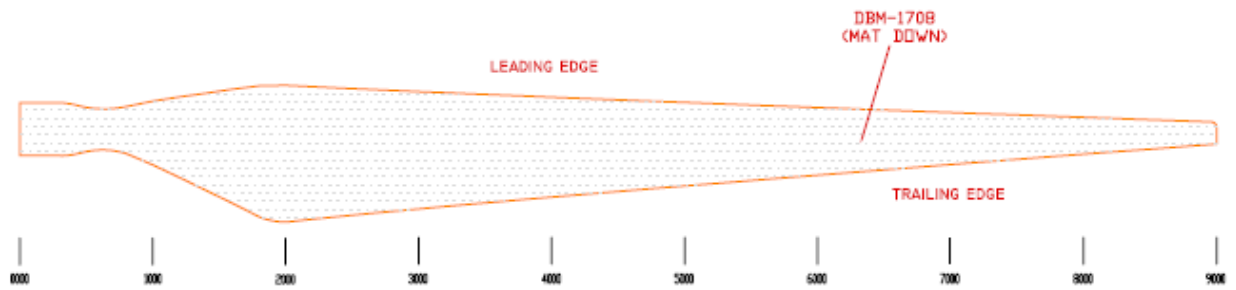
(D)



(E)



(F)



(G)

APPENDIX B: CHANGES TO PRECOMP V1.00.02

PreComp version 1.00.02 had known calculation errors. Through testing it was determined that the errors were most obvious when shear webs were included. Basically, the shear web elements appeared to be adding area moment of inertia as if they were rotated 90 degrees. Two errors were found in the source code which are documented below. PreComp version 1.00.03 incorporates these changes.

30-Mar-2010 shear web bugs: section centers and area moments of inertia

=====
Line 1196 -- Finding the center of a shear web segment lamina stack

original: $y_0 = y_0 - tbar/2. - y_sc$

modified: $y_0 = ysg - tbar/2. - y_sc$

additional note: Need to understand why tbar is divided by 2

Lines 1212-1213 -- this change seems to fix the problems caused by shear webs, need to verify with code authors

original: $ipp = iepz - iemz*c2ths$! check this block later

$iqq = iepz + iemz*c2ths$

modified: $ipp = iepz + iemz*c2ths$! check this block later

$iqq = iepz - iemz*c2ths$

additional note: Does line 1214 also need a sign change?

How are ipp, iqq, and ipq defined for a segment?

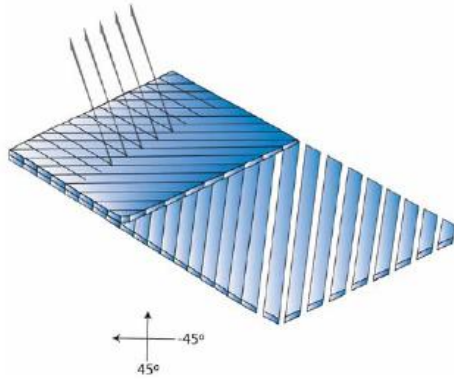
Line 1719 -- calculating the orientation of a segment

original: $yba = ya - yb$

note: should this be $yb - ya$? In which direction is thseg intended to be positive?

APPENDIX C: VECTORPLY DATA SHEET

(2 pages)



C-BX 1200

Fiber Type: Carbon
 Architecture: +45°/-45° Double Bias
 Dry Thickness: 0.024 in. / 0.61 mm
 Total Weight: 11.56 oz/sq.yd / 392 g/sq.m

VECTORULTRA™



Roll Specifications			Fiber Architecture Data	
Roll Width:	Roll Weight:	Roll Length:	0 ° :	n/a
50 in / 1270 mm	113 lb / 51 kg	110 yd / 101 m	45 ° :	5.78 oz/sq.yd / 196 g/sq.m
			90 ° :	n/a
			- 45 ° :	5.78 oz/sq.yd / 196 g/sq.m
			Chopped Mat :	n/a

1: Packaging: box or bag.
 2: Weights do not include polyester stitching.

Laminated Properties

45 °

45 °

Laminate Weight (lb/sq.ft)	C-BX 1200 Resin Infused	C-BX 1200 Open Mold
Fiber	0.08	0.08
Resin	0.04	0.10
Total	0.12	0.18

Physical Properties

C-BX 1200 Resin Infused

C-BX 1200 Open Mold

Density (g/cc)	1.53	1.41
Fiber Content (% by Wt.)	65%	45%
Thickness (in)	0.016	0.024

Laminate Moduli		
(MSI)	C-BX 1200 Resin Infused	C-BX 1200 Open Mold
Ex	8.53	5.69
Ey	8.53	5.69
Gxy	0.37	0.25
Ex,flex.	8.10	5.40
Ey,flex.	8.10	5.40

Ultimate Stress		
(KSI)	C-BX 1200 Resin Infused	C-BX 1200 Open Mold
Long. Ten.	81	54
Long. Comp.	74	50
Trans. Ten.	81	54
Trans. Comp.	74	50
In-Plane Shear	7	5
Long. Flex.	83	55
Trans. Flex.	83	55

In-Plane Stiffness, "EA"		
10 ³ lb/in	C-BX 1200 Resin Infused	C-BX 1200 Open Mold
(EA)x	133	138
(EA)y	133	138
(GA)xy	6	6

Ultimate In-Plane Load		
lb/in	C-BX 1200 Resin Infused	C-BX 1200 Open Mold
Long. Ten.	1,254	1,307
Long. Comp.	1,159	1,208
Trans. Ten.	1,254	1,307
Trans. Comp.	1,159	1,208
In-Plane Shear	116	120

Notes:

- 1: Resin infused laminate made with vinyl ester resin 200 cps viscosity @ 77° F.
- 2: Open mold laminate made with polyester resin.
- 3: All standard reinforcements should be infused with a flow aid or Vectorfusion® reinforcements.



3500 Lakewood Dr. Phenix City, AL 36867 tel. 334 291 7704 fax. 334 291 7743

Disclaimer:

As a service to customers, Vectorply Corporation ("VP") may provide computer-generated predictions of the physical performance of a product using a reinforcement fabric produced by VP in combination with other materials or systems.

VP makes no warranty whatsoever as to the accuracy of any such predicted physical performance, and customer acknowledges that customer is solely responsible for determining the performance and fitness for a particular use of any product produced by customer utilizing a fabric or material produced or manufactured by VP. Specifications of reinforcements may change without notice.

APPENDIX D: PRECOMP SECTION ANALYSIS INPUTS

Material Properties

Input file

Mat_Id	E1	E2	G12	Nu12	Density	Mat_Name
(-)	(Pa)	(Pa)	(Pa)	(-)	(Kg/m ³)	(-)
1	3.44e+009	3.4400e+009	1.3231e+009	0.300000	1230	(gel_coat)
3	1.2e+008	1.2000e+008	2.0000e+007	0.300000	230	(Balsa)
5	7.58e+009	7.5800e+009	4.0000e+009	0.300000	1687	(Mat_NPS)
6	9.58e+009	9.5800e+009	6.8900e+009	0.390000	1814	(DBM1708_NPS)
8	8.41e+010	8.7600e+009	4.3800e+009	0.250000	3469	(CX100_hybrid_triax)
10	1.2e+008	1.2000e+008	2.0000e+007	0.300000	230	(Balsa_NPS)
12	5.8812e+010	5.8812e+010	2.5511e+009	0.32	1530	(VectorPly_CBX1200)

Webs:

Main shear web

web_num no of laminae (N_weblams)
1 3

lamina number	num plies	thickness of ply (m)	fibers_direction (deg)	composite_material ID (-)
wlam_num	N_plies	w_tply	Tht_Wlam	Wmat_id
1	1	0.0015	0	4 (DBM1708)
2	1	0.0095	0	3 (Balsa)
3	1	0.0015	0	4 (DBM1708)

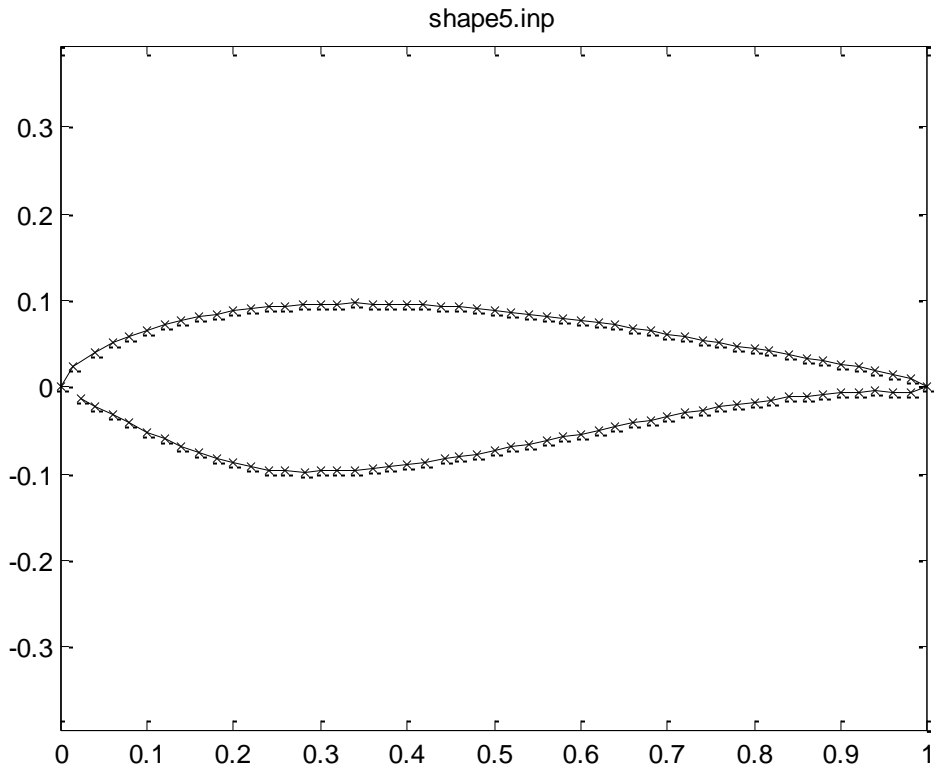
Aft flange

web_num no of laminae (N_weblams)
2 3

lamina number	num plies	thickness of ply (m)	fibers_direction (deg)	composite_material ID (-)
wlam_num	N_plies	w_tply	Tht_Wlam	Wmat_id
1	2	0.0004064	0	12 (VectorPly_CBX1200)
2	1	0.0095	0	3 (Balsa)
3	2	0.0004064	0	12 (VectorPly_CBX1200)

Station 5

This is the last station with full chord, i.e. no cut-off trailing edge.



Overall

Blade-sections-specific data -----

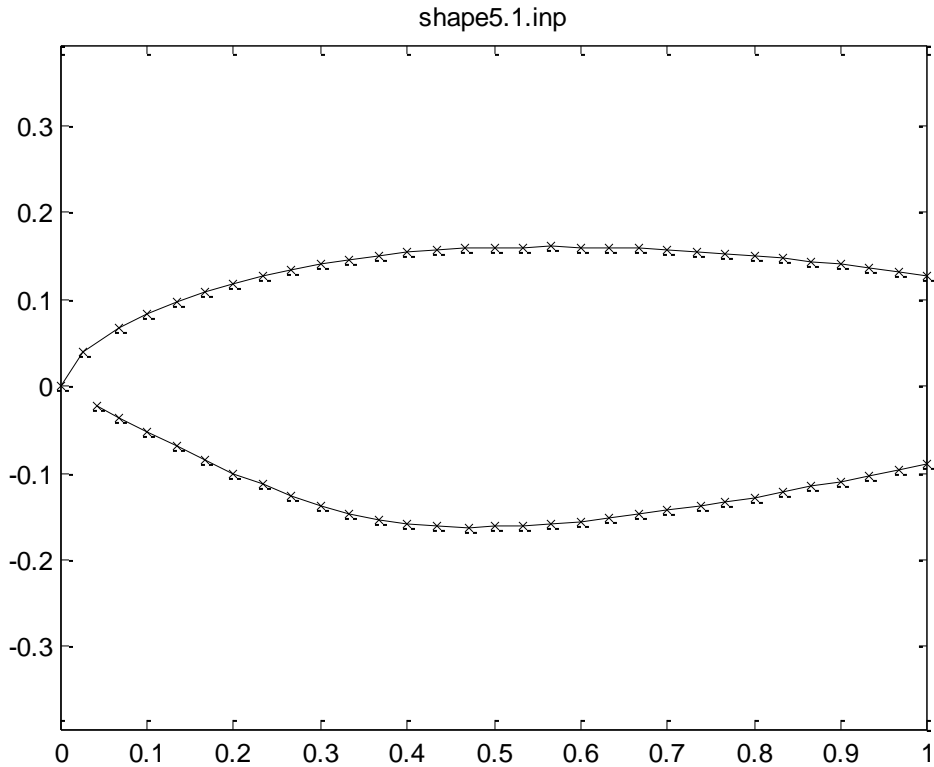
Sec span	l.e.	chord	aerodynamic	af_shape	int str	layup
location	position	length	twist	file	file	
Span_loc	Le_loc	Chord	Tw_aero	Af_shape_file	Int_str_file	
(-)	(-)	(m)	(degrees)	(-)	(-)	

0.000000	0.320000	0.346000	1.400000	'shape5.inp'	'layup5.inp'
1.000000	0.320000	0.346000	1.400000	'shape5.inp'	'layup5.inp'

Layup (webs present but not shown here)

Not included here.

Station 5.1 (cutout)



Overall

Blade-sections-specific data -----

Sec span	location	position	length	twist	af_shape	int	str	layup
Span_loc	Le_loc	Chord	Tw_aero	Af_shape_file	Int_str_file			
(-)	(-)	(m)	(degrees)	(-)	(-)			

0.000000	0.533333	0.207600	1.400000	'shape5.1.inp'	'layup5.1.inp'			
1.000000	0.533333	0.207600	1.400000	'shape5.1.inp'	'layup5.1.inp'			

Webs (spars) data -----

2	Nweb	: number of webs (-) ! enter 0 if the blade has no webs
1	lb_sp_stn	: blade station number where inner-most end of webs is located (-)
2	Ob_sp_stn	: blade station number where outer-most end of webs is located (-)

Web_num	Inb_end_ch_loc	Oub_end_ch_loc	(fraction of chord length)
1	0.71	0.71	
2	1.0	1.0	

Layup (webs present but not shown here)
 Composite laminae lay-up inside the blade section

***** TOP SURFACE *****

4 N_scts(1): no of sectors on top surface

normalized chord location of nodes defining airfoil sectors boundaries (xsec_node)

0.0 0.518 0.705 0.766 1.0

.....

Sect_num no of laminae (N_laminas)

1 5

lamina num of thickness fibers_direction composite_material ID

number plies of ply (m) (deg) (-)

lam_num N_plies Tply Tht_lam Mat_id

1	1	0.0001	0	1	(gel_coat)
2	1	0.0004	0	5	(Mat_NPS)
3	2	0.0004064	0	12	(VectorPly_CBX1200)
4	1	0.00056	0	6	(DBM1708_NPS)
5	1	0.0014	0	6	(DBM1708_NPS)

.....

Sect_num no of laminae (N_laminas)

2 6

lamina num of thickness fibers_direction composite_material ID

number plies of ply (m) (deg) (-)

lam_num N_plies Tply Tht_lam Mat_id

1	1	0.0001	0	1	(gel_coat)
2	1	0.0004	0	5	(Mat_NPS)
3	2	0.0004064	0	12	(VectorPly_CBX1200)
4	1	0.00056	0	6	(DBM1708_NPS)
5	1	0.0033	0	8	(CX100_hybrid_triax)
6	1	0.0014	0	6	(DBM1708_NPS)

.....

Sect_num no of laminae (N_laminas)

3 6

lamina num of thickness fibers_direction composite_material ID

number plies of ply (m) (deg) (-)

lam_num N_plies Tply Tht_lam Mat_id

1	1	0.0001	0	1	(gel_coat)
2	1	0.0004	0	5	(Mat_NPS)
3	2	0.0004064	0	12	(VectorPly_CBX1200)
4	1	0.00056	0	6	(DBM1708_NPS)
5	1	0.0033	0	8	(CX100_hybrid_triax)
6	1	0.0014	0	6	(DBM1708_NPS)

.....

Sect_num no of laminae (N_laminas)

4 4

lamina num of thickness fibers_direction composite_material ID

number plies of ply (m) (deg) (-)

lam_num	N_plies	Tply	Tht_lam	Mat_id
1	1	0.0001	0	1 (gel_coat)
2	1	0.0004	0	5 (Mat_NPS)
3	2	0.0004064	0	12 (VectorPly_CBX1200)
4	1	0.0009	0	6 (DBM1708_NPS)

***** BOTTOM SURFACE *****

3 N_scts(2): no of sectors on bottom surfaces

normalized chord location of surface nodes defining sector boundaries (xsec_node)

0.0 0.472 0.716 1.0

.....

Sect_num no of laminae (N_laminas)

1 5

lamina num of thickness fibers_direction composite_material ID
number plies of ply (m) (deg) (-)

lam_num	N_plies	Tply	Tht_lam	Mat_id
1	1	0.0001	0	1 (gel_coat)
2	1	0.0004	0	5 (Mat_NPS)
3	2	0.0004064	0	12 (VectorPly_CBX1200)
4	1	0.00056	0	6 (DBM1708_NPS)
5	1	0.0014	0	6 (DBM1708_NPS)

.....

Sect_num no of laminae (N_laminas)

2 6

lamina num of thickness fibers_direction composite_material ID
number plies of ply (m) (deg) (-)

lam_num	N_plies	Tply	Tht_lam	Mat_id
1	1	0.0001	0	1 (gel_coat)
2	1	0.0004	0	5 (Mat_NPS)
3	2	0.0004064	0	12 (VectorPly_CBX1200)
4	1	0.00056	0	6 (DBM1708_NPS)
5	1	0.0033	0	8 (CX100_hybrid_triax)
6	1	0.0014	0	6 (DBM1708_NPS)

.....

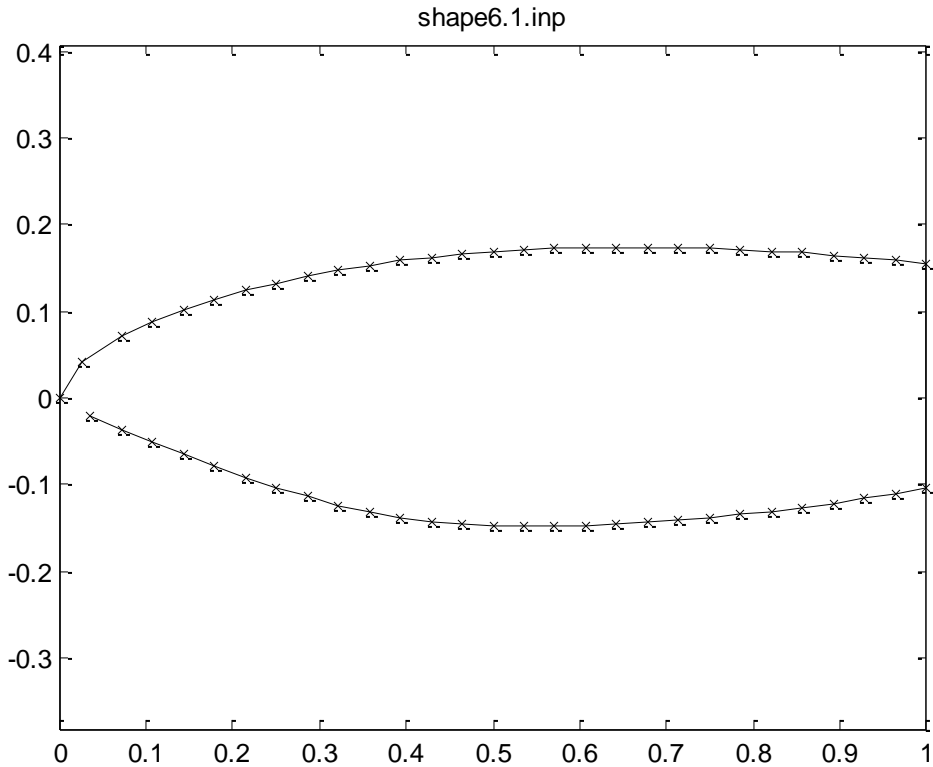
Sect_num no of laminae (N_laminas)

3 4

lamina num of thickness fibers_direction composite_material ID
number plies of ply (m) (deg) (-)

lam_num	N_plies	Tply	Tht_lam	Mat_id
1	1	0.0001	0	1 (gel_coat)
2	1	0.0004	0	5 (Mat_NPS)
3	2	0.0004064	0	12 (VectorPly_CBX1200)
4	1	0.0009	0	6 (DBM1708_NPS)

Station 6.1 (cutout)



Overall

Blade-sections-specific data -----

Sec span location	I.e. position	chord length	aerodynamic twist	af_shape file	int str file	layup
Span_loc (-)	Le_loc (-)	Chord (m)	Tw_aero (degrees)	Af_shape_file (-)	Int_str_file (-)	
0.000000	0.5714	0.14896	0.700000	'shape6.1.inp'	'layup6.1.inp'	
1.000000	0.5714	0.14896	0.700000	'shape6.1.inp'	'layup6.1.inp'	

Webs (spars) data -----

2 Nweb : number of webs (-) ! enter 0 if the blade has no webs
 1 lb_sp_stn : blade station number where inner-most end of webs is located (-)
 2 Ob_sp_stn : blade station number where outer-most end of webs is located (-)

Web_num	Inb_end_ch_loc	Oub_end_ch_loc	(fraction of chord length)
1	0.8	0.8	
2	1.0	1.0	

Layup (webs present but not shown here)
 Composite laminae lay-up inside the blade section

***** TOP SURFACE *****

3 N_scts(1): no of sectors on top surface

normalized chord location of nodes defining airfoil sectors boundaries (xsec_node)

0.0 0.585 0.792 1.0

.....

Sect_num no of laminae (N_laminas)

1 5

lamina num of thickness fibers_direction composite_material ID

number plies of ply (m) (deg) (-)

lam_num N_plies Tply Tht_lam Mat_id

1	1	0.0001	0	1	(gel_coat)
2	1	0.0004	0	5	(Mat_NPS)
3	2	0.0004064	0	12	(VectorPly_CBX1200)
4	1	0.00056	0	6	(DBM1708_NPS)
5	1	0.0014	0	6	(DBM1708_NPS)

.....

Sect_num no of laminae (N_laminas)

2 6

lamina num of thickness fibers_direction composite_material ID

number plies of ply (m) (deg) (-)

lam_num N_plies Tply Tht_lam Mat_id

1	1	0.0001	0	1	(gel_coat)
2	1	0.0004	0	5	(Mat_NPS)
3	2	0.0004064	0	12	(VectorPly_CBX1200)
4	1	0.00056	0	6	(DBM1708_NPS)
5	1	0.0033	0	8	(CX100_hybrid_triax)
6	1	0.0014	0	6	(DBM1708_NPS)

.....

Sect_num no of laminae (N_laminas)

3 4

lamina num of thickness fibers_direction composite_material ID

number plies of ply (m) (deg) (-)

lam_num N_plies Tply Tht_lam Mat_id

1	1	0.0001	0	1	(gel_coat)
2	1	0.0004	0	5	(Mat_NPS)
3	2	0.0004064	0	12	(VectorPly_CBX1200)
4	1	0.0009	0	6	(DBM1708_NPS)

***** BOTTOM SURFACE *****

3 N_scts(2): no of sectors on bottom surfaces

normalized chord location of surface nodes defining sector boundaries (xsec_node)

0.0 0.624 0.833 1.0

.....
Sect_num no of laminae (N_laminas)

1 5

lamina number	num of plies	thickness of ply (m)	fibers_direction (deg)	composite_material ID (-)
lam_num	N_plies	Tply	Tht_lam	Mat_id
1	1	0.0001	0	1 (gel_coat)
2	1	0.0004	0	5 (Mat_NPS)
3	2	0.0004064	0	12 (VectorPly_CBX1200)
4	1	0.00056	0	6 (DBM1708_NPS)
5	1	0.0014	0	6 (DBM1708_NPS)

.....
Sect_num no of laminae (N_laminas)

2 6

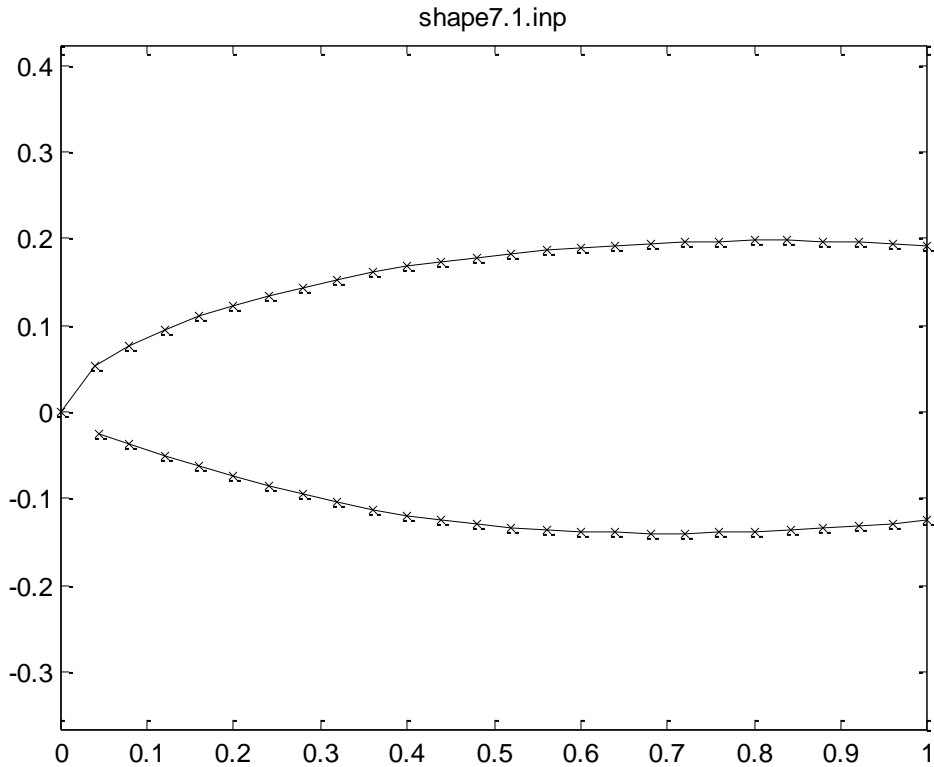
lamina number	num of plies	thickness of ply (m)	fibers_direction (deg)	composite_material ID (-)
lam_num	N_plies	Tply	Tht_lam	Mat_id
1	1	0.0001	0	1 (gel_coat)
2	1	0.0004	0	5 (Mat_NPS)
3	2	0.0004064	0	12 (VectorPly_CBX1200)
4	1	0.00056	0	6 (DBM1708_NPS)
5	1	0.0033	0	8 (CX100_hybrid_triax)
6	1	0.0014	0	6 (DBM1708_NPS)

.....
Sect_num no of laminae (N_laminas)

3 4

lamina number	num of plies	thickness of ply (m)	fibers_direction (deg)	composite_material ID (-)
lam_num	N_plies	Tply	Tht_lam	Mat_id
1	1	0.0001	0	1 (gel_coat)
2	1	0.0004	0	5 (Mat_NPS)
3	2	0.0004064	0	12 (VectorPly_CBX1200)
4	1	0.0009	0	6 (DBM1708_NPS)

Station 7.1 (cutout)



Overall

Blade-sections-specific data -----

Sec span location	i.e. position	chord length	aerodynamic twist	af_shape file	int str file	layup file
Span_loc (-)	Le_loc (-)	Chord (m)	Tw_aero (-)	Af_shape_file (-)	Int_str_file (-)	
0.000000	0.640000	0.09500	0.250000	'shape7.1.inp'	'layup7.1.inp'	
1.000000	0.640000	0.09500	0.250000	'shape7.1.inp'	'layup7.1.inp'	

Webs (spars) data -----

1 Nweb : number of webs (-) ! enter 0 if the blade has no webs
 1 lb_sp_stn : blade station number where inner-most end of webs is located (-)
 2 Ob_sp_stn : blade station number where outer-most end of webs is located (-)

Web_num Inb_end_ch_loc Oub_end_ch_loc (fraction of chord length)
 1 1.0 1.0

Layup (web present but not shown here)
 Composite laminae lay-up inside the blade section

***** TOP SURFACE *****

3 N_scts(1): no of sectors on top surface

normalized chord location of nodes defining airfoil sectors boundaries (xsec_node)

0.0 0.74 0.884 1.0

.....

Sect_num no of laminae (N_laminas)

1 5

lamina num of thickness fibers_direction composite_material ID

number plies of ply (m) (deg) (-)

lam_num N_plies Tply Tht_lam Mat_id

1	1	0.0001	0	1	(gel_coat)
2	1	0.0004	0	5	(Mat_NPS)
3	2	0.0004064	0	12	(VectorPly_CBX1200)
4	1	0.00056	0	6	(DBM1708_NPS)
5	1	0.0014	0	6	(DBM1708_NPS)

.....

Sect_num no of laminae (N_laminas)

2 6

lamina num of thickness fibers_direction composite_material ID

number plies of ply (m) (deg) (-)

lam_num N_plies Tply Tht_lam Mat_id

1	1	0.0001	0	1	(gel_coat)
2	1	0.0004	0	5	(Mat_NPS)
3	2	0.0004064	0	12	(VectorPly_CBX1200)
4	1	0.00056	0	6	(DBM1708_NPS)
5	1	0.0033	0	8	(CX100_hybrid_triax)
6	1	0.0014	0	6	(DBM1708_NPS)

.....

Sect_num no of laminae (N_laminas)

3 4

lamina num of thickness fibers_direction composite_material ID

number plies of ply (m) (deg) (-)

lam_num N_plies Tply Tht_lam Mat_id

1	1	0.0001	0	1	(gel_coat)
2	1	0.0004	0	5	(Mat_NPS)
3	2	0.0004064	0	12	(VectorPly_CBX1200)
4	1	0.0009	0	6	(DBM1708_NPS)

***** BOTTOM SURFACE *****

3 N_scts(2): no of sectors on bottom surfaces

normalized chord location of surface nodes defining sector boundaries (xsec_node)

0.0 0.873 0.96 1.0

.....
Sect_num no of laminae (N_laminas)

1 5

lamina number	num of plies	thickness of ply (m)	fibers_direction (deg)	composite_material ID (-)
lam_num	N_plies	Tply	Tht_lam	Mat_id
1	1	0.0001	0	1 (gel_coat)
2	1	0.0004	0	5 (Mat_NPS)
3	2	0.0004064	0	12 (VectorPly_CBX1200)
4	1	0.00056	0	6 (DBM1708_NPS)
5	1	0.0014	0	6 (DBM1708_NPS)

.....
Sect_num no of laminae (N_laminas)

2 6

lamina number	num of plies	thickness of ply (m)	fibers_direction (deg)	composite_material ID (-)
lam_num	N_plies	Tply	Tht_lam	Mat_id
1	1	0.0001	0	1 (gel_coat)
2	1	0.0004	0	5 (Mat_NPS)
3	2	0.0004064	0	12 (VectorPly_CBX1200)
4	1	0.00056	0	6 (DBM1708_NPS)
5	1	0.0033	0	8 (CX100_hybrid_triax)
6	1	0.0014	0	6 (DBM1708_NPS)

.....
Sect_num no of laminae (N_laminas)

3 4

lamina number	num of plies	thickness of ply (m)	fibers_direction (deg)	composite_material ID (-)
lam_num	N_plies	Tply	Tht_lam	Mat_id
1	1	0.0001	0	1 (gel_coat)
2	1	0.0004	0	5 (Mat_NPS)
3	2	0.0004064	0	12 (VectorPly_CBX1200)
4	1	0.0009	0	6 (DBM1708_NPS)

Station 8.1

Overall

Blade-sections-specific data -----

Sec span i.e. chord aerodynamic af_shape int str layup

location position length twist file file

Span_loc Le_loc Chord Tw_aero Af_shape_file Int_str_file

(-) (-) (m) (degrees) (-) (-)

0.000000 0.640000 0.0600 0.0000 'shape7.1.inp' 'layup7.1.inp'

1.000000 0.640000 0.0600 0.0000 'shape7.1.inp' 'layup7.1.inp'

Webs (spars) data -----

1 Nweb : number of webs (-) ! enter 0 if the blade has no webs

1 lb_sp_stn : blade station number where inner-most end of webs is located (-)

2 Ob_sp_stn : blade station number where outer-most end of webs is located (-)

Web_num Inb_end_ch_loc Oub_end_ch_loc (fraction of chord length)

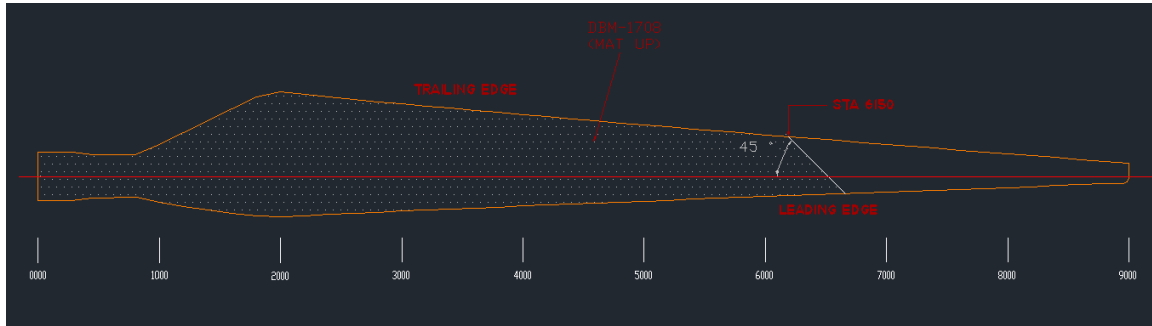
1 1.0 1.0

Layup (web present but not shown here)

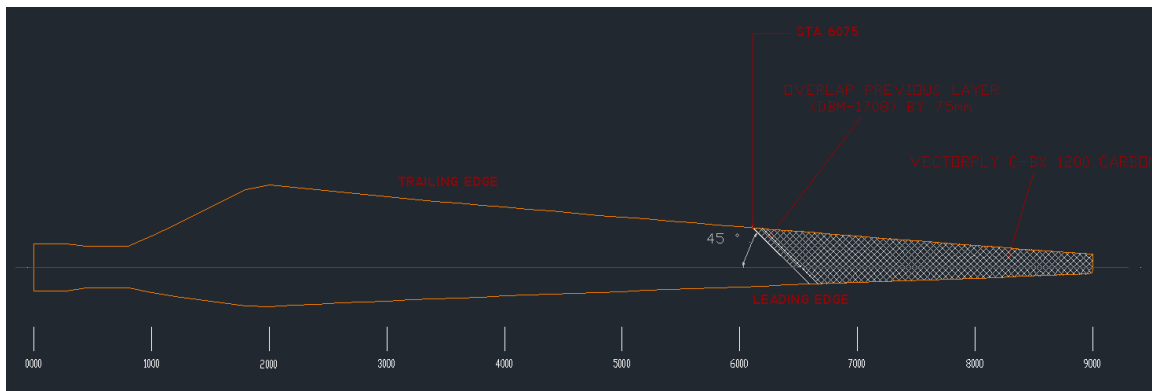
Same as Station 7.1

APPENDIX E: SMART BLADE LAYUP

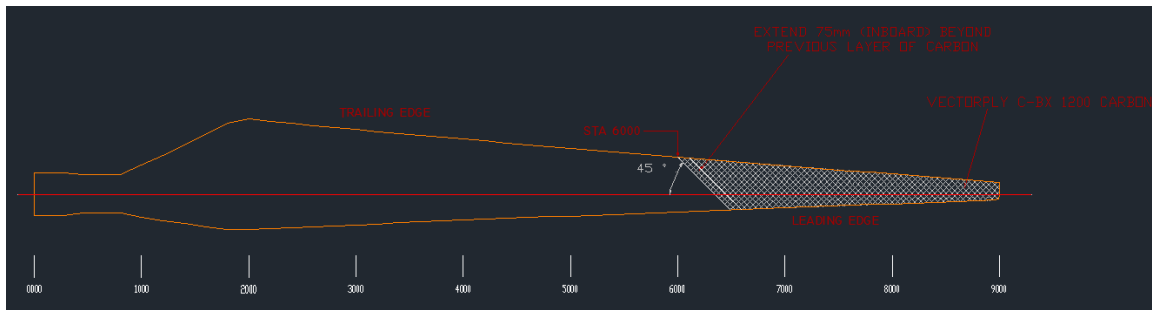
Low Pressure



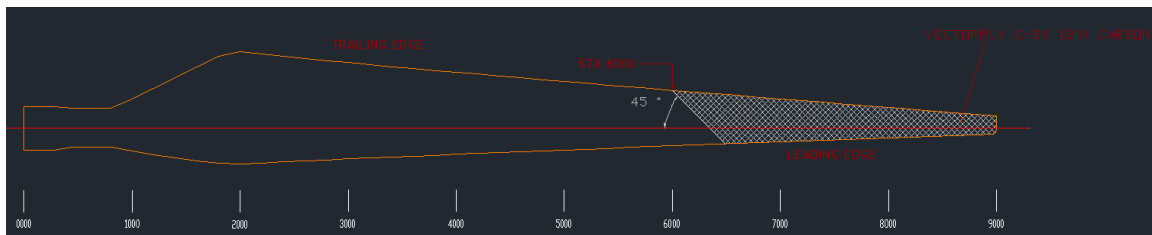
(B)



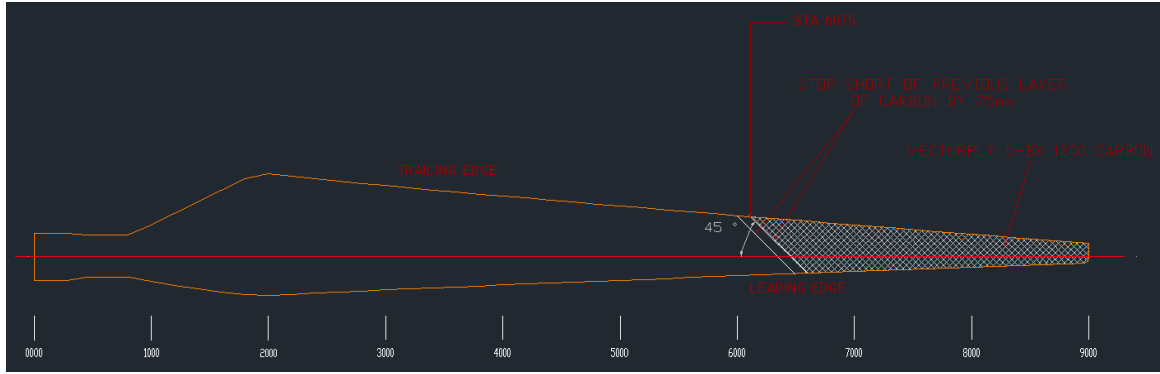
(B.1)



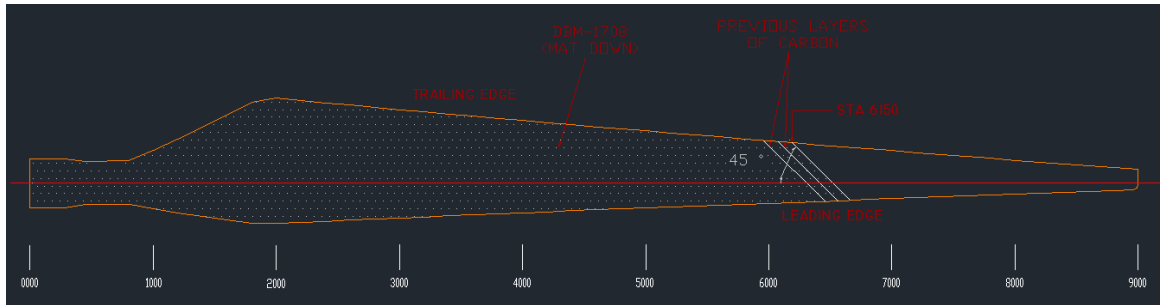
(B.2)



(F.1)

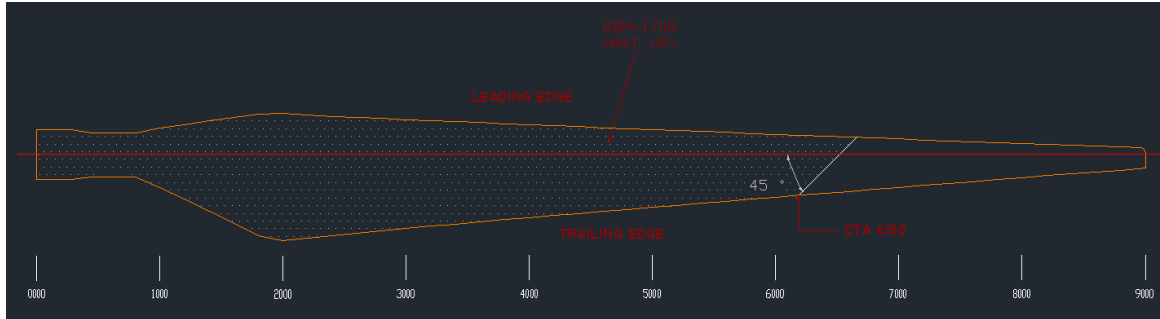


(F.2)

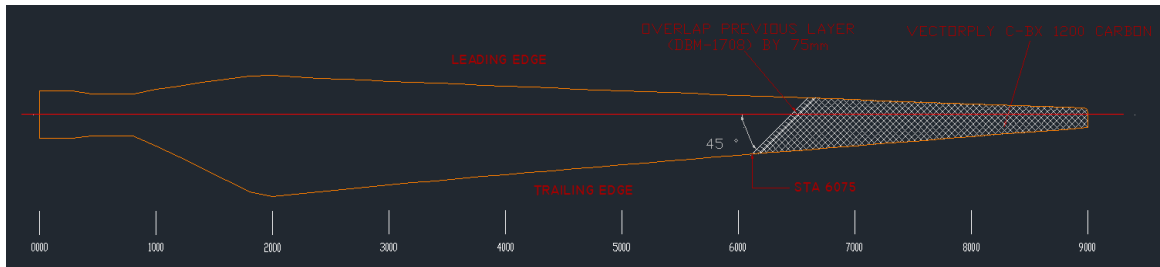


(G)

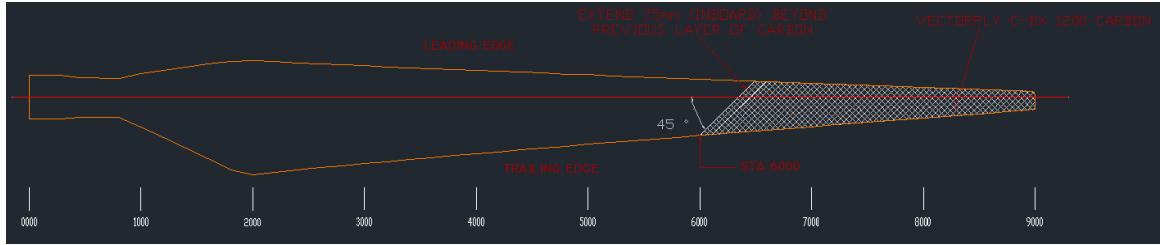
High pressure



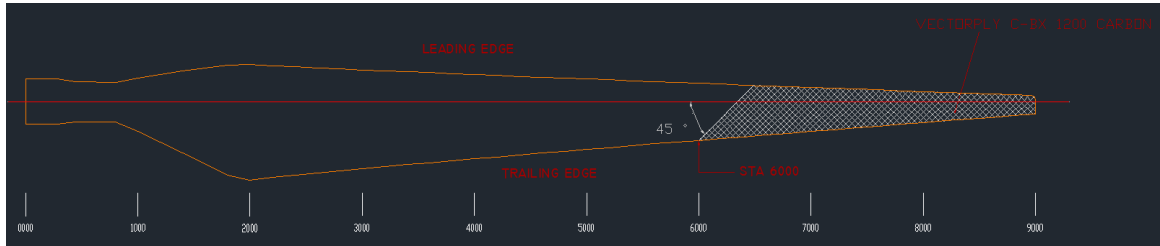
(B)



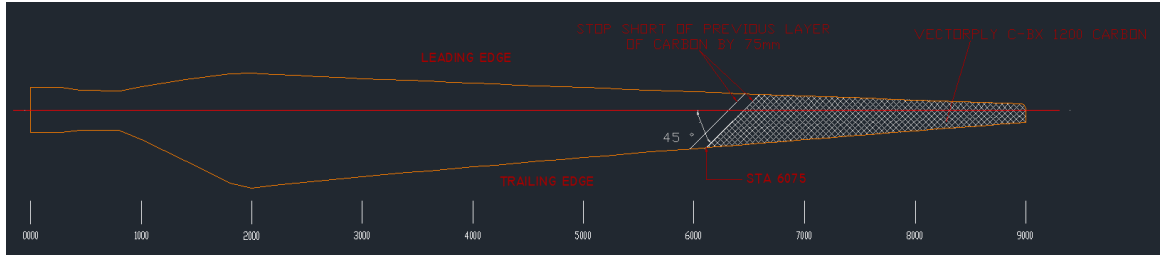
(B.1)



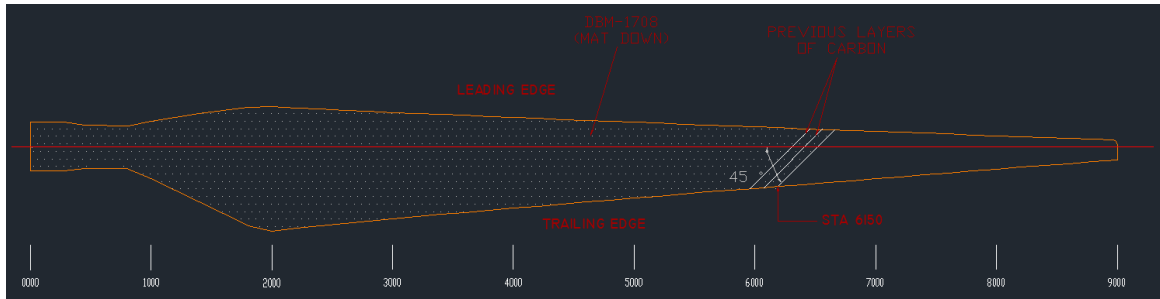
(B.2)



(F.1)



(F.2)



(G)

APPENDIX F: INFLOW AND TURBINE INSTRUMENTATION

Table F.1 Inflow Instrumentation

Name	Instrument	Location	Placement
BAHHATI	Ultrasonic Anemometer	Center Met Tower	Hub Height
BAHHATIV			
BAHHATI			
BAHHATIT			
BAHHC	Cup		
BAHHV	Wind Vane		
BARTC	Cup		Rotor Top
BARBC	Cup		Rotor Bottom
BA2mC	Cup		2m
BATP	Temperature		2m
BADTP	Differential Temperature		
BAHHEC	Cup		Near South Met Tower
BAHHWC	Cup	Near North Met Tower	
OHHC	Cup	Off-Axis Met Tower	
OHHV	Wind Vane		
BAROMETRIC_PRESSURE	Barometric Pressure	Instrument Building	2m

Table F.2 Turbine Instrumentation

Name	Instrument	Location	Placement
On_Off	Turbine Monitor	Tower Base	
GENERATOR_POWER	Turbine Power		
PLC_BRAKE_M	Maintenance Brake Monitor	Tower Base	
PLC_BRAKE_E	Emergency Brake Monitor		
YAW_ANGLE	Yaw Position	Nacelle	
AZIMUTH_ANGLE	Rotor Azimuth		
ROTATIONAL_SPEED	Rotor Speed		
LSS_SPEED	Rotor Speed, Magnetic Encoder		
NACELLE_IMU_AX	Fore-Aft Acceleration		
NACELLE_IMU_AY	Side-to-Side Acceleration		
NACELLE_IMU_AZ	Up-Down Acceleration		
NACELLE_IMU_RX	Pitch Rate		
NACELLE_IMU_RY	Roll Rate		
NACELLE_IMU_RZ	Yaw Rate		
BTNACC	Wind Speed Cup		
TOWER_BENDING_FA	Fore-Aft Bending	Tower	12 Feet
TOWER_BENDING_SS	Side-to-Side Bending		

Table F.3 Rotor Instrumentation

Name	Instrument	Location	Placement		
Bn_Strain_0350_Z_TE	Root Edge Bending	Blade n, where n = 1,2,3	Root		
Bn_Strain_0350_Z_LE					
Bn_Strain_0350_Z_HP	Root Flap Bending		Blade n, where n = 1,2,3	Root	
Bn_Strain_0350_Z_LP					
Bn_Strain_2250_Z_LP	Flap Bending - 1/4 span			2250 mm	
Bn_Strain_4500_Z_LP	Flap Bending - 1/2 span			4500 mm	
Bn_Strain_6750_Z_LP	Flap Bending - 3/4 span			6750 mm	
Hn_Strain_Z_Flap	Hub Flap Bending			Hub	
Hn_Strain_Z_Edge	Hub Edge Bending				
Bn_Accel_2000_X_HP	Tri-axial Accelerometer		Blade n, where n = 1,2,3	2000 mm, Centerline	
Bn_Accel_2000_Y_HP					
Bn_Accel_2000_Z_HP					
Bn_Accel_2000_X_TE	Uni-axial Accelerometer	2000 mm, Offset			
Bn_Accel_8000_X_HP	Tri-axial Accelerometer	Blade n, where n = 1,2,3		8000 mm	
Bn_Accel_8000_Y_HP					
Bn_Accel_8000_Z_HP					
Bn_Accel_8000_X_TE	Uni-axial Accelerometer			8000 mm	
Bn_FBGT_0350_Z_LP	Fiber Optic Temperature			Blade n, where n = 1,2,3	Root
Bn_FBGT_2250_Z_LP	Fiber Optic Temperature				2250 mm
Bn_FBGT_4500_Z_LP	Fiber Optic Temperature	4500 mm			
Bn_FBGT_6750_Z_LP	Fiber Optic Temperature	6750 mm			
Bn_FBGS_6750_Z_LP	Fiber Optic Strain, flap	6750 mm			
Bn_FBGS_4500_Z_LP	Fiber Optic Strain, flap	4500 mm			
Bn_FBGS_2250_Z_LP	Fiber Optic Strain, flap	2250 mm			
Bn_FBGS_0350_Z_LP	Fiber Optic Strain, flap	Hub			
Bn_FBGS_0350_Z_LE	Fiber Optic Strain, edge				
Bn_FBGT_0350_Z_HP	Fiber Optic Temperature				
Bn_FBGS_0350_Z_HP	Fiber Optic Strain, flap				
Bn_FBGS_0350_Z_TE	Fiber Optic Strain, edge				
Bn_Motor1_Position	Flap 1, motor position		Blade n, where n = 1,2,3		7330 mm
Bn_Motor1_Current	Flap 1, motor current				
Bn_Motor2_Position	Flap 2, motor position	Control Enclosure		7940 mm	
Bn_Motor2_Current	Flap 2, motor current				
Bn_Motor3_Position	Flap 3, motor position			8550 mm	
Bn_Motor3_Current	Flap 3, motor current				
Athena_AnalogOut1	Blade 1 command	Control Enclosure	Hub		
Athena_AnalogOut2	Blade 2 command				
Athena_AnalogOut3	Blade 3 command				
DAQ_IMU_X	Rotor Acceleration	DAQ Enclosure	Hub Center		
DAQ_IMU_Y					
DAQ_IMU_Z					

APPENDIX G: DATA FILE SUMMARIES

Table G.1 Initial shakedown.

Data File	Time Stamp Label	Mean Wind Speed (m/s)	Median Wind Direction (deg)	Event Time	Turbine State	AAD State Change
2012-02-01-20-55-49.zip	'Wed, Feb 01, 2012 2:55:49 PM'	6.4	331	14:57:30	parked	homing
				15:05:20	slow roll, start	
2012-02-01-21-05-52.zip	'Wed, Feb 01, 2012 3:05:53 PM'	6.0	343	15:06:45	slow roll, stop	
				15:08:15	parked	sine(5deg,1Hz)
				15:09:15	parked	stopped
2012-02-01-21-19-45.zip	'Wed, Feb 01, 2012 3:19:46 PM'	5.4	24	15:20:45	parked	homing
				15:22:20	parked	homing
				15:23:40	parked	homing
				15:26:09	parked	sine(10deg,1Hz)
				15:27:07	parked	stopped
2012-02-01-22-42-36.zip	'Wed, Feb 01, 2012 4:42:36 PM'	5.5	15	16:42:55	slow roll, start	
				16:44:30	slow roll, stop	
2012-02-01-22-50-31.zip	'Wed, Feb 01, 2012 4:50:32 PM'	3.5	22	16:53:30	slow roll, start	
				16:56:00	slow roll, stop	
				16:59:10	parked	homing
2012-02-01-23-00-34.zip	'Wed, Feb 01, 2012 5:00:35 PM'	3.9	21	17:00:00	slow roll, start	
				17:00:55	turning	sine(10deg,1Hz)
				17:02:45	slow roll, stop	
2012-02-01-23-10-34.zip	'Wed, Feb 01, 2012 5:10:35 PM'	4.3	13	17:03:05	parked	stopped
					parked	
2012-02-10-17-13-42.zip	'Fri, Feb 10, 2012 11:13:42 AM'	2.5	331	11:14:00	parked	sine(10deg,1Hz)
				11:16:00	parked	stopped
				11:17:00	parked	B1: sine sweep(10deg)
2012-02-10-17-23-47.zip	'Fri, Feb 10, 2012 11:23:48 AM'	1.8	55	11:26:00	parked	stopped
				11:28:00	parked	sine sweep(10deg)
2012-02-10-17-33-45.zip	'Fri, Feb 10, 2012 11:33:46 AM'	1.9	317	11:38:00	parked	stopped
2012-02-10-17-43-45.zip	'Fri, Feb 10, 2012 11:43:45 AM'	1.6	251	11:43:45	parked	sine series(10deg)
2012-02-10-17-53-50.zip	'Fri, Feb 10, 2012 11:53:50 AM'	1.6	38	11:54:00	parked	stopped
2012-02-10-18-59-59.zip	'Fri, Feb 10, 2012 12:59:59 PM'	2.3	298	13:02:00	parked	steps(5deg,20s)
				13:03:30	slow roll, start	
				13:06:45	slow roll, stop	
2012-02-10-19-10-02.zip	'Fri, Feb 10, 2012 1:10:03 PM'	1.9	308	13:07:00	parked	stopped
					parked	

Table G.2 First operation during power production.

Data File	Time Stamp Label	Mean Wind Speed (m/s)	Median Wind Direction (deg)	Event Time	Turbine State	AAD State Change
2012-02-21-14-49-46.zip	'Tue, Feb 21, 2012 8:49:47 AM'	7.8	248	8:51:00	parked	sine(10deg,1Hz)
				8:59:45	parked	stopped
2012-02-21-14-59-50.zip	'Tue, Feb 21, 2012 8:59:51 AM'	7.7	255	9:00:30	starting	
				9:02:20	generating	
2012-02-21-15-09-50.zip	'Tue, Feb 21, 2012 9:09:51 AM'	9.2	258	9:11:00	generating	steps(5deg,20s)
2012-02-21-15-19-51.zip	'Tue, Feb 21, 2012 9:19:52 AM'	10.2	264	9:20:20	generating	stopped
				9:21:30	generating	steps(5deg,40s)
				9:29:50	generating	stopped
2012-02-21-15-29-51.zip	'Tue, Feb 21, 2012 9:29:52 AM'	11	264	9:31:30	generating	steps(10deg,30s)
2012-02-21-15-39-51.zip	'Tue, Feb 21, 2012 9:39:51 AM'	11.6	262	9:41:20	generating	stopped
				9:43:10	stopping	
2012-02-21-15-49-50.zip	'Tue, Feb 21, 2012 9:49:50 AM'	10.5	271		parked	
2012-02-29-18-31-09.zip	'Wed, Feb 29, 2012 12:31:10 PM'	3.9	224	12:31:00	parked	homing
				12:33:00	parked	sine(5deg,1Hz)
				12:35:40	parked	stopped
2012-02-29-18-41-09.zip	'Wed, Feb 29, 2012 12:41:09 PM'	2.4	219		parked	
2012-02-29-18-48-56.zip	'Wed, Feb 29, 2012 12:48:56 PM'	4.5	187	12:50:30	parked	homing
				12:52:10	parked	sine(5deg,1Hz)
				12:56:50	parked	stopped
2012-02-29-18-58-59.zip	'Wed, Feb 29, 2012 12:58:59 PM'	4.5	197		parked	
2012-02-29-19-08-59.zip	'Wed, Feb 29, 2012 1:08:59 PM'	4.5	201	13:14:20	parked	static 0deg flap
				13:17:30	parked	stopped
2012-02-29-19-18-59.zip	'Wed, Feb 29, 2012 1:18:59 PM'	5.9	203	13:24:30	parked	homing
2012-02-29-19-28-59.zip	'Wed, Feb 29, 2012 1:28:59 PM'	4.7	190		parked	
2012-02-29-19-44-50.zip	'Wed, Feb 29, 2012 1:44:50 PM'	5.2	185		parked	
2012-02-29-19-54-53.zip	'Wed, Feb 29, 2012 1:54:53 PM'	5.1	186	14:01:25	parked	homing
2012-02-29-20-04-53.zip	'Wed, Feb 29, 2012 2:04:53 PM'	5.6	189	14:11:30	parked	
2012-02-29-20-14-53.zip	'Wed, Feb 29, 2012 2:14:53 PM'	6	195	14:18:25	parked	homing
2012-02-29-20-24-53.zip	'Wed, Feb 29, 2012 2:24:53 PM'	5.1	193		parked	
2012-02-29-20-34-52.zip	'Wed, Feb 29, 2012 2:34:53 PM'	6.1	213	14:36:15	parked	homing
				14:40:05	parked	homing
				14:40:30	parked	homing
				14:44:45	parked	homing
2012-02-29-20-44-52.zip	'Wed, Feb 29, 2012 2:44:53 PM'	7.6	208	14:50:25	parked	sine(5deg,1Hz)
				14:52:05	parked	stopped
				14:52:30	parked	homing
				14:53:15	parked	sine(5deg,1Hz)
2012-02-29-20-54-53.zip	'Wed, Feb 29, 2012 2:54:53 PM'	7.9	212	14:59:20	parked	stopped

Table G.3 Static flap settings with 10-minute data files.

Data File	Time Stamp Label	Mean Wind Speed (m/s)	Median Wind Direction (deg)	Event Time	Turbine State	AAD State Change	
2012-03-09-15-19-51.zip	'Fri, Mar 09, 2012 9:19:52 AM'	CORRECTING STRAIN OFFSETS - SIGNALS ARE IN RAW COUNTS					
2012-03-14-16-37-33.zip	'Wed, Mar 14, 2012 11:37:33 AM'	8.2	220	11:37:45	starting		
				11:38:45	generating		
				11:40:20	generating	steps(15deg,20s)	
2012-03-14-16-47-37.zip	'Wed, Mar 14, 2012 11:47:38 AM'	7.6	216	11:48:20	generating	stopped	
				11:48:40	generating	steps(20deg,20s)	
2012-03-14-16-57-37.zip	'Wed, Mar 14, 2012 11:57:38 AM'	7.7	221	11:58:15	generating	stopped	
				11:59:05	stopping		
2012-03-14-17-07-36.zip	'Wed, Mar 14, 2012 12:07:37 PM'	7.5	216		parked		
2012-03-14-17-17-36.zip	'Wed, Mar 14, 2012 12:17:36 PM'	7.6	222	12:20:40	parked	static 0deg flap	
2012-03-14-17-27-36.zip	'Wed, Mar 14, 2012 12:27:37 PM'	7.8	224		parked		
2012-03-14-17-37-36.zip	'Wed, Mar 14, 2012 12:37:37 PM'	8.6	221		parked		
2012-03-14-17-47-36.zip	'Wed, Mar 14, 2012 12:47:37 PM'	8.6	221	12:56:25	parked	stopped	
				12:56:40	parked	sine(10deg,1Hz)	
				12:57:20	parked	stopped	
				12:57:30	parked	static 0deg flap	
2012-03-14-17-57-40.zip	'Wed, Mar 14, 2012 12:57:41 PM'	7.8	222	12:58:10	starting		
				12:59:00	generating		
				12:59:10	generating	stopped	
				13:00:30	generating	step series(2P)	
2012-03-14-18-07-37.zip	'Wed, Mar 14, 2012 1:07:38 PM'	8	219		generating		
2012-03-14-18-17-37.zip	'Wed, Mar 14, 2012 1:17:38 PM'	7.8	215		generating		
2012-03-14-18-27-37.zip	'Wed, Mar 14, 2012 1:27:38 PM'	7.3	214		generating		
2012-03-14-18-37-37.zip	'Wed, Mar 14, 2012 1:37:38 PM'	7.2	211		generating		
2012-03-14-18-47-37.zip	'Wed, Mar 14, 2012 1:47:38 PM'	7.2	212		generating		
2012-03-14-18-57-37.zip	'Wed, Mar 14, 2012 1:57:38 PM'	7.3	201	14:00:25	generating	stopped	
				14:01:45	generating	static 0deg flap	
2012-03-14-19-07-38.zip	'Wed, Mar 14, 2012 2:07:38 PM'	7.4	197		generating		
2012-03-14-19-17-38.zip	'Wed, Mar 14, 2012 2:17:38 PM'	8.2	198		generating		
				14:27:20	generating	stopped	
2012-03-14-19-27-37.zip	'Wed, Mar 14, 2012 2:27:38 PM'	8.2	191	14:27:45	generating	static -10deg flap	
				14:37:45	generating	stopped	
2012-03-14-19-37-37.zip	'Wed, Mar 14, 2012 2:37:38 PM'	7.2	195	14:37:55	generating	static -20deg flap	
				14:45:20	generating	stopped	
				14:46:55	generating	static 10deg flap	
2012-03-14-19-47-37.zip	'Wed, Mar 14, 2012 2:47:38 PM'	8.4	189	14:57:15	generating	stopped	
2012-03-14-19-57-37.zip	'Wed, Mar 14, 2012 2:57:38 PM'	8.1	200	14:57:40	generating	static 20deg flap	
2012-03-14-20-07-37.zip	'Wed, Mar 14, 2012 3:07:38 PM'	8.3	197	15:07:50	generating	stopped	
				15:08:25	generating	static 15deg flap	
				15:17:15	generating	stopped	
2012-03-14-20-17-38.zip	'Wed, Mar 14, 2012 3:17:38 PM'	8.1	209	15:17:40	generating	static -15deg flap	
				15:27:30	generating	stopped	
2012-03-14-20-27-38.zip	'Wed, Mar 14, 2012 3:27:38 PM'	7.6	205	15:27:40	generating	static -5deg flap	
2012-03-14-20-37-37.zip	'Wed, Mar 14, 2012 3:37:38 PM'	7.5	199	15:38:10	generating	stopped	
				15:38:20	generating	static 5deg flap	
				15:47:35	generating	stopped	
2012-03-14-20-47-37.zip	'Wed, Mar 14, 2012 3:47:38 PM'	7.5	225	15:45:45	generating	static 0deg flap	
				15:54:45	generating	stopped	
				15:56:50	generating	sine steps 5deg	
2012-03-14-20-57-37.zip	'Wed, Mar 14, 2012 3:57:38 PM'	7.5	222	16:06:50	generating	stopped	
				16:07:25	stopping		
2012-03-14-21-07-38.zip	'Wed, Mar 14, 2012 4:07:38 PM'	7.1	202	16:07:45	parked	sine(10deg,1Hz)	
				16:16:45	parked	stopped	
2012-03-14-21-17-37.zip	'Wed, Mar 14, 2012 4:17:37 PM'	8.9	219		parked	off	

Table G.4 Sine sweeps during power production.

Data File	Time Stamp Label	Mean Wind Speed (m/s)	Median Wind Direction (deg)	Event Time	Turbine State	AAD State Change
2012-04-09-15-23-23.zip	Mon, Apr 09, 2012 10:23:23 AM	9.6	213	10:24:06	parked	sine(10deg, 1Hz)
2012-04-09-15-24-29.zip	Mon, Apr 09, 2012 10:24:30 AM	9.2	213	10:25:15	parked	stopped
2012-04-09-15-25-24.zip	Mon, Apr 09, 2012 10:25:24 AM	9.4	212	10:25:43	startup attempt	
				10:26:06	starting	
2012-04-09-15-26-23.zip	Mon, Apr 09, 2012 10:26:23 AM	9.4	214	10:26:57	generating	off
2012-04-09-15-27-23.zip	Mon, Apr 09, 2012 10:27:23 AM	8.1	209		generating	off
2012-04-09-15-28-23.zip	Mon, Apr 09, 2012 10:28:24 AM	7.3	214		generating	off
2012-04-09-15-29-26.zip	Mon, Apr 09, 2012 10:29:26 AM	6.8	212		generating	off
2012-04-09-15-30-23.zip	Mon, Apr 09, 2012 10:30:24 AM	8.2	218	10:31:00	generating	sine sweep(10deg, 250s)
2012-04-09-15-31-23.zip	Mon, Apr 09, 2012 10:31:24 AM	7.3	216		generating	
2012-04-09-15-32-23.zip	Mon, Apr 09, 2012 10:32:24 AM	7.1	212		generating	
2012-04-09-15-33-23.zip	Mon, Apr 09, 2012 10:33:24 AM	9.5	211		generating	
2012-04-09-15-34-23.zip	Mon, Apr 09, 2012 10:34:24 AM	7.8	211	10:35:15	generating	stopped
2012-04-09-15-35-23.zip	Mon, Apr 09, 2012 10:35:24 AM	8.9	215		generating	
2012-04-09-15-36-23.zip	Mon, Apr 09, 2012 10:36:24 AM	9.1	212		generating	
2012-04-09-15-37-23.zip	Mon, Apr 09, 2012 10:37:24 AM	8.9	213		generating	
2012-04-09-15-38-23.zip	Mon, Apr 09, 2012 10:38:24 AM	8.6	214		generating	
2012-04-09-15-39-23.zip	Mon, Apr 09, 2012 10:39:24 AM	7.8	203		generating	
2012-04-09-15-39-55.zip	Mon, Apr 09, 2012 10:39:56 AM	8.3	213	10:40:06	generating	sine sweep(15deg, 250s)
				10:44:30	generating	stopped
2012-04-09-15-50-01.zip	Mon, Apr 09, 2012 10:50:01 AM	8.8	211	10:51:28	generating	sine sweep(15deg, 500s)
				11:00:00	generating	stopped
2012-04-09-16-00-01.zip	Mon, Apr 09, 2012 11:00:02 AM	9.4	211		generating	
2012-04-09-16-10-01.zip	Mon, Apr 09, 2012 11:10:01 AM	8.9	213	11:10:12	generating	attempt step series(2P)
				11:11:20	generating	stopped
				11:14:06	generating	attempt static 0deg
				11:16:15	generating	stopped
				11:16:48	generating	attempt sine(10deg, 1Hz)
				11:17:47	generating	stopped
				11:19:06	generating	attempt static 0deg
2012-04-09-16-20-01.zip	Mon, Apr 09, 2012 11:20:01 AM	8.5	214	11:21:44	stopping	
				11:22:26	parked	stopped
				11:24:25	parked	attempt sine(10deg, 1Hz)
2012-04-09-16-30-00.zip	Mon, Apr 09, 2012 11:30:00 AM	8.8	214		parked	off

Table G.5 Power production at prevailing wind direction with flap step series.

Data File	Time Stamp Label	Mean Wind Speed (m/s)	Median Wind Direction (deg)	Event Time	Turbine State	AAD State Change
2012-04-24-14-45-49.zip	Tue, Apr 24, 2012 9:45:50 AM	9.1	234	9:48:00	parked	sine(10deg, 1Hz)
				9:48:45	parked	stopped
				9:50:10	startup attempt	
				9:51:19	starting	
				9:51:54	generating	
				9:52:49	generating	step series(10s)
				9:54:22	generating	stopped
2012-04-24-14-55-54.zip	Tue, Apr 24, 2012 9:55:55 AM	8.7	234	10:02:14	generating	step series(30s)
2012-04-24-15-05-55.zip	Tue, Apr 24, 2012 10:05:55 AM	9.1	236		generating	
2012-04-24-15-15-55.zip	Tue, Apr 24, 2012 10:15:56 AM	8.7	237		generating	
2012-04-24-15-25-55.zip	Tue, Apr 24, 2012 10:25:56 AM	7.6	227		generating	
2012-04-24-15-35-55.zip	Tue, Apr 24, 2012 10:35:56 AM	7.5	227		generating	
2012-04-24-15-45-55.zip	Tue, Apr 24, 2012 10:45:56 AM	7.7	221		generating	
2012-04-24-15-55-55.zip	Tue, Apr 24, 2012 10:55:56 AM	7.8	224		generating	
2012-04-24-16-05-55.zip	Tue, Apr 24, 2012 11:05:56 AM	7.7	216		generating	
2012-04-24-16-15-55.zip	Tue, Apr 24, 2012 11:15:55 AM	7.2	209		generating	
2012-04-24-16-25-55.zip	Tue, Apr 24, 2012 11:25:56 AM	7.8	206		generating	
2012-04-24-16-35-55.zip	Tue, Apr 24, 2012 11:35:55 AM	7.2	209		generating	
2012-04-24-16-45-55.zip	Tue, Apr 24, 2012 11:45:55 AM	7.1	208		generating	
2012-04-24-16-55-55.zip	Tue, Apr 24, 2012 11:55:55 AM	7.5	205		generating	
2012-04-24-17-05-55.zip	Tue, Apr 24, 2012 12:05:55 PM	8.5	205		generating	
2012-04-24-17-15-55.zip	Tue, Apr 24, 2012 12:15:55 PM	8.5	205		generating	
2012-04-24-17-25-55.zip	Tue, Apr 24, 2012 12:25:55 PM	9	194		generating	
2012-04-24-17-35-55.zip	Tue, Apr 24, 2012 12:35:55 PM	8.9	200		generating	
2012-04-24-17-45-55.zip	Tue, Apr 24, 2012 12:45:55 PM	9.9	203		generating	
2012-04-24-17-55-55.zip	Tue, Apr 24, 2012 12:55:56 PM	9.3	207		generating	
2012-04-24-18-05-55.zip	Tue, Apr 24, 2012 1:05:55 PM	9.9	200		generating	
2012-04-24-18-15-55.zip	Tue, Apr 24, 2012 1:15:55 PM	9.9	200		generating	
2012-04-24-18-25-55.zip	Tue, Apr 24, 2012 1:25:55 PM	10	203		generating	
2012-04-24-18-35-55.zip	Tue, Apr 24, 2012 1:35:56 PM	9.8	212		generating	
2012-04-24-18-45-55.zip	Tue, Apr 24, 2012 1:45:56 PM	9.9	204		generating	
2012-04-24-18-55-55.zip	Tue, Apr 24, 2012 1:55:56 PM	9.5	208		generating	
				13:59:58	generating	stopped
2012-04-24-19-05-55.zip	Tue, Apr 24, 2012 2:05:55 PM	9	226		generating	
2012-04-24-19-15-55.zip	Tue, Apr 24, 2012 2:15:55 PM	9.5	226		generating	
2012-04-24-19-25-55.zip	Tue, Apr 24, 2012 2:25:55 PM	9.1	211		generating	
2012-04-24-19-35-55.zip	Tue, Apr 24, 2012 2:35:56 PM	8.9	216		generating	
2012-04-24-19-45-55.zip	Tue, Apr 24, 2012 2:45:55 PM	8.6	207		generating	
2012-04-24-19-55-55.zip	Tue, Apr 24, 2012 2:55:55 PM	8.6	217		generating	
2012-04-24-20-05-55.zip	Tue, Apr 24, 2012 3:05:56 PM	9.1	219		generating	
2012-04-24-20-15-55.zip	Tue, Apr 24, 2012 3:15:55 PM	8.1	219		generating	
2012-04-24-20-25-55.zip	Tue, Apr 24, 2012 3:25:55 PM	8.3	230		generating	
2012-04-24-20-35-55.zip	Tue, Apr 24, 2012 3:35:56 PM	6.8	231		generating	
2012-04-24-20-45-55.zip	Tue, Apr 24, 2012 3:45:55 PM	6.5	242		generating	

Table G.6 Power production with flap step series.

Data File	Time Stamp Label	Mean Wind Speed (m/s)	Median Wind Direction (deg)	Event Time	Turbine State	AAD State Change
2012-04-30-19-32-50.zip	Mon, Apr 30, 2012 2:32:51 PM	6.1	173	14:34:02	parked	sine(5deg,1Hz)
				14:36:15	parked	stopped
				14:36:55	parked	sine(20deg,1Hz)
				14:38:08	parked	stopped
2012-04-30-19-42-54.zip	Mon, Apr 30, 2012 2:42:55 PM	7.1	164	14:45:54	parked	step series(30s)
2012-04-30-19-55-18.zip	Mon, Apr 30, 2012 2:55:18 PM	6.7	194		parked	
2012-04-30-20-05-18.zip	Mon, Apr 30, 2012 3:05:18 PM	5.9	183	15:11:06	parked	stopped
2012-04-30-20-15-18.zip	Mon, Apr 30, 2012 3:15:18 PM	7.6	180		parked	
2012-04-30-20-25-17.zip	Mon, Apr 30, 2012 3:25:18 PM	7.1	184		parked	
2012-04-30-20-35-17.zip	Mon, Apr 30, 2012 3:35:18 PM	6	165	15:36:15	starting	static 0deg
				15:37:37	generating	stopped
				15:39:53	generating	step series(30s)
				15:44:36	dip in rotor speed	
2012-04-30-20-47-20.zip	Mon, Apr 30, 2012 3:47:21 PM	6.7	176		generating	
2012-04-30-20-57-25.zip	Mon, Apr 30, 2012 3:57:26 PM	7.8	172		generating	
2012-04-30-21-07-27.zip	Mon, Apr 30, 2012 4:07:27 PM	6.1	182		generating	stopped
				16:15:20	stopping	
2012-05-10-19-21-14.zip	Thu, May 10, 2012 2:21:14 PM	7.5	140	14:23:45	starting	static 0deg
				14:24:38	generating	stopped
				14:25:35	generating	step series(30s)
2012-05-10-19-31-19.zip	Thu, May 10, 2012 2:31:20 PM	7.8	143		generating	
2012-05-10-19-41-20.zip	Thu, May 10, 2012 2:41:20 PM	6.7	159		generating	
2012-05-10-19-51-20.zip	Thu, May 10, 2012 2:51:21 PM	7.4	153		generating	
2012-05-10-20-01-20.zip	Thu, May 10, 2012 3:01:20 PM	6.7	140		generating	
2012-05-10-20-11-20.zip	Thu, May 10, 2012 3:11:20 PM	5.9	155		generating	
2012-05-10-20-21-20.zip	Thu, May 10, 2012 3:21:20 PM	7.4	142		generating	
				15:30:58	dip in rotor speed	
2012-05-10-20-31-20.zip	Thu, May 10, 2012 3:31:20 PM	7.7	149		generating	
2012-05-10-20-41-20.zip	Thu, May 10, 2012 3:41:20 PM	7.3	145	15:42:38	generating	stopped
				15:42:49	stopping	static 0deg
2012-05-10-20-51-25.zip	Thu, May 10, 2012 3:51:26 PM	7.2	146			
2012-05-23-18-10-35.zip	Wed, May 23, 2012 1:10:36 PM	9.7	238		parked	
2012-05-23-18-38-19.zip	Wed, May 23, 2012 1:38:19 PM	10.1	249	13:41:13	parked	sine(20deg,1Hz)
				13:42:15	parked	stopped
				13:43:15	starting	static 0deg
				13:43:49	generating	stopped
				13:45:13	generating	step series(30s)
2012-05-23-18-48-24.zip	Wed, May 23, 2012 1:48:25 PM	10	248		generating	
2012-05-23-18-58-25.zip	Wed, May 23, 2012 1:58:25 PM	9.5	248		generating	
2012-05-23-19-08-24.zip	Wed, May 23, 2012 2:08:25 PM	9.7	259		generating	
2012-05-23-19-18-24.zip	Wed, May 23, 2012 2:18:25 PM	9.7	239		generating	
2012-05-23-19-28-24.zip	Wed, May 23, 2012 2:28:25 PM	10.9	239		generating	
2012-05-23-19-38-24.zip	Wed, May 23, 2012 2:38:25 PM	10.1	231		generating	
2012-05-23-19-48-24.zip	Wed, May 23, 2012 2:48:25 PM	10.2	240		generating	
2012-05-23-19-58-24.zip	Wed, May 23, 2012 2:58:25 PM	11.1	247		generating	
2012-05-23-20-08-24.zip	Wed, May 23, 2012 3:08:25 PM	10.7	234		generating	
2012-05-23-20-18-24.zip	Wed, May 23, 2012 3:18:24 PM	9.9	245		generating	
2012-05-23-20-28-24.zip	Wed, May 23, 2012 3:28:25 PM	9.7	239		generating	
2012-05-23-20-38-24.zip	Wed, May 23, 2012 3:38:25 PM	10.1	224		generating	
2012-05-23-20-48-24.zip	Wed, May 23, 2012 3:48:25 PM	11	242		generating	
2012-05-23-20-58-24.zip	Wed, May 23, 2012 3:58:24 PM	11.4	237		generating	
2012-05-23-21-08-24.zip	Wed, May 23, 2012 4:08:25 PM	10.9	241		generating	stopped
				16:15:59	stopping	static 0deg
2012-05-23-21-18-24.zip	Wed, May 23, 2012 4:18:24 PM	10.7	241		parked	stopped

Table G.7 Data files during video of flaps in operation.

Data File	Time Stamp Label	Mean Wind Speed (m/s)	Median Wind Direction (deg)	Event Time	Turbine State	AAD State Change
2012-05-04-15-14-36.zip	Fri, May 04, 2012 10:14:37 AM	5.1	235	10:17:21	parked	homing
				10:18:25	parked	homing
				10:20:09	parked	homing
				10:20:42	parked	homing
				10:22:16	parked	step series(2P)
				10:23:39	parked	stopped
				10:24:02	parked	sine series(10deg)
2012-05-04-15-25-09.zip	Fri, May 04, 2012 10:25:09 AM	4.7	234	10:25:09	parked	stopped
				10:25:40	parked	sine sweep(10deg,10s)
				10:27:38	starting	
				10:30:40	generating	
				10:32:01	generating	step series(2P)
				10:34:34	generating	stopped
				10:35:04	generating	sine series(10deg)
2012-05-04-15-35-10.zip	Fri, May 04, 2012 10:35:11 AM	4.3	223	10:35:41	generating	stopped
				10:36:24	generating	sine sweep(10deg,10s)
				10:37:14	generating	sine sweep(10deg,10s)
				10:37:50	generating	sine sweep(10deg,10s)
				10:39:09	stopping	
2012-05-04-15-45-10.zip	Fri, May 04, 2012 10:45:10 AM	4.8	219		off	

Table G.8 Power production with tape sealing possible air gaps in flap modules.

Data File	Time Stamp Label	Mean Wind Speed (m/s)	Median Wind Direction (deg)	Event Time	Turbine State	AAD State Change
2012-05-25-15-19-24.zip	Fri, May 25, 2012 10:19:24 AM	7.3	250	10:20:55	starting	taped
				10:22:03	generating	taped
2012-05-25-15-29-29.zip	Fri, May 25, 2012 10:29:30 AM	8	247		generating	taped
2012-05-25-15-39-29.zip	Fri, May 25, 2012 10:39:30 AM	7.8	241		generating	taped
2012-05-25-15-49-29.zip	Fri, May 25, 2012 10:49:30 AM	8.4	248		generating	taped
2012-05-25-15-59-29.zip	Fri, May 25, 2012 10:59:30 AM	6.9	253		generating	taped
2012-05-25-16-09-28.zip	Fri, May 25, 2012 11:09:29 AM	6.1	250	11:03:27	stopping	taped
					parked	taped

DISTRIBUTION

- 1 Shreyas Ananthan c/o Ivette Gonzalez
Office of Wind and Water Power Technologies
EE-2B Forrestal Building, U.S. DOE
1000 Independence Ave. SW
Washington, DC 20585

- 1 Dale Berg
12421 Chelwood Trl NE
Albuquerque, NM 87112

- 1 Michael Derby c/o Ivette Gonzalez
Office of Wind and Water Power Technologies
EE-2B Forrestal Building, U.S. DOE
1000 Independence Ave. SW
Washington, DC 20585

- 1 Mark Higgins c/o Ivette Gonzalez
Office of Wind and Water Power Technologies
EE-2B Forrestal Building, U.S. DOE
1000 Independence Ave. SW
Washington, DC 20585

- 1 Jose Zayas c/o Ivette Gonzalez
Office of Wind and Water Power Technologies
EE-2B Forrestal Building, U.S. DOE
1000 Independence Ave. SW
Washington, DC 20585

- 1 MS0899 Technical Library 9536 (electronic copy)



Sandia National Laboratories